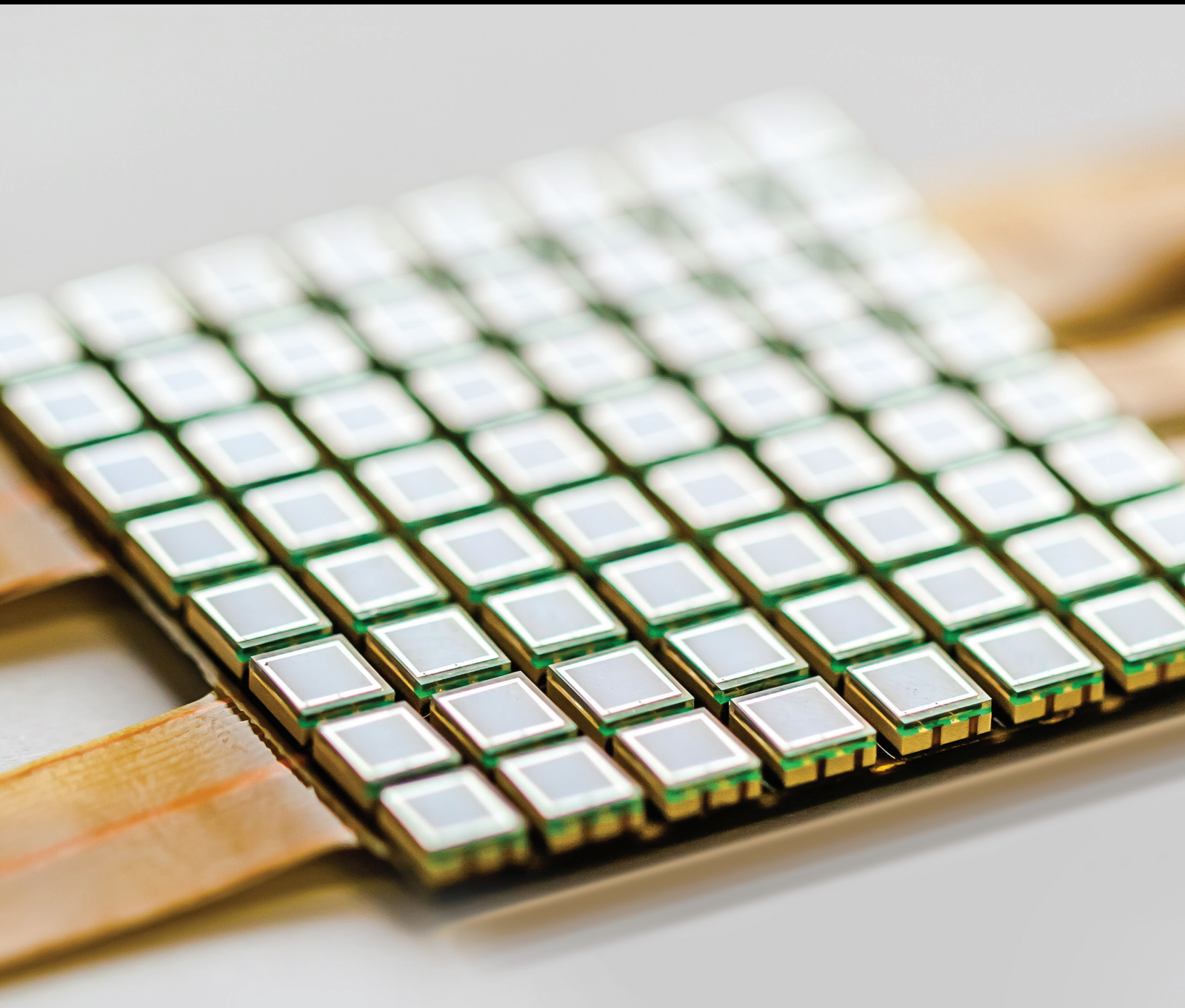


# Remote Sensing of Sustainable Ecosystems

Lead Guest Editor: Yichun Xie

Guest Editors: Zongyao Sha and Victor Mesev





---

# **Remote Sensing of Sustainable Ecosystems**

Journal of Sensors

---

## **Remote Sensing of Sustainable Ecosystems**

Lead Guest Editor: Yichun Xie

Guest Editors: Zongyao Sha and Victor Mesev



---

Copyright © 2018 Hindawi. All rights reserved.

This is a special issue published in "Journal of Sensors." All articles are open access articles distributed under the Creative Commons Attribution License, which permits unrestricted use, distribution, and reproduction in any medium, provided the original work is properly cited.

## Editorial Board

- Harith Ahmad, Malaysia  
M. İlhan Akbaş, USA  
Manuel Aleixandre, Spain  
Bruno Andò, Italy  
Constantin Apetrei, Romania  
Marko Beko, Portugal  
Fernando Benito-Lopez, Spain  
Romeo Bernini, Italy  
Shekhar Bhansali, USA  
Wojtek J. Bock, Canada  
Matthew Brodie, Australia  
Paolo Bruschi, Italy  
Belén Calvo, Spain  
Stefania Campopiano, Italy  
Domenico Caputo, Italy  
Sara Casciati, Italy  
Gabriele Cazzulani, Italy  
Chi Chiu Chan, Singapore  
Edmon Chehura, UK  
Marvin H Cheng, USA  
Nicola Cioffi, Italy  
Mario Collotta, Italy  
Marco Consales, Italy  
Jesus Corres, Spain  
Andrea Cusano, Italy  
Antonello Cutolo, Italy  
Dzung Dao, Australia  
Egidio De Benedetto, Italy  
Luca De Stefano, Italy  
Manel del Valle, Spain  
Francesco Dell'Olio, Italy  
Franz L. Dickert, Austria  
Giovanni Diraco, Italy  
Nicola Donato, Italy  
Mauro Epifani, Italy  
Abdelhamid Errachid, France  
Stephane Evoy, Canada  
Vittorio Ferrari, Italy  
Luca Francioso, Italy  
Manel Gasulla, Spain  
Carmine Granata, Italy  
Banshi D. Gupta, India  
Mohammad Haider, USA  
Clemens Heitzinger, Austria
- M. del Carmen Horrillo, Spain  
Evangelos Hristoforou, Greece  
Syed K. Islam, USA  
Stephen James, UK  
Bruno C. Janegitz, Brazil  
Hai-Feng Ji, USA  
Sang Sub Kim, Republic of Korea  
Antonio Lazaro, Spain  
Laura M. Lechuga, Spain  
Chengkuo Lee, Singapore  
Chenzong Li, USA  
Xinyu Liu, Canada  
Eduard Llobet, Spain  
Jaime Lloret, Spain  
Yu-Lung Lo, Taiwan  
Jesús Lozano, Spain  
Oleg Lupan, Moldova  
Frederick Mailly, France  
Pawel Malinowski, Poland  
Santiago Marco, Spain  
Vincenzo Marletta, Italy  
Carlos Marques, Portugal  
Eugenio Martinelli, Italy  
Antonio Martínez Olmos, Spain  
Jose R. Martinez-De-Dios, Spain  
Giuseppe Maruccio, Italy  
Yasuko Y. Maruo, Japan  
Mike McShane, USA  
Fanli Meng, China  
Carlos Michel, Mexico  
Stephen. J. Mihailov, Canada  
Heinz C. Neitzert, Italy  
Calogero M. Oddo, Italy  
Keat Ghee Ong, USA  
M. Palaniswami, Australia  
Alberto J. Palma, Spain  
Lucio Pancheri, Italy  
Roberto Paolesse, Italy  
Giovanni Pau, Italy  
Alain Pauly, France  
Giorgio Pennazza, Italy  
Michele Penza, Italy  
Salvatore Pirozzi, Italy  
Antonina Pirrotta, Italy
- Stavros Pissadakis, Greece  
Stelios M. Potirakis, Greece  
Biswajeet Pradhan, Malaysia  
Valerie Renaudin, France  
Armando Ricciardi, Italy  
Christos Riziotis, Greece  
Maria Luz Rodriguez-Mendez, Spain  
Jerome Rossignol, France  
Carlos Ruiz, Spain  
Ylias Sabri, Australia  
Josep Samitier, Spain  
José P. Santos, Spain  
Isabel Sayago, Spain  
Giorgio Sberveglieri, Italy  
Andreas Schütze, Germany  
Praveen K. Sekhar, USA  
Sandra Sendra, Spain  
Woosuck Shin, Japan  
Pietro Siciliano, Italy  
Vincenzo Spagnolo, Italy  
Sachin K. Srivastava, India  
Grigore Stamatescu, Romania  
Stefano Stassi, Italy  
Vincenzo Stornelli, Italy  
Weilian Su, USA  
Tong Sun, UK  
Salvatore Surdo, Italy  
Raymond Swartz, USA  
Hidekuni Takao, Japan  
Guiyun Tian, UK  
Suna Timur, Turkey  
Vijay Tomer, USA  
Abdellah Touhafi, Belgium  
Aitor Urrutia, Spain  
H. Vaisocherova - Lisalova, Czech Republic  
Everardo Vargas-Rodriguez, Mexico  
Xavier Vilanova, Spain  
Luca Vollero, Italy  
Tomasz Wandowski, Poland  
Qihao Weng, USA  
Qiang Wu, UK  
Hai Xiao, USA  
Chouki Zerrouki, France

# Contents

---

## **Remote Sensing of Sustainable Ecosystems**

Yichun Xie , Zongyao Sha , and Victor Mesev 

Editorial (2 pages), Article ID 9683415, Volume 2018 (2018)

## **Machine Learning for Estimating Leaf Dust Retention Based on Hyperspectral Measurements**

Wenlong Jing , Xia Zhou, Chen Zhang, Chongyang Wang, and Hao Jiang

Research Article (12 pages), Article ID 6026259, Volume 2018 (2018)

## **Spark Sensing: A Cloud Computing Framework to Unfold Processing Efficiencies for Large and Multiscale Remotely Sensed Data, with Examples on Landsat 8 and MODIS Data**

Hai Lan , Xinshi Zheng , and Paul M. Torrens

Research Article (12 pages), Article ID 2075057, Volume 2018 (2018)

## **Weighted Voronoi Diagram-Based Simulation and Comparative Analysis of Ecosystem Service Coverage: Case Study of the Zhongyuan Urban Agglomeration**

Pengyan Zhang, Wenlong Jing , and Yunzeng Chen 

Research Article (11 pages), Article ID 7147524, Volume 2018 (2018)

## **Detection of *Firmiana danxiaensis* Canopies by a Customized Imaging System Mounted on an UAV Platform**

Chun Liu , Mengchi Ai , Zhuo Chen , Yuan Zhou, and Hangbin Wu 

Research Article (12 pages), Article ID 6869807, Volume 2018 (2018)

## **A Research on the Combination Strategies of Multiple Features for Hyperspectral Remote Sensing Image Classification**

Yuntao Ma, Ruren Li , Guang Yang, Lishuang Sun, and Jingli Wang

Research Article (14 pages), Article ID 7341973, Volume 2018 (2018)

## **Error Compensation Technique for a Resistance-Type Differential Pressure Flow Sensor**

Guimei Wang , Tao Chu , Lijie Yang , and Fang Sun 

Research Article (7 pages), Article ID 8642708, Volume 2018 (2018)

## Editorial

# Remote Sensing of Sustainable Ecosystems

Yichun Xie <sup>1</sup>, Zongyao Sha <sup>2</sup>, and Victor Mesev <sup>3</sup>

<sup>1</sup>*Institute for Geospatial Research & Education, Eastern Michigan University, Ypsilanti, USA*

<sup>2</sup>*School of Remote Sensing & Information Engineering, Wuhan University, Wuhan, China*

<sup>3</sup>*Department of Geography, Florida State University, Tallahassee, USA*

Correspondence should be addressed to Yichun Xie; [yxie@emich.edu](mailto:yxie@emich.edu)

Received 21 October 2018; Accepted 22 October 2018; Published 13 November 2018

Copyright © 2018 Yichun Xie et al. This is an open access article distributed under the Creative Commons Attribution License, which permits unrestricted use, distribution, and reproduction in any medium, provided the original work is properly cited.

## 1. Introduction

Ecosystems, containing biotic and abiotic elements, are complex communities that impact all aspects of the environment. Their equilibrium and sustainability are paramount to their functionality, health, and survival. Remote sensing and other advanced geospatial data acquisition and processing techniques are critical for the measurement of sustainable ecosystems. This special issue includes the latest advancements in remote sensor systems and computing platforms that have made it possible to collect data on ecosystems quickly and routinely. In particular, there is an increasing volume of multispectral and hyperspectral data from unmanned aerial vehicles (UAV), airborne and satellite sensors. They provide rich information for mapping, monitoring, and analyzing a wide range of ecological applications. Big datasets from various remotely sensed platforms are essential for understanding the science behind ecosystem functions and thus provide critical insights on how ecosystems are sustainable.

## 2. Remote Sensing of Sustainable Ecosystems

This special issue was proposed as a follow-up to GSES (Geoinformatics in Sustainable Ecosystem and Society) conference at Wuhan University, China, in September 2017. The forum covered diverse topics centering on advances in earth observation, geospatial analysis, and technologies and their applications in natural resource management and sustainable society. We received 18 papers submitted to this special issue, 6 of which were accepted and published after peer review

(one-third acceptance rate). What binds the papers are themes for spatial observation (using ground-based in-situ sensors or moving sensors) for acquiring information on key ecosystem elements and innovative data assimilation strategies to improve our understanding of the interactions of those elements within or between ecosystems. The 6 accepted papers focus on the design of systematic data acquisition frames, the approaches for processing and extracting ecosystem-related datasets, and the models for understanding the science behind some ecosystems. In summary, the topics illustrated by the published papers include the following:

- (i) Advanced image processing and geostatistical techniques for analyzing and classifying hyperspectral data
- (ii) Calibrating unmanned aerial vehicles using hyperspectral and digital surface models
- (iii) Accessing unlimited cloud computing resources for storing and transforming multisource data
- (iv) Big data analytics based on spatial modeling and machine learning to understand the science for promoting sustainable ecosystem services
- (v) Measuring leaf dust retention across visible and infrared wavelengths
- (vi) Application of Voronoi diagrams for simulation
- (vii) Mapping rare and protected ecosystem service capacities more accurately

### **Conflicts of Interest**

Based on my best knowledge, I and my co-guest editors of this special issue have no conflict of interest.

### **Acknowledgments**

We would like to thank all the authors for their valuable contributions in this special issue as well as all the reviewers whose constructive suggestions helped to improve the quality of the papers and the publication of this special issue. We also thank Wuhan University, China, and Eastern Michigan University, USA, for co-organizing the International Conference on Geoinformatics in Sustainable Ecosystem and Society (GSES-2017) which provided the source for most of the submitted papers to this special issue.

*Yichun Xie  
Zongyao Sha  
Victor Mesev*

## Research Article

# Machine Learning for Estimating Leaf Dust Retention Based on Hyperspectral Measurements

Wenlong Jing<sup>1,2,3</sup>, Xia Zhou<sup>1,2,3</sup>, Chen Zhang<sup>1,2,3,4</sup>, Chongyang Wang<sup>1,2,3</sup>  
and Hao Jiang<sup>1,2,3</sup>

<sup>1</sup>Guangzhou Institute of Geography, Guangzhou, China

<sup>2</sup>Key Laboratory of Guangdong for Utilization of Remote Sensing and Geographical Information System, Guangzhou, China

<sup>3</sup>Guangdong Open Laboratory of Geospatial Information Technology and Application, Guangzhou, China

<sup>4</sup>Shandong University of Science and Technology, Shandong, China

Correspondence should be addressed to Wenlong Jing; [jingwl@reis.ac.cn](mailto:jingwl@reis.ac.cn)

Received 13 April 2018; Revised 7 June 2018; Accepted 26 June 2018; Published 6 September 2018

Academic Editor: Zongyao Sha

Copyright © 2018 Wenlong Jing et al. This is an open access article distributed under the Creative Commons Attribution License, which permits unrestricted use, distribution, and reproduction in any medium, provided the original work is properly cited.

Hyperspectral sensors provide detailed information for dust retention content (DRC) estimation. However, rich hyperspectral data are not fully utilized by traditional image analysis techniques. We integrated several recently developed machine learning algorithms to estimate DRC on plant leaves using the spectra measured by the ASD FieldSpec 3. The experiments were carried out on three common green plants of southern China. The important hyperspectral variables were first identified by applying the random forest (RF) algorithm. Three estimation models were then developed using the support vector machine (SVM), classification and regression tree (CART), and RF algorithms. The results showed that the increase in dust retention contents on plant leaves enhanced their reflectance in the visible wavelength but weakened their reflectance in the infrared wavelength. Wavelengths in the ranges of 450–500 nm, 550–600 nm, 750–1000 nm, and 1100–1300 nm were identified as important variables using the RF algorithm and were used to estimate the DRC. The comparison of the three machine learning techniques for DRC estimation confirmed that the SVM and RF models performed well because their estimations were similar to the measured DRC. Specifically, the average  $R^2$  for SVM and RF model are 0.85 and 0.88. The technical approach of this study proved to be a successful illustration of using hyperspectral measurements to estimate the DRC on plant leaves. The findings of this study can be applied to monitor the DRC on leaves of other plants and can also be integrated with other types of spectral data to measure the DRC at a regional scale.

## 1. Introduction

Haze has been an increasing air pollution issue with the rapid industrialization and urbanization of China [1, 2]. Urban green plants play a significant role in improving the urban atmospheric environment by retaining dust [3–5]. Measurement of the dust retention capacity of green plants is helpful for monitoring and controlling urban air pollution [6, 7]. It is also valuable for evaluation of the influence of green plants upon the urban atmospheric environment, further directing the arrangement and management of urban green plants [8, 9].

The mass difference method is the most basic measuring approach of dust retention content (DRC) of plants [10, 11]. However, this method is complicated and time-consuming. In addition, the monitoring of DRC at the regional scale is

impossible using the mass difference method. Remotely sensed hyperspectral technology has provided an efficient way for monitoring effects of environmental pollution on plants by measuring plant spectral characteristics [12–15]. Previous studies have investigated the influence of dust upon the spectral curve and characteristics of plants [16, 17]. According to Horler et al. [18], dust retention on leaves leads to a change in the red edge position, but experiments conducted by Xiao [19] showed that dust retention has no impact on the red edge position. The red edge position, according to Wang et al. [20], is not sensitive to the influence of detained dust on leaves, but the red edge slope and the area of the spectra of dust-covered leaves are smaller than those of dust-less leaves. In summary, the spectral characteristics of clean leaves differ from those of dust-covered leaves, which

TABLE 1: Physical characteristics of the leaf surface.

Plants	Color	Characteristics of the leaf surface Size	Shape	Texture	Microscopic feature	Dust retention feature
GL	Golden yellow or glossy dark green	3–8 cm	Ellipse	Leathery, fleshy and entire leaf, two sides smooth and glabrous	Many depressions in leaf caused by unequal-sized graininess wax, that lots of particle can adhere to them	Massive stratification
LC	Dull-red or green	2–5 cm	Oval or oblate ellipsoid, round root but deflect, asymmetric	Leathery and entire leaf, stellate leaf trichome in two sides	Rough leaf surface with villus	Mosaic particle
CF	Green or purplish red	25–50 cm	Ellipse to elliptical lanceolate	Smooth leaf surface	Cell profile distinct and aligned	Sporadic mosaic particle

makes it possible to estimate the DRC of plant leaves based on remotely sensed spectral information [12, 19, 21, 22].

Spectral information provided by hyperspectral measurement devices or sensors commonly includes hundreds of bands. Selecting the appropriate bands for a DRC estimation model is significant. The normalized difference vegetation index (NDVI), three-edge (blue, red, and yellow) positions, and slopes for use in constructing a DRC estimation model have been assessed through experimentation by some scholars [21, 23–25]. These variables, however, are mostly selected empirically; considerable useful information was excluded. Univariate/multiple linear regression and the partial least squares regression algorithm have been investigated to simulate the relationship between the DRC and spectral characteristics [16]. However, few studies have been conducted using machine learning. Machine learning, as a powerful modeling tool, has successfully improved the estimation and classification accuracy of environmental variables (air pollution, vegetation health condition, soil moisture, land surface temperature, etc.) and land cover types from remotely sensed images [26–32]. In addition, machine learning algorithms are excellent in solving nonlinear problems of variables with very high dimensions. Therefore, this study attempted to investigate the possibilities of constructing an estimation model for DRC using machine learning algorithms.

The objectives of this study were to (1) investigate the effects of the DRC on the spectral characteristics of leaf surfaces, (2) extract important bands from hyper spectra to reduce the very high dimensions of the variables and further evaluate the effectiveness of the selected bands, and (3) construct a DRC estimation model using machine learning algorithms. In this study, we conducted the experiments on three commonly planted green plants in southern China, and the spectra were measured using an ASD FieldSpec 3 device. Three machine learning regression algorithms were used for DRC estimation model construction for comparison purposes.

## 2. Materials and Methods

*2.1. Experimental Plants and Sampling Collection.* For the research purpose, three plants were chosen as study objects,



FIGURE 1: In situ experiment.

including *Ficus microcarpa* L. f. cv Golden leaves (GL), *Loropetalum chinense* (R. Br) Oliv. var. rubrum Yieh (LC), and *Cordyline fruticosa* (L.) A. Cheval (CF). These plants are the most common and typical green plants in southern China; investigation on these plants is beneficial to promoting the simulation of DRC to regional scale in the experiment area. Moreover, as is shown in Table 1, the leaves of three plants have different characteristics on color, size, shape, and surface texture. This is also helpful in detecting the usefulness and possibilities of simulating the DRC by using a machine learning algorithm on different plant leaves. To reduce the influence of extreme rainfall and wind, the plants were planted under an open greenhouse in Guangzhou (Figure 1). Figure 2 shows the three plants and their leaves.

Ten experiments were carried out from October 2017 to January 2018. Before the experiments, the plants were sufficiently washed to ensure a dust-free state on the leaves. Later, the leaves of the three plants were collected at an interval of 5–7 days on cloudless days. Leaves of similar health and age conditions were collected at the top, middle, and bottom of the canopy, respectively, and then sealed in sampling bags for the measurement of dust retention. Considering the different sizes of the leaves, the number of leaves collected for each plant was different. Among these, there were 30 pieces for GL, 50 pieces for LC, and 5 pieces for CF. Three replicate measurements were taken each time.



FIGURE 2: The three plants and their leaves.

## 2.2. Measurement of Leaf Reflectance Spectra and Dust Content

**2.2.1. Measurement of Leaf Reflectance Spectra.** Spectral measurements were recorded for each plant before and after dust retention to obtain the precise measurement of dust-related spectral changes. In the study, an ASD FieldSpec 3 spectrograph was used to measure the spectral reflectance of the leaves. The equipment was based on the basic theory of electromagnetic waves. The optical probe collected the electromagnetic waves reflected from the ground objects, which were later transformed into digital signals. The spectral range of this spectrograph was 350–2500 nm and with a sampling interval of 1 nm. The measuring speed was fixed at 0.1 s. The length of the optical probe was 1 m. The front field angle was 25°. The reflectance, radiation, and irradiance of the ground objects were simultaneously collected.

At the same time of leaf collection, the spectral reflectance was measured from 10:00 to 14:30. The front sides of five leaves were both measured and repeated five times. After measurement, the leaves were sealed in corresponding bags and used to measure the DRC with the collected leaves. The probe should be perpendicular to the leaf, and the height should change according to the leaf size to guarantee spectrometer probe falls within the scope of the leaf. Specifically, the height from the probe to the leaf surface is calculated based on the equation as follows:

$$H \leq \frac{W_L/2}{\tan \theta/2}, \quad (1)$$

where  $H$  is the height,  $W_L$  is the width of the leaf, and  $\theta$  is the front field angle. Considering that the leaf size for one plant could also be different, we take the minimum width of each plant type as  $W_L$  when calculating the height. For GL and LC, we take 2 cm as  $W_L$ , then  $H$  is less equal to 4.5 cm; for CF, we take 20 cm as  $W_L$ , then  $H$  is less equal to 45 cm. In practice, we used  $H$  of 4 cm for GL and LC, and 10 cm for CF.

**2.2.2. Measurement of Dust Content.** In this study, the plant's dust retention ability is represented by the dust content per unit leaf area, which is measured by the ratio of the leaf dust content and unit leaf area within a certain time [6]. The leaf dust content is measured by the weight difference method, and the unit leaf area is measured using a leaf area meter.

The first procedure of the weight difference method is washing the leaves and then drying them. The weights of the two conditions should be measured, and the difference is considered to be the dust content. To avoid other effects on the experiment, the control variate method was used in this research. That means except for the liquid in the beaker, the soak time, dried water, drying temperature, drying time, and cooling time were the same. The detailed method is as follows:

- (1) The collected leaves were sealed in a dried and weighted beaker ( $W1$ ) corresponding to the bags, then soaked in pure water for 5–6 hours. At the same time, the sampling bag was washed using pure water and then poured into a beaker.
- (2) The beaker was stirred with a clean glass rod to make the dust dissolve into the water. Then, the leaves were sufficiently washed twice using a tweezer and pure water. After washing, the tweezer and glass rod were washed, and the flushing water was poured into the soak beaker.
- (3) The beaker was placed in the drying apparatus, and the temperature was set to 85°C and the drying time set to 25 hours. After drying, the beaker was placed in a drying vessel for 5 hours to cool down.
- (4) The leaves were weighted ( $W2$ ) using a ten-thousandth electronic analytical balance. The difference weight ( $\Delta W = W2 - W1$ ) is the dust retention of the collected sample. The leaf area on the dried clean leaves of each bag was measured using the leaf area meter device. The ratio of dust retention  $\Delta W/\text{leaf area } S$  is the unit leaf dust retention value.

**2.3. Spectral Data Process.** Before the spectral characteristic analysis, the noise and nonsensitive wave band needed to be removed from the collected spectral data, and the spectral transformation should be completed for the following research. First, to ensure the accuracy of the spectral measured data, we examined the five-times repeated spectral data of each point and removed the evident deviated curves. Then, the mean value was calculated. Second, to ensure the comparability of the measured data from different times and conditions and eliminate errors caused by the experimental environment, we divided it by the white board reflectance because the spectral reflectance should follow the principle of proximity. Then, we removed the bands that were assimilated by water vapor because water vapor assimilation has a great effect on the spectral curve, and this wavelength band range is meaningless in botany spectral research. To simplify the following data process, the wave bands were removed directly during this research. The result is shown in Figure 3.

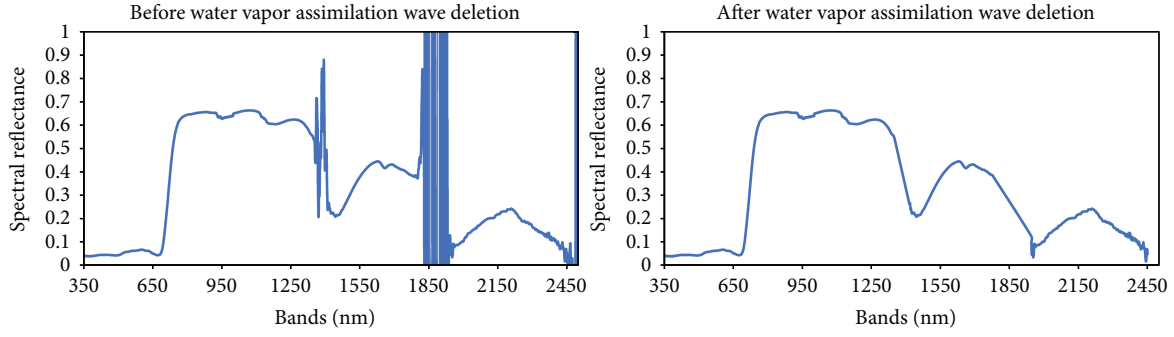


FIGURE 3: Comparison before and after water vapor assimilation wave deletion.

The first derivative spectra can reduce sublinear and quadratic background noise; it can also reduce the impact of the hyperspectral remote-sensing measurement because of the scattering and absorption of atmosphere to light [33]. It is also able to reduce the impact of multiplicative factors that are produced by changing lighting conditions [22]. Therefore, the first derivative spectra computed from the original measured reflection spectra were implemented to establish the estimation model of the DRC. The equation of the first derivative (dR) is expressed as follows:

$$dR(\lambda_i) = \frac{R(\lambda_{i+1}) - R(\lambda_{i-1})}{\lambda_{i+1} - \lambda_{i-1}}. \quad (2)$$

$\lambda_{i+1}$ ,  $\lambda_i$ , and  $\lambda_{i-1}$  are the adjacent wavelengths;  $dR(\lambda_i)$  is the first derivative of wavelength  $\lambda_i$ ;  $R(\lambda_{i+1})$ ,  $R(\lambda_i)$ , and  $R(\lambda_{i-1})$  are the original reflectance of the wavelengths  $\lambda_{i+1}$ ,  $\lambda_i$ , and  $\lambda_{i-1}$ , respectively.

#### 2.4. Identifying Feature Importance and Estimating the DRC.

In this section, we present our key innovation: integrating machine learning algorithms to identify the important spectral features (bands). We estimated the DRC based on these selected features and compared the effectiveness of the various machine learning algorithms. Our design is depicted in Figure 4.

**2.4.1. Identifying Feature Importance.** The first derivative spectra were computed from the original measured reflection spectra. Over a thousand independent variables are provided in the original sample datasets. A feature selection needed to be conducted on the very high-dimensional datasets to exclude the redundant bands, further reducing the dimension of the sample sets. In this study, we implemented random forest (RF) to measure the feature importance (FI) of each band [34–36]. The FI values were then sorted from highest to lowest, and the cumulative value of 0.9 was used to derive the important variables.

RF is an outstanding ensemble learning algorithm. The basic concept of the algorithm is to construct numerous tree-based predictors to obtain better performance [37, 38]. A number of subsets are extracted randomly from the total sample with replacement. The remaining samples are out-of-bag data (OOB). Then, a classification and regression tree (CART) was generated at each subset. The prediction was obtained by averaging all the outputs from the prediction of

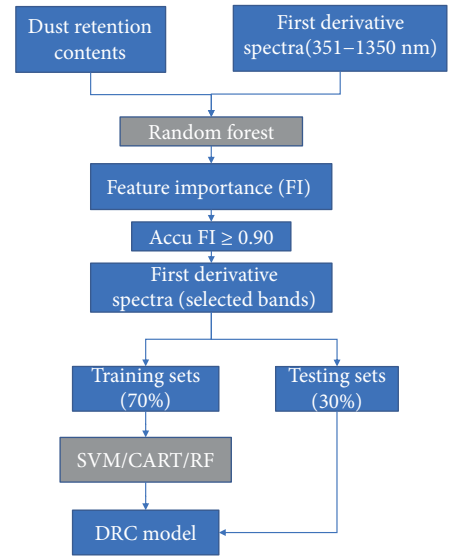


FIGURE 4: Flowchart of the DRC estimation model.

each subset. The feature importance of the bands can be described as follows:

- (1) The OOB of each subset were used to test the estimation of the corresponding tree, and the average errors of the OOB of all trees were calculated.
- (2) The order of values of the  $k$ th variable was permuted while the other variables remain unchanged.
- (3) The OOB error of the permuted set was calculated.
- (4) The difference in the OOB error before and after the permutation was calculated for each variable, and the differences of all the variables were then normalized to a range of from 0 to 1.0, which were the FI values of the variables.

**2.4.2. Model for DRC Estimation.** The DRC estimation model was established based on the selected variables. Three commonly used machine learning algorithms were used to construct the models between DRC and first derivative spectra. SVM, as a supervised learning algorithm, has performed well in many remote-sensing applications [39–42]. CART, as a tree-based algorithm, is easily implemented and has been

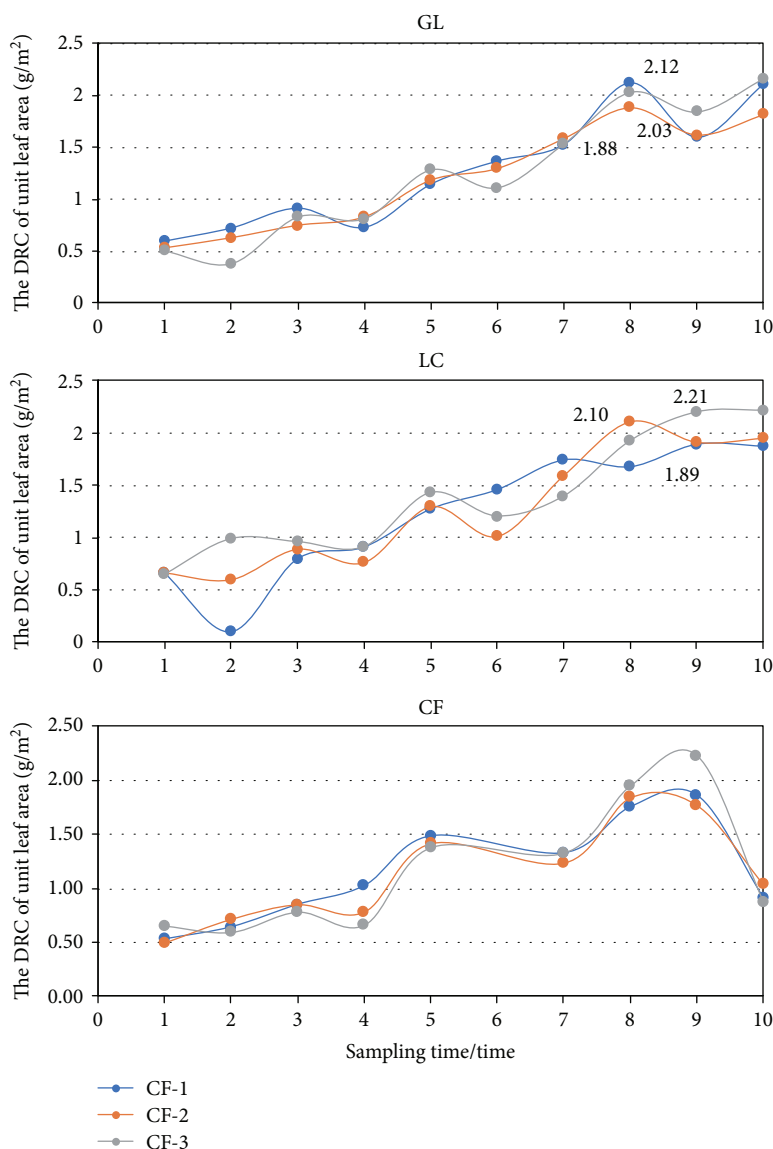


FIGURE 5: Temporal changes in unit DRC of the three green plants.

widely used in a variety of fields [43–45]. The aforementioned RF algorithm, which has been used for variable selection, was also implemented to model the DRC. These three machine learning algorithms were selected for comparison of their effectiveness in establishing the DRC estimation model because of their extensive use, good performance, and easy implementation. For validation purposes, the total sample set was randomly divided into two subsets, with the 70% part used to train the model and the 30% part set aside for testing.

### 3. Results and Discussion

**3.1. Spectral Characteristics.** Figure 5 shows the temporal changes in the unit DRC of the three green plants. It was found that the unit DRC increases with time but tends to remain stable or decrease because of a saturation effect after a long time. In addition, it was also found that the dust retention capability of CF is the most significant among the three

green plants, with a mean unit DRC of 2.23 g/m<sup>3</sup>, followed by that of LC (2.21 g/m<sup>3</sup>). The dust retention capability of GL was the lowest at 2.12 g/m<sup>3</sup>. The DRC of plant leaves, as a result, increased temporally and reached saturation after a certain time, without rainfall and wind disturbance.

In general, the reflectance of the three green plants with or without dust on the leaves showed a universal characteristic, which is similar to the reflectance of many other plants. Due to the pigment absorption of the plants, the reflectance of the three green plants in the visible wavelength is low (less than 20%) and they usually have a reflection peak (at approximately 550 nm for GL and LC and approximately 600 nm for CF). The reflectance in the infrared band is high (greater than 60%) as contributed by the structure of the plants' leaves.

For the same plant, the reflectance of the leaves with dust and those that are clean was significantly different, particularly in the visible-infrared wavelength (Figure 6). Compared to the reflectance of clean leaves, that of the dust-covered

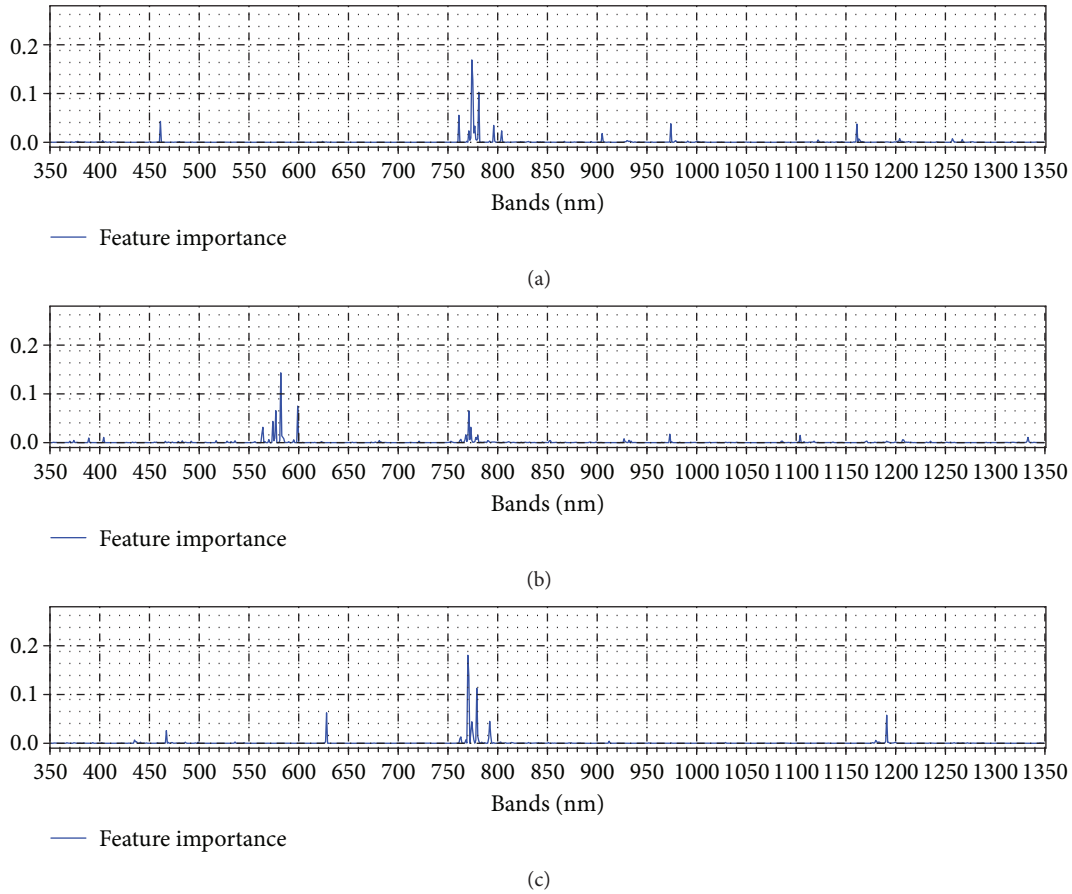


FIGURE 6: Feature importance of different bands calculated using RF for each plant: (a) GL, (b) LC, and (c) CF.

leaves in the visible wavelength markedly increased by more than 70%. It is well known that the reflectance of plant leaves in the visible wavelength is dependent on the absorption and reflection of the leaves' pigments. The dust retention on the leaves not only influences the pigment absorption but also increases the leaves' reflection, which causes high reflectance in the visible wavelength.

However, the reflectance of dust-covered leaves in the infrared wavelength is significantly lower than that of the clean leaves. The main reason is that dust on the leaves can decrease multiple reflections in the leaves' structure, particularly of CF (Figure 7). The characteristic of the reflectance in the shortwave infrared wavelength of the three green plants with or without dust on the leaves is random, because the reflectance in the shortwave infrared wavelength of the leaves was mainly affected by leaf water. Dust retention had little impact on leaf water (Figure 7).

Based on the aforementioned analysis, it was found that significant correlations between the reflectance in the visible-infrared wavelength of the plant leaves and dust retention exist. Thus, it is possible to establish a model for estimating the DRC on plant leaves by using spectral information.

### 3.2. Dust Retention Estimation Model

**3.2.1. Band Selection Results.** As in the aforementioned analysis, the reflectance in the shortwave infrared wavelength of

the leaves was mainly affected by leaf water and only slightly influenced by dust retention. Therefore, we only included spectra between the wavelengths of 351 and 1350 nm. There is a total of 1000 bands from the 351 nm to 1350 nm wavelength with an interval of 1 nm. As a result, 1000 independent variables were provided in the sample datasets.

The RF regression algorithm was run for the total samples for each plant, respectively. FI values of bands in a range of 351–1350 nm were then derived from the algorithm outputs. Figure 6 presents the distribution of FI estimated using RF at different bands. It can be seen that FI values for the three plants show a different distribution pattern. Overall, the FI for the three plants all reach peak values between a wavelength of 750 nm and 800 nm, which are the near infrared bands that are sensitive to vegetation health [46]. However, for GL and CF, the high FI values are mainly concentrated between 750 nm and 800 nm, whereas the FI values of LC range from 550 to 600 nm and overwhelm those of the near infrared bands. In addition, FI values also occur at 460 nm and 630 nm for GL and CF, respectively.

The FI values were then sorted from highest to lowest; we then accumulated the FI values from highest to lowest. The accumulating was stopped when the accumulated FI value reached 0.9. Then the bands that have been accumulated were considered as important variables and selected to establish the DRC model. Figure 8 shows the selected bands for each plant based on the threshold of 0.9 for the cumulative

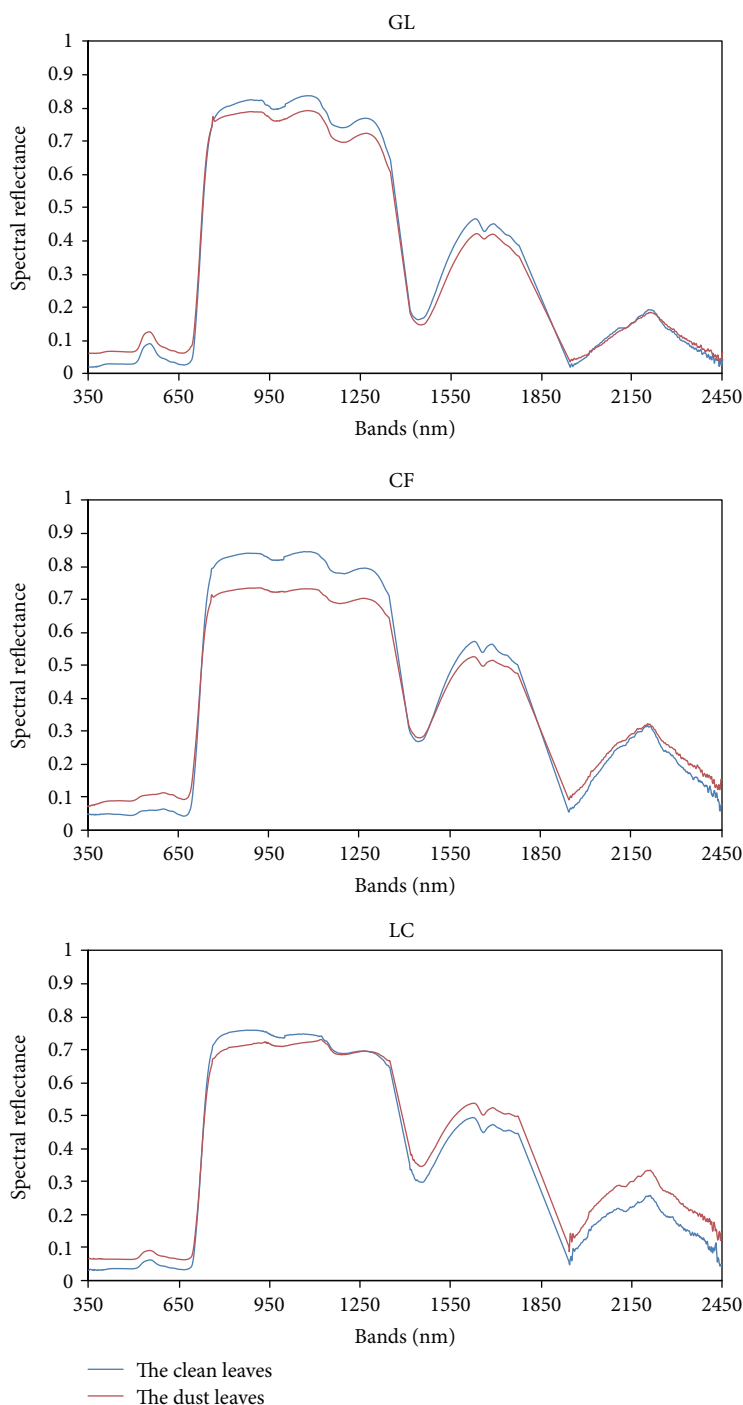


FIGURE 7: Reflectance of dust-covered and clean leaves.

FI value. The number of selected bands for GL, LC, and CF is 94, 167, and 73, respectively, much less than the total number of samples. Because the distribution of FI values for three plants is different, the number of selected bands is different. For GL and CF, the selected bands are mainly in the ranges of 350–500 nm, 750–900 nm, and 1100–1350 nm. For LC, except for the same ranges of GL and CF, many bands were also selected from 550 to 600 nm and 650 to 700 nm.

In theory, the spectra of the selected bands can provide 90% of the information of the total samples. The selected

bands were included as independent variables to establish an estimation model for DRC.

**3.2.2. Dust Retention Model.** The total sample set was divided into two subsets randomly, with the 70% part used to train the model and the 30% part set aside for testing. Models were established for each plant independently based on the selected bands. Moreover, models were also established using the total bands for comparison purposes. Table 2 summarizes the training and test results for each plant using the CART,

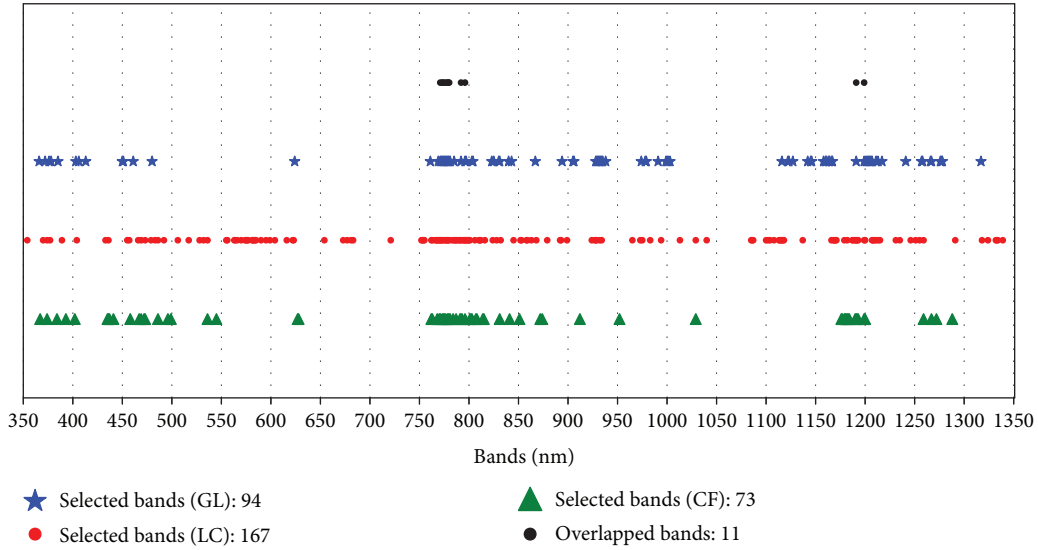


FIGURE 8: Distribution of selected bands based on the FI values for each plant.

TABLE 2: Training and testing results for three plants using the different regression algorithms.

Plants	Algorithms	Number of bands	Training				Number of samples	Testing				Number of samples
			$R^2$	MAE ( $\text{g/m}^2$ )	RMSE ( $\text{g/m}^2$ )	Bias		$R^2$	MAE ( $\text{g/m}^2$ )	RMSE ( $\text{g/m}^2$ )	Bias	
GL	CART	1000	0.98	0.04	0.08	0.00	99	0.78	0.17	0.26	0.05	42
		94	0.95	0.08	0.13	0.00		0.76	0.18	0.26	0.04	
	RF	1000	0.98	0.07	0.10	0.00		0.88	0.14	0.19	0.05	
		94	0.98	0.06	0.08	0.00		0.92	0.11	0.15	0.03	
LC	SVM	1000	0.97	0.08	0.09	-0.01	97	0.89	0.14	0.19	0.05	41
		94	0.92	0.13	0.16	0.00		0.89	0.16	0.19	0.07	
	CART	1000	0.97	0.05	0.10	0.00		0.50	0.33	0.47	-0.06	
		167	0.95	0.07	0.12	0.00		0.50	0.29	0.46	-0.03	
CF	RF	1000	0.97	0.08	0.11	0.00	94	0.83	0.17	0.23	-0.03	41
		167	0.98	0.07	0.10	0.00		0.87	0.14	0.20	-0.02	
	SVM	1000	0.97	0.09	0.10	-0.01		0.80	0.17	0.23	-0.02	
		167	0.95	0.11	0.13	0.00		0.77	0.20	0.25	-0.01	
CF	CART	1000	0.93	0.08	0.13	0.00	94	0.64	0.20	0.31	0.00	41
		73	0.98	0.04	0.07	0.00		0.70	0.17	0.29	0.03	
	RF	1000	0.97	0.06	0.09	0.00		0.80	0.16	0.23	0.02	
		73	0.98	0.05	0.08	0.00		0.84	0.14	0.21	0.02	
SVM	1000	0.97	0.06	0.08	0.01	0.90	0.13	0.17	0.03			
	73	0.97	0.08	0.08	0.00	0.88	0.14	0.18	-0.01			

SVM, and RF methods, respectively. Figures 9 and 10 show the scatter plots between the estimated and measured dust amount by model using the selected bands and total bands, respectively.

In general, the models established based on selected and total bands both achieved high accuracy, with a similar coefficient of determination ( $R^2$ ), mean absolute error (MAE), and root mean square error (RMSE). The testing results also imply that the models implementing the selected bands produced comparable performance to that of the models

considering total bands. The RF-based models for LC and GL using selected bands produced evidently higher  $R^2$  values than those using the total bands. This indicates that dimensionality reduction is necessary, and the selected bands preserve important and useful information that could express the spectral differences of the leaves caused by dust retention.

For LC and GL, the RF-based model performed better than the other two algorithms, with a testing  $R^2$  of 0.87 and 0.92, respectively. The bias values for the models are all less than 0.08. For CF, the SVM-based model outperformed the

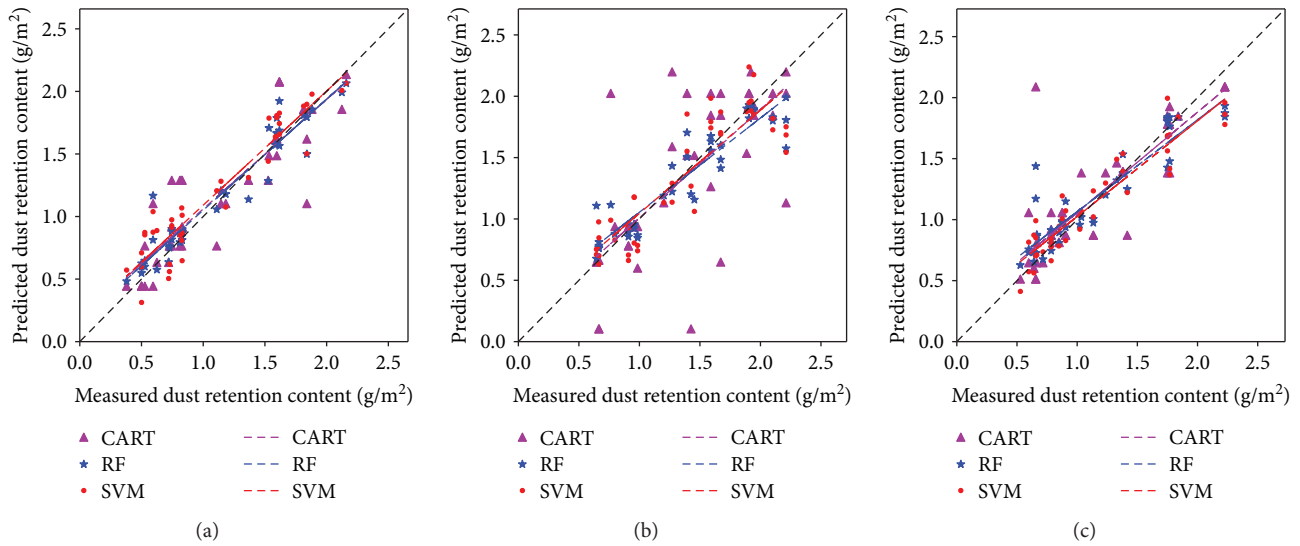


FIGURE 9: Scatter plots of estimated and measured DRC based on selected bands: (a) GL, (b) LC, and (c) CF.

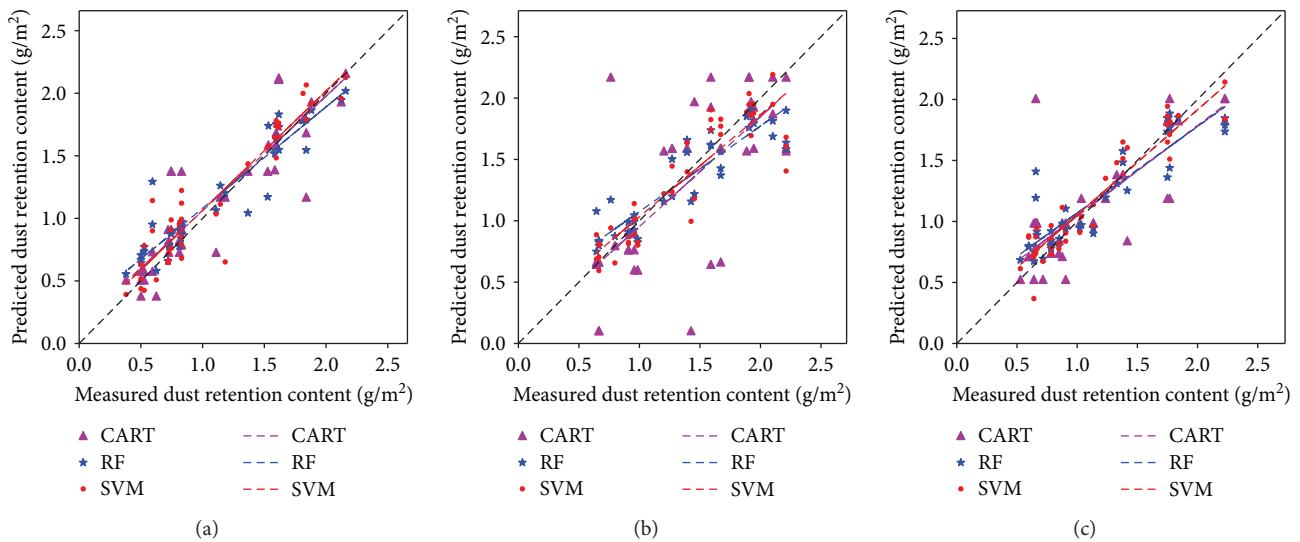


FIGURE 10: Scatter plots of estimated and measured DRC based on total bands: (a) GL, (b) LC, and (c) CF.

other two algorithms. Overall, the CART-based model produced the least accurate estimation results. Figure 11 shows the Taylor diagrams of testing accuracy for the three plants. The Taylor diagram is helpful for comparative assessment of different models. It integrates four statistics on a diagram to quantify the degree of correspondence between the modeled and observed values. The four statistics are the Pearson correlation coefficient, normalized standard deviation, normalized error standard deviation, and normalized bias. The measured (observed) values serve as the reference. More details can be found in [47]. According to Figure 11, the estimated results produced by the CART-based model show the lowest correlations with the measured values. The results estimated using the SVM and RF models show similar standard deviations and correlations. In addition, the three algorithms all underestimated the measured dust contents of LC.

## 4. Conclusion

In this study, we investigated the effectiveness of using machine learning to estimate the DRC of leaves based on remotely sensed hyperspectral information. We conducted experiments on three green plants in southern China. The spectra were measured using an ASD FieldSpec 3. A feature selection process was implemented to reduce the high dimensions of the original spectra. Three commonly used machine learning algorithms, SVM, CART, and RF, were used to detect the possible relationships between the DRC and the first derivative spectra. The conclusions can be summarized as follows:

- (1) Significant correlations exist between spectral reflection and the DRC of the plant leaves in the visible-infrared wavelength region: the reflectance of the plant leaves increases in the visible wavelength and

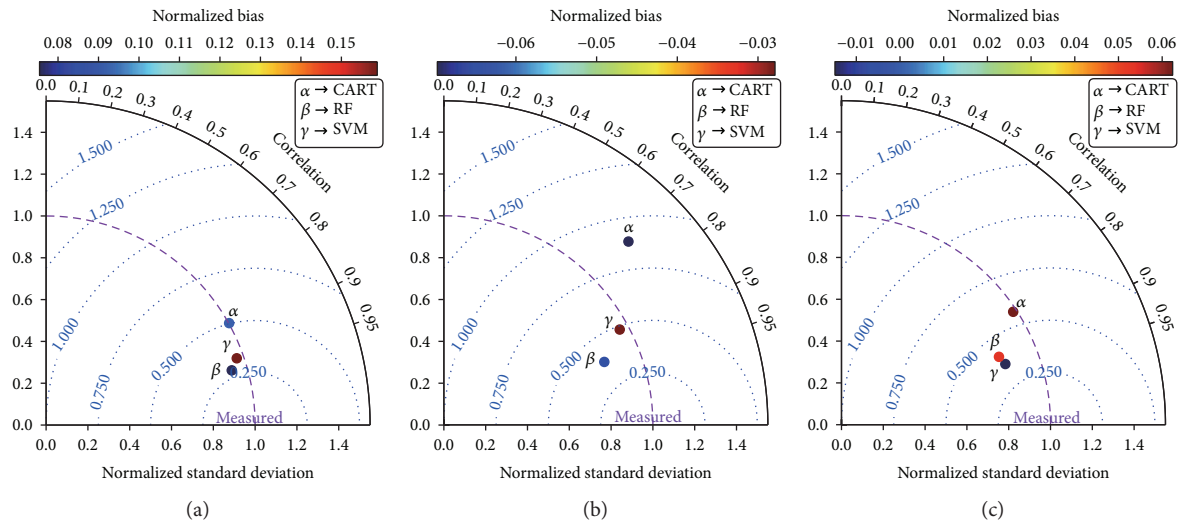


FIGURE 11: Taylor diagrams showing the correlations between the estimated DRC of the different models and the measured values of (a) GL, (b) LC, and (c) CF.

decreases in the infrared wavelength with increase in DRC. The characteristic of the reflectance in the shortwave infrared wavelength of the three green plants with or without dust on the leaves is random because the reflectance at these wavelengths is mainly affected by leaf water content.

- (2) Spectra from 450 to 500 nm, 550 to 600 nm, 750 to 1000 nm, and 1100 to 1300 nm are recommended for detecting and estimating the DRC of leaves. However, appropriate bands differ among plants. The experiments in this study were only conducted on three types of plants; a feature selection process is recommended in any other practical applications.
- (3) The RF algorithm reduced the variable dimensions well. Testing results showed that the estimated values using the SVM and RF approaches had good agreement with the measured DRC. SVM and RF, as a result, are recommended for modeling DRC based on hyperspectral data. Optimal algorithms should be determined based on different situations.

This study provided a technical approach for estimating DRC on plant leaves based on hyperspectral measurements. The validation results showed that the machine learning model proposed in this study efficiently reduced the variable dimensions and accurately estimated the DRC of different plants. Consequently, the results of this study can be applied to monitor the DRC on leaves of other plants and further be fused or integrated with other types of spectral data to measure the DRC at a regional scale based on airborne hyperspectral sensors or sensors onboard unmanned aerial vehicles (UAVs).

## Acronyms

CART: Classification and regression tree  
 CF: *Cordyline fruticosa* (L.) A. Cheval  
 DRC: Dust retention content

FI: Feature importance  
 GL: *Ficus microcarpa* L. f. cv Golden leaves  
 LC: *Loropetalum chinense* (R. Br) Oliv. var. rubrum Yieh  
 MAE: Mean absolute error  
 NDVI: Normalized difference vegetation index  
 OOB: Out-of-bag data  
 $R^2$ : Coefficient of determination  
 RF: Random forest  
 RMSE: Root mean square error  
 SVM: Support vector machine.

## Data Availability

The hyperspectral measurements and the dust retention content data used to support the findings of this study are available from the corresponding author upon request.

## Conflicts of Interest

The authors declare that there is no conflict of interest regarding the publication of this paper.

## Authors' Contributions

Wenlong Jing and Xia Zhou contributed equally to this work.

## Acknowledgments

This study was jointly supported by the National Natural Science Foundation of China (41401430 and 41771380), the Guangdong Innovative and Entrepreneurial Research Team Program (2016ZT06D336), the Guangdong Academy of Sciences' Special Project of Science and Technology Development (2017GDASCX-0101 and 2018GDASCX-0904), the Forest Science and Technology Innovation in Guangdong (2015KJCX047), the Science and Technology Program of Guangzhou (201604016047), and the Science and Technology Program of Guangdong Province (2017B010117008).

## References

- [1] R. J. Huang, Y. Zhang, C. Bozzetti et al., “High secondary aerosol contribution to particulate pollution during haze events in China,” *Nature*, vol. 514, no. 7521, pp. 218–222, 2014.
- [2] S. Guo, M. Hu, M. L. Zamora et al., “Elucidating severe urban haze formation in China,” *Proceedings of the National Academy of Sciences of the United States of America*, vol. 111, no. 49, pp. 17373–17378, 2014.
- [3] L.-M. Mårtensson, A. Wuolo, A.-M. Fransson, and T. Emilsson, “Plant performance in living wall systems in the Scandinavian climate,” *Ecological Engineering*, vol. 71, pp. 610–614, 2014.
- [4] H. F. Wang, J. X. Qiu, J. Breuste, C. Ross Friedman, W. Q. Zhou, and X. K. Wang, “Variations of urban greenness across urban structural units in Beijing, China,” *Urban Forestry & Urban Greening*, vol. 12, no. 4, pp. 554–561, 2013.
- [5] U. Weerakkody, J. W. Dover, P. Mitchell, and K. Reiling, “Particulate matter pollution capture by leaves of seventeen living wall species with special reference to rail-traffic at a metropolitan station,” *Urban Forestry & Urban Greening*, vol. 27, pp. 173–186, 2017.
- [6] J. Liu, Z. Cao, S. Zou et al., “An investigation of the leaf retention capacity, efficiency and mechanism for atmospheric particulate matter of five greening tree species in Beijing, China,” *Science of the Total Environment*, vol. 616–617, pp. 417–426, 2018.
- [7] Y. C. Wang, “Carbon sequestration and foliar dust retention by woody plants in the greenbelts along two major Taiwan highways,” *Annals of Applied Biology*, vol. 159, no. 2, pp. 244–251, 2011.
- [8] A. Baidourela, Ü. Halik, T. Aishan, A. Abliz, and M. Welp, “Dust retention capacities of urban trees and the influencing factors in Aksu, Xinjiang, China,” *Journal of Desert Research*, vol. 35, pp. 322–329, 2015.
- [9] L. Liu, D. Guan, M. R. Peart, G. Wang, H. Zhang, and Z. Li, “The dust retention capacities of urban vegetation—a case study of Guangzhou, South China,” *Environmental Science & Pollution Research*, vol. 20, no. 9, pp. 6601–6610, 2013.
- [10] V. M. Kretinin and Z. M. Selyanina, “Dust retention by tree and shrub leaves and its accumulation in light chestnut soils under forest shelterbelts,” *Eurasian Soil Science*, vol. 39, no. 3, pp. 334–338, 2006.
- [11] J. Yu and R. Yang, “Analysis on dust retention measurement of common plant leaves in Shenyang,” in *2016 3rd International Conference on Materials Science and Mechanical Engineering*, Windsor, UK, 2016.
- [12] G.-Y. Chi, X.-H. Liu, S.-H. Liu, and Z.-F. Yang, “Spectral characteristics of vegetation in environment pollution monitoring,” *Environmental Science & Technology*, 2005.
- [13] E. Choe, F. van der Meer, F. van Ruitenbeek, H. van der Werff, B. de Smeth, and K. W. Kim, “Mapping of heavy metal pollution in stream sediments using combined geochemistry, field spectroscopy, and hyperspectral remote sensing: a case study of the Rodalquilar mining area, SE Spain,” *Remote Sensing of Environment*, vol. 112, no. 7, pp. 3222–3233, 2008.
- [14] E. J. Emengini, G. A. Blackburn, and J. C. Theobald, “Discrimination of plant stress caused by oil pollution and waterlogging using hyperspectral and thermal remote sensing,” *Journal of Applied Remote Sensing*, vol. 7, no. 1, article 073476, 2013.
- [15] K. Zhao, D. Valle, S. Popescu, X. Zhang, and B. Mallick, “Hyperspectral remote sensing of plant biochemistry using Bayesian model averaging with variable and band selection,” *Remote Sensing of Environment*, vol. 132, no. 10, pp. 102–119, 2013.
- [16] N. N. Luo, W. J. Zhao, and X. Yan, “Impact of dust-fall on spectral features of plant leaves,” *Spectroscopy and Spectral Analysis*, vol. 33, no. 10, pp. 2715–2720, 2013.
- [17] S. Shi, Z. Wu, F. Liu, and W. Fan, “Retention of atmospheric particles by local plant leaves in the mount Wutai scenic area, China,” *Atmosphere*, vol. 7, no. 8, p. 104, 2016.
- [18] D. N. H. Horler, M. Dockray, and J. Barber, “The red edge of plant leaf reflectance,” *International Journal of Remote Sensing*, vol. 4, no. 2, pp. 273–288, 1983.
- [19] S. L. Xiao and Z. X. Chen, “Assessment of effect of the dust covered the foliage on canopy reflectance,” *Chinese Agricultural Science Bulletin*, vol. 23, no. 4, pp. 410–414, 2007.
- [20] T. Wang, Y. Liu, H. Y. Wu, and Y. M. Zuo, “Influence of foliar dust on crop reflectance spectrum and nitrogen monitoring,” *Spectroscopy and Spectral Analysis*, vol. 32, no. 7, pp. 1895–1898, 2012.
- [21] H. F. Wang, N. Fang, X. Yan, F. T. Chen, Q. L. Xiong, and W. J. Zhao, “Retrieving dustfall distribution in Beijing City based on ground spectral data and remote sensing,” *Spectroscopy & Spectral Analysis*, vol. 36, no. 9, pp. 2911–2918, 2016.
- [22] C. Wu and X. Wang, “Research of foliar dust content estimation by reflectance spectroscopy of *Euonymus japonicus* Thunb,” *Environmental Nanotechnology, Monitoring & Management*, vol. 5, pp. 54–61, 2016.
- [23] W. Li, J. Wu, T. Chen, and D. Peng, “Hyperspectral estimation model of dust deposition content on plant leaves,” *Transactions of the Chinese Society of Agricultural Engineering*, vol. 32, no. 2, pp. 180–185, 2016.
- [24] H.-L. Xiao, X.-P. Chen, Q.-Y. Ling, and Z.-X. Zhou, “Analysis of dust detention capability of landscape plants and the hyperspectral remote sensing quantitative models construction of foliage dust detention,” *Resources & Environment in the Yangtze Basin*, vol. S1, pp. 16–19, 2015.
- [25] X. Yan, W. Shi, W. Zhao, and N. Luo, “Estimation of atmospheric dust deposition on plant leaves based on spectral features,” *Spectroscopy Letters*, vol. 47, no. 7, pp. 536–542, 2014.
- [26] S. Ahmad, A. Kalra, and H. Stephen, “Estimating soil moisture using remote sensing data: a machine learning approach,” *Advances in Water Resources*, vol. 33, no. 1, pp. 69–80, 2010.
- [27] E. Burchfield, J. J. Nay, and J. Gilligan, “Application of machine learning to the prediction of vegetation health,” *ISPRS - International Archives of the Photogrammetry, Remote Sensing and Spatial Information Sciences*, vol. XLI-B2, pp. 465–469, 2016.
- [28] K. Hu, A. Rahman, H. Bhugubanda, and V. Sivaraman, “HazeEst: machine learning based metropolitan air pollution estimation from fixed and mobile sensors,” *IEEE Sensors Journal*, vol. 17, no. 11, pp. 3517–3525, 2017.
- [29] J. Nay, E. Burchfield, and J. Gilligan, “A machine-learning approach to forecasting remotely sensed vegetation health,” *International Journal of Remote Sensing*, vol. 39, no. 6, pp. 1800–1816, 2018.
- [30] K. P. Singh, S. Gupta, and P. Rai, “Identifying pollution sources and predicting urban air quality using ensemble learning methods,” *Atmospheric Environment*, vol. 80, no. 6, pp. 426–437, 2013.
- [31] S. Heremans and J. Van Orshoven, “Machine learning methods for sub-pixel land-cover classification in the spatially heterogeneous region of Flanders (Belgium): a multi-criteria

- comparison,” *International Journal of Remote Sensing*, vol. 36, no. 11, pp. 2934–2962, 2015.
- [32] J. Rogan, J. Franklin, D. Stow, J. Miller, C. Woodcock, and D. Roberts, “Mapping land-cover modifications over large areas: a comparison of machine learning algorithms,” *Remote Sensing of Environment*, vol. 112, no. 5, pp. 2272–2283, 2008.
- [33] A. M. Wahbi and S. Ebel, “The use of the first-derivative curves of absorption spectra in quantitative analysis,” *Analytica Chimica Acta*, vol. 70, no. 1, pp. 57–63, 1974.
- [34] J. C.-W. Chan and D. Paelinckx, “Evaluation of random forest and Adaboost tree-based ensemble classification and spectral band selection for ecotope mapping using airborne hyperspectral imagery,” *Remote Sensing of Environment*, vol. 112, no. 6, pp. 2999–3011, 2008.
- [35] K. J. Archer and R. V. Kimes, “Empirical characterization of random forest variable importance measures,” *Computational Statistics & Data Analysis*, vol. 52, no. 4, pp. 2249–2260, 2008.
- [36] C. Strobl, A. L. Boulesteix, A. Zeileis, and T. Hothorn, “Bias in random forest variable importance measures: illustrations, sources and a solution,” *BMC Bioinformatics*, vol. 8, no. 1, p. 25, 2007.
- [37] M. Belgiu and L. Drăguț, “Random forest in remote sensing: a review of applications and future directions,” *ISPRS Journal of Photogrammetry and Remote Sensing*, vol. 114, pp. 24–31, 2016.
- [38] L. Breiman, “Random forests,” *Machine Learning*, vol. 45, no. 1, pp. 5–32, 2001.
- [39] C. Cortes and V. Vapnik, “Support-vector networks,” *Machine Learning*, vol. 20, no. 3, pp. 273–297, 1995.
- [40] M. Chi, R. Feng, and L. Bruzzone, “Classification of hyperspectral remote-sensing data with primal SVM for small-sized training dataset problem,” *Advances in Space Research*, vol. 41, no. 11, pp. 1793–1799, 2008.
- [41] G. M. Foody and A. Mathur, “The use of small training sets containing mixed pixels for accurate hard image classification: training on mixed spectral responses for classification by a SVM,” *Remote Sensing of Environment*, vol. 103, no. 2, pp. 179–189, 2006.
- [42] C. Huang, L. S. Davis, and J. R. G. Townshend, “An assessment of support vector machines for land cover classification,” *International Journal of Remote Sensing*, vol. 23, no. 4, pp. 725–749, 2002.
- [43] L. Breiman, J. H. Friedman, R. Olshen, and C. J. Stone, “Classification and regression trees (CART),” *Encyclopedia of Ecology*, vol. 40, no. 3, pp. 582–588, 1984.
- [44] M. A. Friedl, D. K. McIver, J. C. F. Hodges et al., “Global land cover mapping from MODIS: algorithms and early results,” *Remote Sensing of Environment*, vol. 83, no. 1-2, pp. 287–302, 2002.
- [45] L. Giglio, G. R. van der Werf, J. T. Randerson, G. J. Collatz, and P. Kasibhatla, “Global estimation of burned area using MODIS active fire observations,” *Atmospheric Chemistry and Physics*, vol. 6, no. 4, pp. 957–974, 2006.
- [46] E. Ben-Ze'ev, A. Karnieli, N. Agam, Y. Kaufman, and B. Holben, “Assessing vegetation condition in the presence of biomass burning smoke by applying the aerosol-free vegetation index (AFRI) on MODIS images,” *International Journal of Remote Sensing*, vol. 27, no. 15, pp. 3203–3221, 2006.
- [47] K. E. Taylor, “Summarizing multiple aspects of model performance in a single diagram,” *Journal of Geophysical Research: Atmospheres*, vol. 106, no. D7, pp. 7183–7192, 2001.

## Research Article

# Spark Sensing: A Cloud Computing Framework to Unfold Processing Efficiencies for Large and Multiscale Remotely Sensed Data, with Examples on Landsat 8 and MODIS Data

Hai Lan <sup>1</sup>, Xinshi Zheng <sup>2</sup>, and Paul M. Torrens<sup>1,2</sup>

<sup>1</sup>Department of Computer Science and Engineering, Tandon School of Engineering, New York University, Brooklyn, NY 11201, USA

<sup>2</sup>Center for Urban Science + Progress, New York University, Brooklyn, NY 11201, USA

Correspondence should be addressed to Hai Lan; [hai.lan@nyu.edu](mailto:hai.lan@nyu.edu)

Received 26 April 2018; Accepted 8 July 2018; Published 23 August 2018

Academic Editor: Victor Mesev

Copyright © 2018 Hai Lan et al. This is an open access article distributed under the Creative Commons Attribution License, which permits unrestricted use, distribution, and reproduction in any medium, provided the original work is properly cited.

Inquiry using data from remote Earth-observing platforms often confronts a straightforward but particularly thorny problem: huge amounts of data, in ever-replenishing supplies, are available to support inquiry, but scientists' agility in converting data into actionable information often struggles to keep pace with rapidly incoming streams of data that amass in expanding archival silos. Abstraction of those data is a convenient response, and many studies informed purely by remotely sensed data are by necessity limited to a small study area with a relatively few scenes of imagery, or they rely on larger mosaics of images at low resolution. As a result, it is often challenging to thread explanations across scales from the local to the global, even though doing so is often critical to the science under pursuit. Here, a solution is proposed, by exploiting Apache Spark, to implement parallel, in-memory image processing with ability to rapidly classify large volumes of multiscale remotely sensed images and to perform necessary analysis to detect changes on the time series. It shows that processing on three different scales of Landsat 8 data (up to ~107.4 GB, five-scene, time series image sets) can be accomplished in 1018 seconds on local cloud environment. Applying the same framework with slight parameter adjustments, it processed same coverage MODIS data in 54 seconds on commercial cloud platform. Theoretically, the proposed scheme can handle all forms of remote sensing imagery commonly used in the Earth and environmental sciences, requiring only minor adjustments in parameterization of the computing jobs to adjust to the data. The authors suggest that the "Spark sensing" approach could provide the flexibility, extensibility, and accessibility necessary to keep inquiry in the Earth and environmental sciences at pace with developments in data provision.

## 1. Introduction

Data provided by remote sensing have long presented as a critical resource in monitoring, measuring, and explaining natural and physical phenomena. Indeed, remote sensing might justly be characterized as one of the first "big data" sciences [1]. Steadfastly, for the advances in the sensing capabilities of remote, Earth-observing platforms have continued to produce more and more data, with increasing observational breadth and finesse of detail. These developments carry a dual benefit and problem: analysis and inquiry in the environmental and Earth sciences not only are routinely awash with data but also often struggle to match pace in building empirical knowledge from those data

because the data are incoming with such haste and heft. Strategies to manage big remotely sensed data are required to fully exploit the benefits those data hold for applied scientific inquiry, and the topic of how computing might be leveraged to ease pathways between science and sensing holds significant currency across many fields, with particularly rapid adoption of high-performance computing [2] and cloud computing in the geographical sciences [3].

Remote sensing imagery is a commonly used source to support those studies of sustainable ecosystems, such as ecosystem dynamics, grassland degradation, and urban ecosystem restoration, especially in large areas [4]. Traditionally, studies with pure remotely sensed data involved only a few scenes of data in a limited study area, or they rely on

low-resolution remotely sensed images in large-area experiments [5]. Those traditions are changing as new data have dramatically altered the underlying substrate for analysis. For example, in the past few decades, the space-borne and air-borne Earth observation sensors are continually providing large-volume datasets. For example, Landsat 8, the latest Landsat mission launched in 2013, can collect more than 700 images per day, corresponding to approximately 86 terabytes of data per year [6], which is 14 times as much as that in the 1980s [4]. Processing the massive volume of remotely sensed data is now not the only problem: the intrinsic complexity of those data is also an important issue that must be considered.

The sensors that are actuated in remote sensing are usually designed to serve specific requirements of analysis for different fields of study. To fulfill those different needs, sensors are usually tasked to capture images at different resolutions. For example, high-resolution satellite sensors such as *WorldView-4* can produce imagery with a spatial resolution of 0.31 m in panchromatic vistas and 1.24 m spatial resolution in multispectral vistas [7], while the *QuickBird* platform can image the Earth with 0.61 m spatial resolution in panchromatic form and 2.44 m spatial resolution in multispectral form [8]. These resolutions, on the order of fractions of a meter to a few meters in spatial resolution, presented significant opportunities to monitor the Earth and represent the state of the art in Earth-observing imaging detail.

Concurrently, other remote sensing platforms are tasked with refreshing observations of the whole Earth's surface, aiming for coverage of large areas with temporal consistency, rather than small-area detail. For example, relatively medium-resolution sensors, such as *Landsat*, and relatively low-resolution sensors, such as *MODIS*, are deployed as long-term Earth observatories. *Landsat* provides 15 m panchromatic and 30 m multispectral imagery, which is very widely used in studies of large-area grassland degradation and urban land cover dynamics [9]. *MODIS* offers 250 m multispectral imagery and can build a mosaic view of the entire Earth once every few days. *MODIS* data has been widely adopted in global-scale research studies, particularly those trained on studying vegetation canopies for investigation of worldwide forest cover dynamics [10].

Many sensors support multispectral imaging. For example, *WorldView-4* data includes four spectral bands, and *Landsat 8 OLI/TIRS* provides 11 spectral bands. For some spectrally sensitive studies, higher spectral resolution imagery is required. In those studies, hyperspectral sensors (such as *Hyperion*, which generates 220 bands between 0.4–2.5  $\mu\text{m}$  [11]) can produce detailed spectral data over a very small wavelength range. Furthermore, different sensors offer different temporal resolutions in their rate of imaging as well as the timing of their coverage of subjects under their purview. For example, the *WorldView-4* satellite is capable of revisiting views every 4.5 days (sometimes sooner), while *Landsat* can deliver repeat views every 16 days [12]. Higher temporal resolution in return views facilitates the study of dynamics on the Earth surface, so that the time series and the time interval between visits become significant attributes of the observation, alongside the spatial resolution and spectral range. Therefore, methods to streamline a

feasible, effective, and efficient approach to processing archived and continually incoming multispatial, multispectral, and multitemporal remote sensing data are an ongoing requirement across many potential applications of remote sensing to applied scientific inquiry.

In this paper, possible scalable solutions are introduced to address issues of processing multiscale large-volume remote sensing datasets in multispatial, multispectral, and multitemporal cases. The aim is to implement a tool that can process different proposed remote-sensed tasks with only minor adjustments rather than fully rebuild new toolkits. Furthermore, this solution should be fully capable of exploiting benefits from cutting-edge cloud computing technologies, resources, and platforms to help researchers process and analyze large remotely sensed datasets that are difficult to process on local machines in an effective and efficient manner.

*1.1. Cloud Computing as a Resource for Big Data Processing.* Many researchers have made significant progress in advancing feasible, effective, and efficient processing for multiprong attributes of remotely sensed data, using developments in computer engineering. In particular, research into how graphical processing units (GPUs) and cluster-based high-performance computing (HPC) might be leveraged to advance image processing for remote sensing has been particularly fruitful [13]. More recently, cloud computing is increasingly being considered as a resource in processing remotely sensed imagery, largely because of cloud computing's native abilities to scale computing in kind as the data being processed also the scale. Furthermore, significant cloud computing resources are now available commercially, on a "pay as you go" model, from providers such as *Amazon Web Services (AWS)* [14], *Microsoft Azure* [15], and *Google's Compute Engine* [16]. These resources can be brought to bear on image processing tasks as IaaS (infrastructure as a service), PaaS (platform as a service), or SaaS (software as a service).

Cloud computing is useful in providing some of the flexibility required to match pace between incoming data, large existing data silos, and evolving analytical needs in image processing that authors alluded to in the introduction. Cloud computing affords this flexibility by allowing users to allocate and share software and hardware resources on the Internet in a distributed fashion, by splitting large computational tasks into many small parallel computing tasks, then assigning them to as many computing instances as are required to achieve computing goals based on data size, data fusion, resource use, or computing time. After all the distributed nodes of the cloud service have completed their assigned tasks, the results are bundled and returned to the users' local database. In this way, virtual instances, applications, and software are provided on an as-requested basis, and users may pay for those services as demanded. This affords a user access to a theoretically limitless size computing capacity (although very strong limits of available financial budgets to pay for the services quickly dock theoretical capacities to tangible practical realities in many real instances).

A promising community of computing frameworks has codeveloped alongside cloud computing hardware, and

several of these frameworks hold significant promise for processing remotely sensed imagery of the Earth's surface. For example, MapReduce was introduced by Dean and Ghemawat [17], ten years ago. In the decade since, a number of open-source implementations of the MapReduce model have emerged as promising frameworks for mediating the computing between image processing for remotely sensed data and cloud resources that are available to distribute and/or accelerate that computing on commercial (or user-run) clouds. Chief among these open-source implementations of MapReduce is *Apache Hadoop*. While Hadoop MapReduce relies on reading and writing data to a disk, another variant, Apache Spark [18] maintains data partitions in memory (a so-called in-memory computing framework). Spark also provides a network buffer for each reducing task, rather than merging outputs into a single partition, with the result that Spark can be one hundred times faster than Hadoop MapReduce on some big data tasks [19]. Nevertheless, one advantage that Hadoop might hold over Spark is that Hadoop allows parallel processing of large amounts of data that are bigger in physical storage size than the available memory. In fact, many remote sensing datasets are of a size that is so massive that they exceed the memory available in local machines or small clusters. Furthermore, physical disk resources are usually much less expensive in financial cost (of owning or accessing) than memory resources are. So, in cases for which limited memory may become a constraining factor, Hadoop presents as a better option in some cases for processing large amounts of remote sensing data.

However, cloud computing frameworks are agile relative to resource constraints. And that novel advances in cloud computing technologies and cloud platforms allow Spark to leverage resources from and across different cloud computing platforms, with the possibility that memory limitations may no longer loom as large a constraint for big remote sensing data processing scenarios. Consider memory as a resource that can be drawn upon on an as-needed basis, researchers can access theoretically unlimited memory on the cloud. Furthermore, Spark can run on a single workstation, as well as local computing clusters and cloud platforms. And Spark could access diverse data sources, such as *Amazon S3*, *Hadoop Distributed File System* (HDFS), *Cassandra*, and *HBase*. In other words, Spark not only can access local private data warehouses but also can reach cloud-stored big remote sensing datasets and do so via the cloud platform directly, with the ability to process those data on the cloud and then stream back the required results.

### 1.2. Cloud Computing for Processing Remotely Sensed Images.

One of the common computing solutions to the burden of processing, analyzing, and managing large-scale remote sensing data is to parallelize the remote sensing processing tasks: to spread the burden over multiple computing units to reduce the overall processing time [6]. For example, Huang and her colleagues used the message passing interface (MPI) as a computing framework for their work on dust storm simulation and forecasting on the *Amazon EC2* commercial cloud service [13]. They deployed MPI on the Amazon cloud and applied loosely coupled nested models

to process a high-resolution dust storm dataset. Their performance tests showed efficient and economical results. Cavallaro et al. [20] used GPUs to implement a support vector machine (SVM) classifier with MPI and *openMPI* frameworks. As an alternative to using HPC computing frameworks, other researchers have developed their own bespoke parallel large-scale remote sensing data processing platforms. For example, Wang et al. [21] developed *pipsCloud*, which is a cloud-based HPC approach to process remote sensing on-demand and in real time. To further enhance performance, Wang et al. [21] used Hilbert  $R^+$ -tree indexing.

The turn toward development of tools by remote sensing scientists, for remote sensing scientists, leveraging computing techniques but departing in ways that are special to remote sensing applications, is a wonderful development for remote sensing science. Nevertheless, bespoke solutions (particularly in academic settings) cannot feasibly contribute to the massive levels of computing available now commercially, with the result that absolute performance will always lag behind that which might otherwise be available on the marketplace. Also, applying MPI or self-developed systems often requires significant research and development effort into programming, debugging, and tuning the computing system and environment, and one might perhaps make an argument that the time devoted to these tasks could be used on the applied science instead. In some cases, building these systems on a bespoke basis is very challenging. For example, consider MPI, programming tasks designed for serial computing and converting them to parallel form can be significantly burdensome and particularly so for some complex image processing algorithms. Moreover, the networking security, near ubiquitous availability, and fast-moving hardware compatibility (e.g., in shared memory clusters) of commercial platforms offer significant practical advantages. Some existing work points to the potential advantages that are obtainable in cloud processing of big geospatial data. For example, Chen and Zhou [22] demonstrated that Apache Hadoop can be leveraged for partitioning using a mean shift algorithm. With a local mode test, they successfully increased the processing speed by  $\sim 2$  times [22]. Also, Giachetta [23] introduced a Hadoop-based geospatial data management and processing toolkit, *AEGIS*, which he compared against many existing MapReduce-based frameworks, such as *SpatialHadoop*, *Hadoop-GIS*, *HIPI*, and *MrGeo* with spatial join, query, and aggregation operations [23].

Compared to MapReduce-based approaches, solutions based on Apache Spark can usually generate results at higher efficiency, as mentioned in "Introduction." For example, Sun et al. [24] used *MLlib* in Spark to test the multi-iteration singular value decomposition (SVD) algorithm on high-resolution hyperspectral remote sensing images. Compared with the *Apache Mahout* (MapReduce) approach, they found that the Spark approach can essentially trounce MapReduce in their tests, once Spark is able to access enough hardware resources. Another study using Spark to process massive remote sensing data, by Huang and his colleagues [25], demonstrated a series of comprehensive performance tests, using Spark to implement different types of algorithms

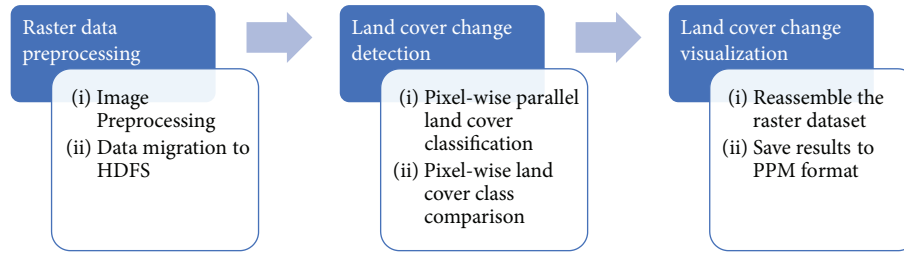


FIGURE 1: Spark-based remote sensing image processing workflow.

in remote sensing. Huang et al. [25] discussed the performance of each of the tests on different running environments, including local, standalone, and *yet another resource negotiator* (YARN). They also proposed a self-defined, strip-based partitioning approach to replace the default hash partitioning method [25].

## 2. Methodology and Data Sources

In this paper, authors propose to extend upon recent developments in cloud computing as a resource for processing remotely sensed imagery. Specifically, a Spark-based large-scale remote sensing image processing tool that can be deployed on cloud platforms will be introduced. In the following sections, authors will discuss how to design experiments by applying two commonly used classifiers—normalized difference vegetation index (NDVI) and normalized difference water index (NDWI)—as a testbed to assess the feasibility and performance of our tool. A scheme for designing a change detection scheme based on classification results generated by the proposed tool on a time series will be also introduced. One of the key advantages of this approach is in its ability to easily and straightforwardly support users' access to processed land cover changes within a large set of spatial-temporal images. Moreover, the paper will demonstrate a visualization approach to save text-based output from the analysis in common picture format, allowing users to examine results easily and quickly.

**2.1. Methodology.** The approach presented in this paper is based on the YARN cloud environment. The goal, in using YARN, is to facilitate the availability of the processing environment in ways that are widely applicable to real-world scenarios. YARN has been widely used in many current cloud environments [26]. Unlike traditional versions of Hadoop MapReduce, YARN allows for allocation of system resources as containers to the various applications. In other words, different computing frameworks can be deployed on a single physical cluster in a noninterfering manner. In YARN mode, a Spark framework is composed of a master instance and many workers. The master instance is responsible for negotiating with the YARN *Resource Manager* to request enough computing resources, as needed, by analyzing the Spark applications submitted by clients. Once the master instance is loaded, it will schedule the tasks to executors with allocated containers. Until all tasks have been finished, Resource Manager will revoke all allocated resources for further possible tasks.

Resilient distributed datasets (RDD) form the basic abstraction of a dataset in Spark. RDDs can be created from an external dataset, or from existing RDDs. For cases in this research, RDDs will be created from the original remote sensing images stored in HDFS. For each image, three RDDs will be created for green, red, and near-infrared bands for NDVI and NDWI land cover classification at the initial stage. RDDs contain the data partitions and the metadata records. According to the Spark mechanism, RDDs will go through a series of transformations and action operations to process the data partitions in a distributive manner. The transformation operations of RDDs will be executed on individual partitions of an RDD and those operations will return a new RDD. Action operations will summarize information from an RDD by user-defined functions and return a result. For example, the joining operation, as a commonly used transformation operation in Spark, involves joining partitions belonging to two RDDs and creating a new one. In this case, the data blocks will not be moved at the current stage because of the lazy mechanism. However, action operations, such as count, will process the data partitions in RDD and perform real computing.

Based on the features of Spark, a workflow has been designed as illustrated in Figure 1. The first step in that workflow is to extract each band of a raster dataset by using the *Geospatial Data Abstraction Library* (GDAL), which is an open-source translator library for raster and vector geospatial data formats [27]. Each line of the extracted data contains the geographical coordinates and the digital number (DN) value of the raster cell in the original raster dataset. These files are then put into the HDFS as data input sources for distributive processing.

The second step is to perform parallel processing of image classification and land cover change detection. As introduced before, for each image that must be processed by this tool, three RDDs will be created for its green, red, and near-infrared bands. The basic units of the RDD are key-value pairs. In this case, the geographical coordinates are set as the key, and the DN value of a raster cell will be the value. In this manner, parallel land cover classifications can be conducted across many computer units in a cluster. The extent of parallel processing depends on the Spark application configuration and the cluster hardware specifications. Because the basic parallel processing unit is pixel-wise, this method can be highly flexible and scalable, allowing raster datasets to be partitioned in any manner, regardless of the spatial structures of the raster. However, partitioning

```

1: Input= TIF1, TIF2, ..., TIFk; Dimension = X*Y
2: For k = 1 to K-1 do:
3:   InputTIF1 = TIFk
4:   InputTIF2 = TIFk+1
5:   For m = 1 to 2 do:
6:     For x in 1 to X
7:       For y in 1 to Y:
8:         ndvixy = (InputTIFxy.NIR - InputTIFxy.R)/(InputTIFxy.NIR + InputTIFxy.R)
9:         ndwixy = (InputTIFxy.G - InputTIFxy.NIR)/(InputTIFxy.G + InputTIFxy.NIR)
10:        landcoverxy = CLASSIFIED(ndvixy, ndwixy)
11:        landcoverm[x, y] = landcoverxy
12:      endFor
13:    endFor
14:  endFor
15:  landcover_changek = CHANGE(landcover1, landcover2)
16:  Output = landcover_coverk
17: endFor

```

ALGORITHM 1: NDVI/NDWI classification and changing detection.

strategies still must be seriously considered, because an appropriate partitioning strategy will help to optimize the performance with better usage of the computing resources of the cluster. Spark supports hash partitioning and range partitioning by default; these applications are appropriate for many cases in the real world. However, according to the results of the study of Huang et al. [25], the partition scale cannot be too small or too large. A very small partition scale will result in low-performance computing and even increase the fault recovery cost. A very large partition scale may lead to the out-of-memory error. Inspired by their strip-based partitioning method, splitting data into chunks with a configured HDFS block size is needed in following experiments.

In Algorithm 1, the detailed algorithm of using NDVI and NDWI as classifiers on remote sensing images has been illustrated. Several transformation operations are performed on each partition in RDDs. For  $k$  input *GeoTiff* remote sensing images, the algorithm will first parse the dimension of them. Moreover, those created RDDs will be marked by a time sequence in the time series. For each data chunk, in each pair of image RDDs (e.g., a pair of images in 2013 and images in 2014), the NDVI and NDWI classifier will be applied to each pixel to calculate the indicated values. The NDVI [28] can be calculated according to its definition as

$$\text{NDVI} = \frac{\text{NIR} - \text{red}}{\text{NIR} + \text{red}}. \quad (1)$$

The range of NDVI is from negative one to one, which can use different ranges to denote sparse vegetation, dense vegetation, barren rock and sand, and water. However, NDVI may not always correctly distinguish the water body, especially when there is a noisy signal in the water area (e.g., mud). To further improve the accuracy of

classification, NDWI is applied according to McFeeters [29] as follows:

$$\text{NDWI} = \frac{\text{green} - \text{NIR}}{\text{green} + \text{NIR}}. \quad (2)$$

NDWI can distinguish the water feature with the positive value indicator. From the perspective of algorithm implementation, RDDs of three bands will be joined as a single RDD for NDVI and NDWI calculation of each raster cell with mapping operations. Land cover classification can, therefore, be conducted in parallel by using calculated NDVI and NDWI results. Once the land cover features are classified by NDVI and NDWI indicators, each feature can be labelled with a class ID and pass those IDs when changing the detection function. The changing detection function will compare the feature IDs from each image pair and summarize how those land features change from the former year to the current year.

The final step is to visualize land cover change, as illustrated in pseudo code in Algorithm 2. With all  $k$  numbers of land cover change results generated by Algorithm 1 for each image pair, visualization images are created in PPM format from the obtained output RDD, which is a lowest common denominator color image file format [30]. Although redundant, PPM is an easy format to write and manage text-based outputs into human-readable figures. The two RDDs of land cover classifications for two images from Algorithm 1 will be joined as a single RDD, and the values of key-value pairs will be converted to colors according to a user-defined RGB color scheme. This joined RDD will then be sorted to the original order and reduced in a manner such that each key-value pair represents a row of the original raster image. Finally, to produce a PPM-format image, this RDD is appended to the PPM file header to create a complete PPM image.

```

1: Input = landcover_change1, landcover_change2, ..., landcover_changeK; Dimension = X*Y
2: For k = 1 to K do:
3:   InputKVk = landcover_changek
4:   rgbKVk = RGB(inputKVk)
5:   Sort rgbKVk by two dimensions
6:   rgbVk = values of rgbKVk
7:   Reshape rgbVk to dimensions X*Y
8:   Output = rgbVk
9:   Save rgbVk to files
10: endFor

```

ALGORITHM 2: Visualization.

An overview of how the whole process works is illustrated in Figure 2. Four steps are applied in this design: (1) read and parse each pair of input images and create RDDs for green, red, and near-infrared bands; (2) split data into chunks and process them in parallel; (3) gather results and assign labels to each pixel; and (4) reconstruct whole images by sorting output RDDs and visualize them in PPM format.

**2.2. Data Sources.** To prove the applied utility of the proposed scheme, three experiments are performed, and two different remote-sensed imagery datasets are involved. The first experiment is using the Landsat 8 operational land imager (OLI) dataset in three different scales to test the workflow of classification and change detection and visualization algorithm with Spark on local cloud environment. To further study the tuning performance of this scheme, the second experiment is designed to run this tool under different execution configurations with the same Landsat 8 dataset. The last experiment is set to prove this tool can consume different source remote-sensed imagery datasets with only minor parameter adjustments. By using the same algorithm presented above, a MODIS dataset on Amazon EC2 which is a real commercial cloud platform is processed.

Landsat 8 scans the entire planet surface in a 16-day period [31]. Equipped with the latest OLI sensor, Landsat 8 provides unprecedented spectral information with two additional spectral bands in the whole Landsat instrument family. In addition to offering a 15 m panchromatic band and a 30 m multispectral band, as in many previous products, Landsat 8 also includes a quality assessment (QA) band to support pixel-based cloud, shadow, and terrain occlusion filtering. A relatively short revisit period, medium spatial resolution, and seven spectral bands make Landsat 8 OLI products a commonly used freely accessible remote sensing imagery datasets for science that relies upon spatial, spectral, and temporal Earth attributes for environmental research. Furthermore, the Landsat 8 dataset is currently open to the public on cloud platforms, such as Amazon S3 [32] and *Google Earth Engine* (GEE), making it a great data source to serve cloud-based large-scale remote sensing processing in the cloud.

Like Landsat 8 OLI, MODIS satellite datasets are landed on as Amazon S3 [33] and GEE since 2017. MODIS

provides a variety of planet observation products with daily temporal resolution. In this paper, MODIS/Terra Surface Reflectance Daily L2G Global 1 km and 500 m SIN Grid V006 (MOD09GA) will be used as second data input, which can provide 7 band surface spectral reflectance with 500-meter spatial resolution. Besides, a bunch of 1-kilometer resolution observation and geolocation statistic bands are offered in this product.

The coverage of each of the datasets that are used is illustrated in Figure 3. Three scales of Landsat 8 imagery datasets of small, medium, and large scale were used in experiments, as the input data source. This multiscale approach allowed us to assess whether our tool can perform multiscale remote sensing image processing with only minor parameter adjustments, to assess whether a wide array of remote sensing imagery datasets can be processed by our proposed framework in real scenarios. Because of remote sensing images, which are collected by different sensors at different spatial resolutions, with various bands of spectral information, and at diverse temporal scales are essentially formed by pixels, pixel-based algorithms implemented via Spark in the cloud should be capable of performing a very wide array of pixel-based processing and analysis. However, to further prove the presented tool can handle multisource remote sensing images in real cases, a MODIS dataset that fits for the exact same coverage of large-size Landsat 8 dataset is imported.

To generate a time series for change detection, one image per year has been chosen from a dataset spanning 2013 to 2017. The small-size images and medium-size images are approximately in one single scene of a Landsat image. Hence, those images that were acquired on a similar date for each year are preferably selected to reduce the land cover changes caused by seasonal variation factors. However, a large dataset is formed by over 15 scenes of original images. In this case, it cannot guarantee that each tile of this dataset can be filled by same-date images for each year. Hence, by broadening the filter criteria to the month level, obtaining enough tiles can be ensured to form the whole area. Another important factor is that the chosen images are preferably high quality to reduce the cloud and haze problems. For MODIS dataset, with relatively coarse spatial resolution and large coverage per scene, it takes about half of single scene to fit the large-size Landsat dataset coverage. Also, the acquisition time of it follows the date of the small- and medium-size

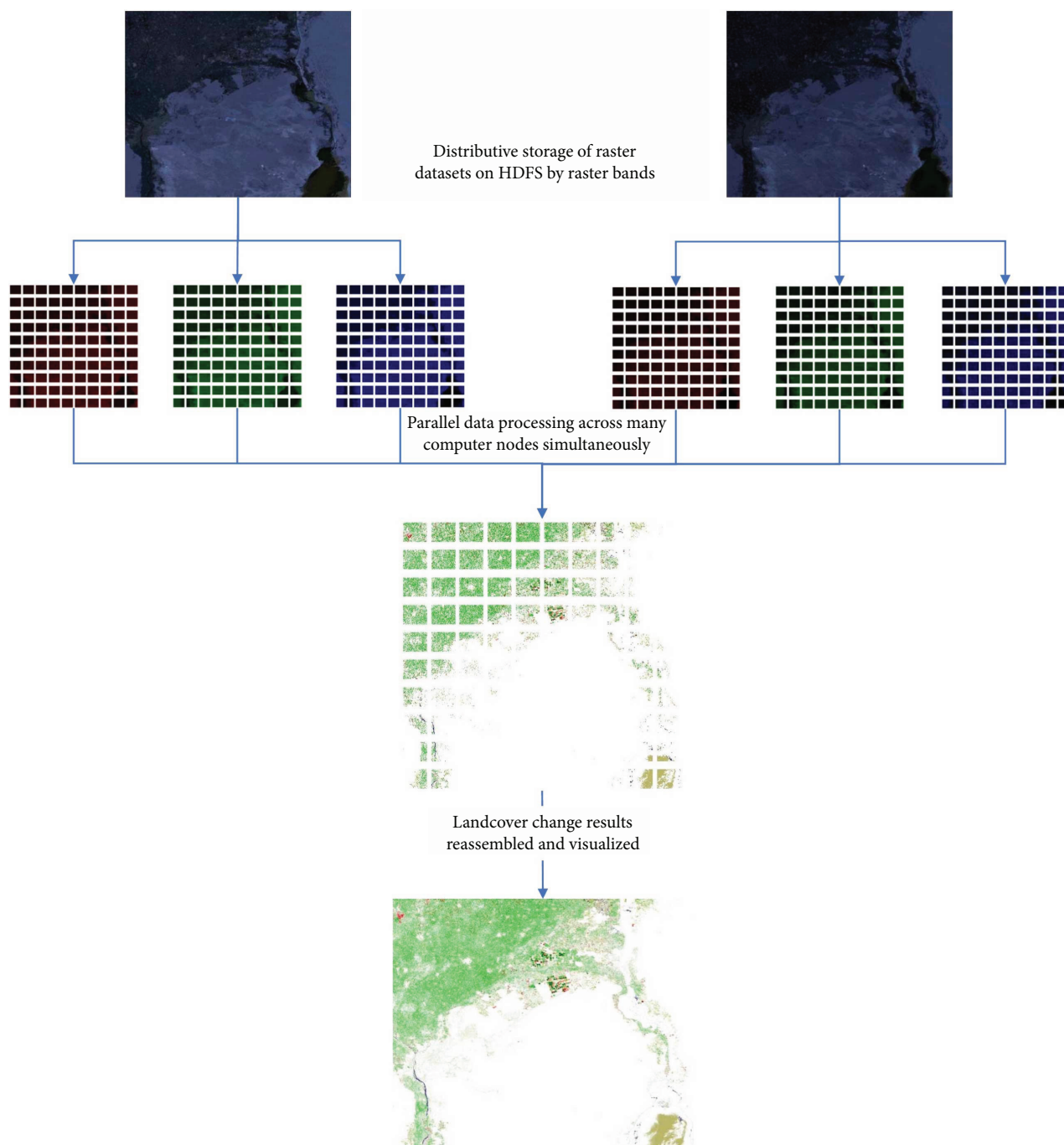


FIGURE 2: Detailed workflow for image classification and changing detection.

Landsat dataset because MODIS can provide daily products. The detailed acquisition time of each dataset is listed in Table 1.

The reason for the choice of the study area shown in Figure 3 is that, in the Suez Canal area, the land cover mainly includes sparse and dense vegetation, a natural water body, the Suez Canal (with water), and bare sands and rocks. Thus, the study area is a great test area for our NDVI/NDWI classifier to detect detailed land cover and generate relatively accurate change detection results. Another reason for the choice of the study area is that Suez Canal was expanded

since 2013 to build another branch [34]. This project can be clearly monitored by the presented change detection process.

In those experiments, all remote sensing image datasets were exported from GEE, which is a cloud-based platform that can serve remote sensing data source with customized criteria [35], for example, setting (1) the region boundaries to acquire data belonging to our study area and (2) the cloud mask to filter the cloud pixels on images before exporting the data to our cloud drive. Landsat 8 and MODIS (MOD09GA) both provide surface reflectance produced on GEE. If other datasets are used, a strictly image-based atmospheric

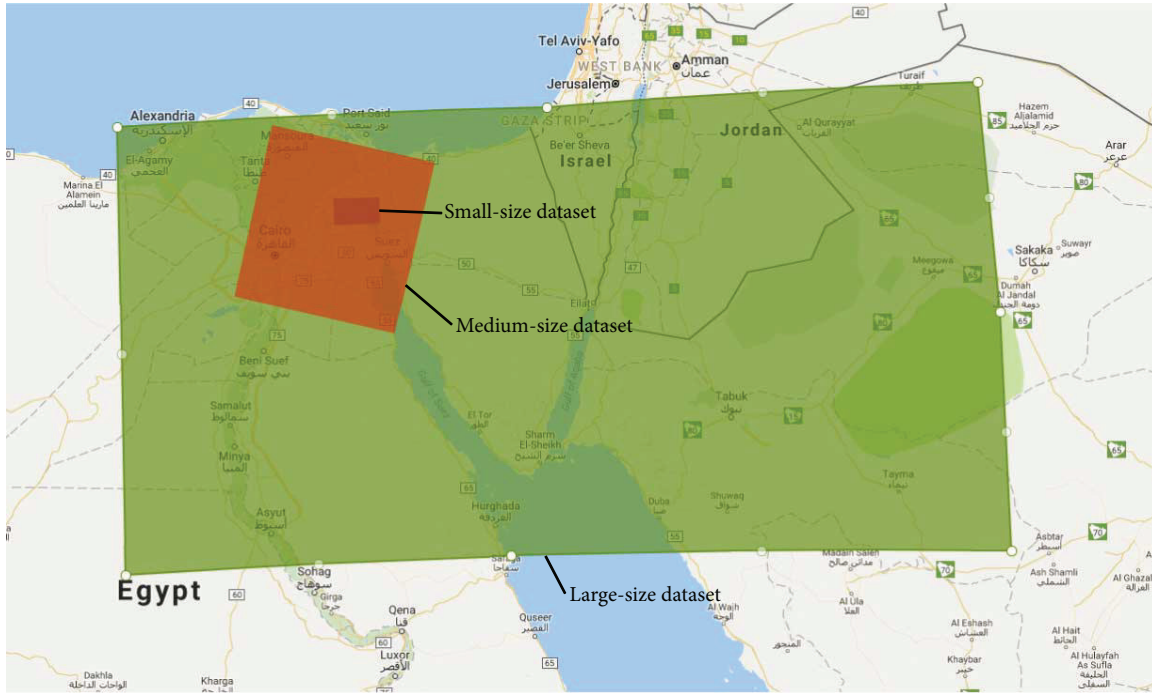


FIGURE 3: Landsat 8 image dataset in three different scales.

TABLE 1: Detailed acquisition time of each dataset.

	2013	2014	2015	2016	2017
Landsat_small	4/29	3/31	4/19	3/4	4/5
Landsat_medium	4/29	3/31	4/19	3/4	4/5
Landsat_large	Apr	Mar	Apr	Apr	Apr
MODIS	4/29	3/31	4/19	3/4	4/5

TABLE 2: Landsat data size and processing time.

	Scenes for each year	Size	Processing time
Small	~0.15	~1.2 G	67 s
Medium	~1	~10 G	276 s
Large	~15	~107.4 G	1018 s

correction should be followed to remove the haze impact on those images [36].

**2.3. Experiment Environment.** Two experiment environments are involved in this research for local cloud environment test and real commercial cloud platform test, respectively. The local computing cluster contains a total of 20 nodes. Two of them are master nodes, which equipped with 2 Intel Xeon E5-2680v4 2.4 GHz CPUs and 256 G memory each. 18 computing nodes are equipped with 2 Intel Xeon E5-2690v4 2.6 GHz CPUs (28 cores) and 256 G memory each. 10 Gbit network is assigned. In total, there are 1008 computing vcores and 5.12 Tb memory available. 2 Pb HDFS is configured and the block size is 128 M as default. Linux (Centos 6.9) is running on this cluster. Java 1.8.0\_152 64-Bit Server VM is installed. Spark version is 2.2.0 with Cloudera release 1 and CDH 5.12.0.

The Amazon EC2-based computing cluster is another computing environment. Based on the computing needs of the third experiment in this paper, a 3-node cluster is built with 1 t2.xlarge instance with 4 vCPU Intel Broadwell E5-2686v4 2.3 GHz as master nodes and 2 t2.large instances with 2 vCPU Intel Broadwell E5-2686v4 2.3 GHz as slaves.

All nodes are involved in computing. The total number of vcores is 8 and the overall memory is 32 G. 20 G storage per node is attached with default 128 M block size. The default HDFS replica is set as 3. Ubuntu Server 14.04 LTS (HVM) is the operation system. Similar to local computing cluster, Java 1.8.0\_152 64-Bit Server VM, Spark 2.2.0 with Cloudera release 1, and CDH 5.12.0 are configured.

In the following parts of this paper, how authors applied the aforementioned workflow on real multiscale and different source remote sensing datasets to test the performance and feasibility of the Spark-sensing scheme will be discussed. The performance of the tool and the visualization of the experimental results will also be shown. Moreover, the flexibility, extensibility, and accessibility gleaned by using a Spark-based solution in remote sensing image dataset processing will be further discussed.

### 3. Results and Discussion

The first experiment is performed on a 20-node YARN computing cluster. In this experiment, a multiscale remote sensing image dataset with the Spark-based classification and change detection algorithm has been successfully processed.

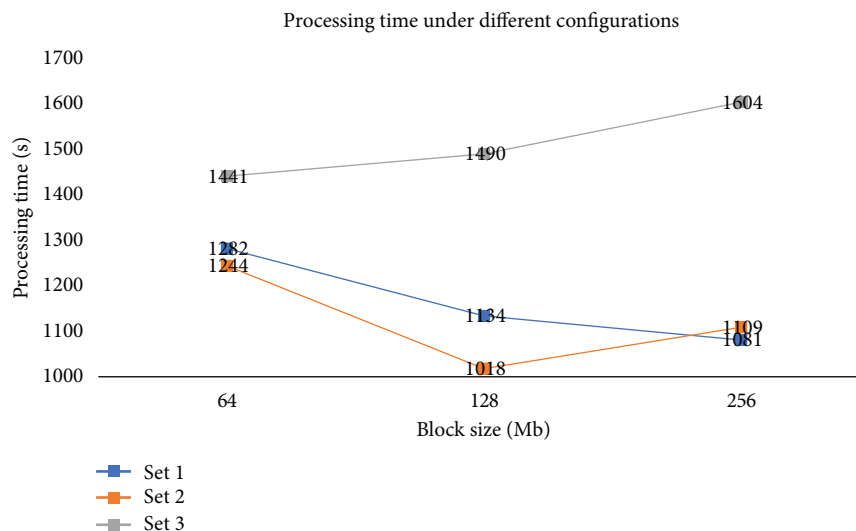


FIGURE 4: Processing time of large-size Landsat dataset under different configurations.

The detailed data size and processing time are shown in Table 2. The processing time is recorded under configurations with default block size, 50 executors with 20 cores each, and 20 G executor memory. Note that Spark can offer highly efficient processing for remote sensing images. Especially for a relatively large cluster, a sufficient computing resource can support the entire distributed computing process, ensuring that the processing time does not significantly increase as the data size increases. From the perspective of algorithm design, by anatomizing the overall processing time in each operation time-consuming segment, the joining operations are found to be very time-consuming, especially for a dataset with large pixels. In contrast, mapping operations for classification and change detection are much faster in comparison to joining operations. Hence, designing an image processing algorithm with fewer join operations and appropriate partitioning to reduce the data block moving may enhance the performance. Besides, repartitioning operations should also be avoided because it will result in a very time-consuming shuffle process.

Except enhancing the overall performance from algorithm design, the second experiment is developed to further study if the execution configurations may effect on the processing performance. Only the large-size Landsat 8 dataset is applied in this experiment to assess the processing time with different configurations. According to Spark performance tuning official documents [37], the executor numbers, executor, cores and executor memory are three main factors that may effect on performance of Spark-based applications. Budgeting available computing resources in advance is usually needed for users to gain satisfying processing performance. Here, three different configuration sets are assigned as follows: (1) 10 executors with 100 G memory and 100 cores each as set 1, (2) 50 executors with 20 G memory and 20 cores each as set 2, and (3) 500 executors with 2 G memory and 2 cores as set 3. Those three configuration sets are designed with the same total computing vcores and memory. It is also worth to point out that block size

may sometimes effect on performance as well. As discussed above, repartition operations (especially for increase partitions) usually should be avoided to eliminate unnecessary shuffle process. Under this circumstance, partitions will be mainly decided by block size during I/O process when RDDs are created. If the block size were too small, massive number of partitions will be created especially with very large input dataset, which will lead to increasing the overhead of task management, though coalesce operation may be applied to decrease the partitions sometimes without shuffling in some cases. If the block size were too large, only a few partitions will be created so that not all the cores in the available computing resource can be sufficiently utilized. In other words, the feature of parallelism is not fully exploited to enhance the performance. Here, three different block sizes are set during the experiments. In Figure 4, the performance of processing the dataset under different execution configurations and different block sizes is represented. The shortest run is offered by 50 executors with 20 G memory and 20 cores each under default block size. With the same executor configuration set, the performance shows a bit lower with 64 M block size, which may result from the total task number which is increased with a smaller block size. However, the execution time for each task is not significantly reduced with corresponding settings. The performance of the same configuration set with 256 M block size is also beaten by it with a default block size. The reason is the partitions generated under this block size are too few so that parts of the executors are not active during processing. This problem shows more obviously when applying configuration set 3, because the number of executors is far more than the tasks under this case and too many computing resources are in idle, which leads to the lower performance. The execution configuration set 1 shows very similar performance with set 2 under each block size setting. However, by monitoring the core utilization of set 1, it is lower than it is with set 2. This may present that the increasing number of executors and decreasing the cores per executor may lift the utilization of cores and may

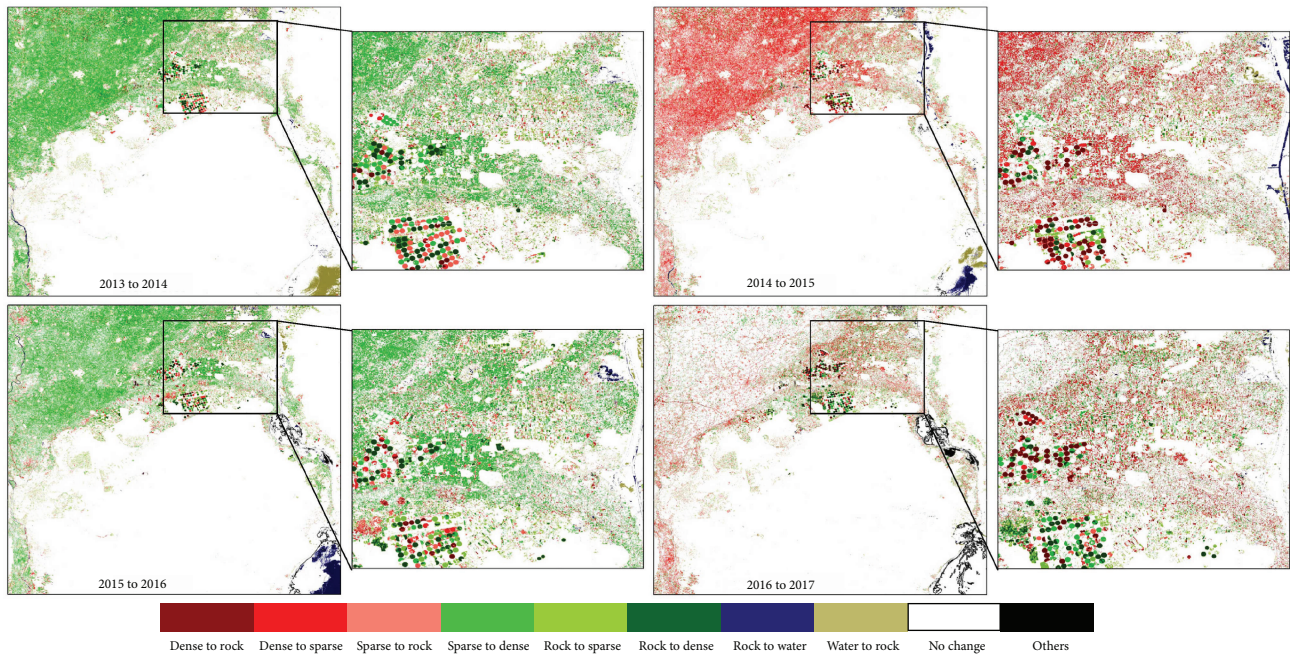


FIGURE 5: Changing detection visualization results of 2013 to 2014, 2014 to 2015, 2015 to 2016, and 2016 to 2017.

also help enhance the overall performance in some cases especially for very large dataset with relatively limited computing resources.

Here, the land cover feature is defined in four classes: dense vegetation, sparse vegetation, rock/sand, and water. In the legend of Figure 5, colors are set for the changes of each pixel in the study area from one feature to another. For example, “rock to water” indicates that the land cover feature was observed to have changed from sand or rock to water body in the past year. Conditions of no change indicate there are no detected changes in the past year. Others indicate those parts in the images with no data or with erroneous data. In Figure 5, the changes for each pair of images can be clearly seen. Moreover, users can generate a “final” result directly from 2013 to 2017 with a single parameter change. Taking the changing map of 2014 to 2015 in Figure 5 as an example, users can monitor the new branch of the Suez Canal being built and filled with water. It also shows that some new vegetation is growing along the Canal; such vegetation may be a new farmland because most of the vegetation regions are in artificial-like shapes.

As discussed before, the presented tool can be deployed on commercial cloud platform with no change (if the hardware configuration is highly different, strategies of balancing workload may need to be reconsidered). The third experiment is designed to use the proposed framework on Amazon EC2 to process MODIS dataset. Different from Landsat 8 products with band 4 as red, band 5 as NIR and band 3 as green, MODIS (MOD09GA) product sets red band as band 1, NIR as band 2, and green as band 4. Except changing the band index for input, the processing tool is ready to launch with no additional adjustment needed in coding. This experiment run on the 3-node Amazon EC2 cloud computing cluster. By applying 2 executors with 2 cores and 4 G memory

each, the experiment is successfully completed in 54 seconds. It is worth to point out that 54-second processing time is not fast with such a small input dataset and that  $\sim 0.5$  scene MODIS image is only about 50 M. Because in this case, lots of time are occupied by job submission, task management, resource allocation, and so on, the performance of Spark applications can only show significantly with relatively large dataset. However, this experiment still proves the idea that the proposed framework can be deployed on real commercial platforms to process multisource remote sensing images with only minor parameter adjustments.

Those experiments represent a robust solution for constructing remote sensing image processing tools for multiple purposes that are flexible (the ability of the tool to fit multisource datasets in different scales), extensible (the ability of the tool to grow in size and accommodate the volume of computing to resolve), and accessible (the ability of the tool to access data from multiple storage platforms and locations on local resources, data centers, and the cloud). All tested image datasets in those experiments are Landsat 8 with 30-meter spatial resolution and MODIS with 500-meter spatial resolution. However, the reader should note that the input dataset can be any raster-based images in different spatial, temporal, and spectral resolutions, because the algorithm implemented in our experiment is a pixel-based processing algorithm. Following a similar mechanism, all pixel-based algorithms can be implemented by processing the DN values of each pixel to generate required results under this framework. Hence, regardless of applying it to an existing large amount of data or filling it with a next-horizon dataset that will be collected in the future with current sensors or new sensors, this solution is capable of handling the tasks with only minor change in coding, thereby saving the high cost usually invoked in reprogramming different tools for different research goals.

With the Spark-based implementation, as demonstrated in the experiment, the main structures of this tool do not require modification as the volume of dataset changes. For example, it is becoming possible that, even if a Landsat 8 dataset covering a whole year (47.33 Tb) [6] is involved in processing at the same time, by the support of cloud platforms, users can always gain sufficient computing resources (memory especially, for Spark) in theory. Consider that Amazon EC2 now provides the “x1e.32xlarge” instance, which contains 128 virtual CPUs, ~4 Tb memory, and ~4 Tb storage. Users can apply fewer than 20 instances to implement in-memory computing with Spark-based approaches for this dataset in many different processing purposes. Nevertheless, to maintain the high performance of the tool, the partitioning strategies should be tailored based on real execution environments, especially for clusters with unevenly distributed computing resources and networking performance.

As discussed in the introduction, Spark-based approaches can easily access HDFS, Amazon S3, Cassandra, and HBase. Benefitting from cloud storage and management development, an increasing amount of data has been stored in the cloud and is open to the public. The approach as demonstrated provides cloud-based data resources to support users in performing a “pure” cloud analysis and in creating new products from it, without transferring unnecessary original and intermediate data to local storage before the final results are generated. This solution can also support data from multiple sources at the same time. For example, users can access cloud-stored public data as part of their data source and can also access and load their private data stored on local HDFS in a single Spark application.

#### 4. Conclusions

In this paper, authors argue that the current state of the art for big data remote sensing, involving massive datasets being generated from existing and next-generation satellites and observation platforms, is, in many cases, proceeding at paces that outstrip our analytical capabilities to keep up with information products atop those data. While data and analysis are out of alignment, researchers perhaps miss opportunities to build the necessary science that might otherwise be attainable if data and analysis could be better connected. In this paper, authors discussed the current widely used approaches that have been developed by existing studies as a means to cater to the call of the community for the development of an effective and efficient large-scale processing framework to process large-volume remote sensing datasets. Based on the reviews of a comparison with other possible approaches, using Spark to build a robust scalable tool on a cloud environment is possibly an important and practical option to match data with analysis at pace. To this end, a Spark-based multiscale large remote sensing classification and change detection tool has been introduced, and its successful deployment and experimental testing in a cloud environment have been shown.

The approach in this paper suggests several promising advantages. First, the scheme for Spark-sensing offers

considerable flexibility for processing big remote sensing datasets in multispatial, multispectral, and multitemporal cases. Indeed, shifting between resolutions and spectrums is possible with slight adjustment, thereby significantly saving the time cost of reprogramming brand new toolkits for different purposes. Second, this scheme makes it possible to exploit the benefits of cloud platforms to gain (theoretically) unlimited computing resources, with highly efficient performance. Third, the presented approach is natively highly accessible to multisource data storage, even in the cloud, which is useful in reducing data transformation costs.

The tool discussed in this paper is obviously just a prototypical framework. Thus, significant improvements could be made. The work here serves to prove the general principle and mechanisms necessary to get going with experiments in this area, and hopefully it can encourage others in the community to build on this foundation. An obvious extension of our approach could include the implementation of more complex remote sensing image processing algorithms, especially in classification, to better match the real cases in different research areas. Another improvement could be explored in designing better partitioning strategies to further enhance the computing performance. Moreover, using a dataset from the cloud directly may reduce the unnecessary data transferring from the data source to the cloud environment, which may better fit the usage habits in real-world problem solving.

#### Data Availability

The Landsat 8 surface reflectance data used to support the findings of this study have been deposited in the Google Earth Engine repository ([https://explorer.earthengine.google.com/#detail/LANDSAT%2FLC08%2FC01%2FT1\\_SR](https://explorer.earthengine.google.com/#detail/LANDSAT%2FLC08%2FC01%2FT1_SR)). The MODIS/Terra Surface Reflectance data used to support the findings of this study have been deposited in the Google Earth Engine repository (<https://explorer.earthengine.google.com/#detail/MODIS%2F006%2FMOD09GA>).

#### Conflicts of Interest

The authors declare that they have no conflicts of interest.

#### Acknowledgments

The authors are grateful to Professor Huy T. Vo in the Department of Computer Science and Engineering at New York University for his advice in building the partitioning components of the work.

#### References

- [1] M. F. Goodchild, H. Guo, A. Annoni et al., “Next-generation digital earth,” *Proceedings of the National Academy of Sciences*, vol. 109, no. 28, pp. 11088–11094, 2012.
- [2] C. Yang, M. Yu, F. Hu, Y. Jiang, and Y. Li, “Utilizing cloud computing to address big geospatial data challenges,” *Computers, Environment and Urban Systems*, vol. 61, pp. 120–128, 2017.

- [3] C. A. Lee, S. D. Gasster, A. Plaza, C. I. Chang, and B. Huang, "Recent developments in high performance computing for remote sensing: a review," *IEEE Journal of Selected Topics in Applied Earth Observations and Remote Sensing*, vol. 4, no. 3, pp. 508–527, 2011.
- [4] M. A. Wulder and N. C. Coops, "Make earth observations open access: freely available satellite imagery will improve science and environmental-monitoring products," *Nature*, vol. 513, no. 7516, p. 30, 2014.
- [5] Z. Wang, J. Zhong, H. Lan, Z. Wang, and Z. Sha, "Association analysis between spatiotemporal variation of net primary productivity and its driving factors in Inner Mongolia, China during 1994–2013," *Ecological Indicators*, 2017.
- [6] Y. Ma, H. Wu, L. Wang et al., "Remote sensing big data computing: challenges and opportunities," *Future Generation Computer Systems*, vol. 51, pp. 47–60, 2015.
- [7] Satellite Imaging Corporation, "WorldView-4 satellite image gallery," March 2018, <https://www.satimagingcorp.com/gallery/worldview-4/>.
- [8] Satellite Imaging Corporation, "Quick Bird satellite sensor," March 2017, <https://www.satimagingcorp.com/satellite-sensors/quickbird/>.
- [9] H. Lan and Y. Xie, "A semi-ellipsoid-model based fuzzy classifier to map grassland in Inner Mongolia, China," *ISPRS Journal of Photogrammetry and Remote Sensing*, vol. 85, pp. 21–31, 2013.
- [10] M. A. Friedl, D. K. McIver, J. C. F. Hodges et al., "Global land cover mapping from MODIS: algorithms and early results," *Remote Sensing of Environment*, vol. 83, no. 1–2, pp. 287–302, 2002.
- [11] US Geological Survey, "Sensors-Hyperion," March 2018, <https://eo1.usgs.gov/sensors/hyperion>.
- [12] W. Turner, S. Spector, N. Gardiner, M. Fladeland, E. Sterling, and M. Steininger, "Remote sensing for biodiversity science and conservation," *Trends in Ecology & Evolution*, vol. 18, no. 6, pp. 306–314, 2003.
- [13] Q. Huang, C. Yang, K. Benedict, S. Chen, A. Rezgui, and J. Xie, "Utilize cloud computing to support dust storm forecasting," *International Journal of Digital Earth*, vol. 6, no. 4, pp. 338–355, 2013.
- [14] E. Amazon, "Amazon web services," 2015, November 2012, <http://aws.amazon.com/es/ec2/>.
- [15] B. Wilder, *Cloud Architecture Patterns: Using Microsoft Azure*, O'Reilly Media, Inc., 2012.
- [16] D. Sanderson, *Programming Google App Engine: Build and Run Scalable Web Apps on Google's Infrastructure*, O'Reilly Media, Inc., 2009.
- [17] J. Dean and S. Ghemawat, "MapReduce: simplified data processing on large clusters," *Communications of the ACM*, vol. 51, no. 1, pp. 107–113, 2008.
- [18] Apache Software Foundation, "Apache Spark," April 2018, <https://spark.apache.org/>.
- [19] M. Guller, *Big Data Analytics with Spark: a practitioner's Guide to Using Spark for Large Scale Data Analysis*, Springer, 2015.
- [20] G. Cavallaro, M. Riedel, C. Bodenstern et al., "Scalable developments for big data analytics in remote sensing," in *2015 IEEE International Geoscience and Remote Sensing Symposium (IGARSS)*, pp. 1366–1369, Milan, Italy, July 2015.
- [21] L. Wang, Y. Ma, J. Yan, V. Chang, and A. Y. Zomaya, "pipsCloud: high performance cloud computing for remote sensing big data management and processing," *Future Generation Computer Systems*, vol. 78, pp. 353–368, 2018.
- [22] X. Chen and L. Zhou, "The remote sensing image segmentation mean shift algorithm parallel processing based on MapReduce," in *International Conference on Intelligent Earth Observing and Applications 2015, 98083T*, Guilin, China, December 2015.
- [23] R. Giachetta, "A framework for processing large scale geospatial and remote sensing data in MapReduce environment," *Computers & Graphics*, vol. 49, pp. 37–46, 2015.
- [24] Z. Sun, F. Chen, M. Chi, and Y. Zhu, "A spark-based big data platform for massive remote sensing data processing," in *ICDS 2015 Proceedings of the Second International Conference on Data Science*, pp. 120–126, Sydney, Australia, August 2015.
- [25] W. Huang, L. Meng, D. Zhang, and W. Zhang, "In-memory parallel processing of massive remotely sensed data using an apache spark on Hadoop YARN model," *IEEE Journal of Selected Topics in Applied Earth Observations and Remote Sensing*, vol. 10, no. 1, pp. 3–19, 2017.
- [26] X. Fan, B. Lang, Y. Zhou, and T. Zang, "Adding network bandwidth resource management to Hadoop YARN," in *2017 Seventh International Conference on Information Science and Technology (ICIST)*, pp. 444–449, Da Nang, Vietnam, April 2017.
- [27] C.-Z. Qin, L.-J. Zhan, and A.-X. Zhu, "How to apply the geospatial data abstraction library (GDAL) properly to parallel geospatial raster I/O?," *Transactions in GIS*, vol. 18, no. 6, pp. 950–957, 2014.
- [28] J. W. Rouse Jr., R. H. Haas, J. A. Schell, and D. W. Deering, "Monitoring vegetation systems in the Great Plains with ERTS," in *NASA. Goddard Space Flight Center 3d ERTS-1 Symp*, College Station, TX, USA, January 1974.
- [29] S. K. McFeeters, "The use of the normalized difference water index (NDWI) in the delineation of open water features," *International Journal of Remote Sensing*, vol. 17, no. 7, pp. 1425–1432, 1996.
- [30] A. C. Frery and T. Perciano, "Image data formats and color representation," in *Introduction to Image Processing Using R. SpringerBriefs in Computer Science*, pp. 21–29, Springer, London, 2013.
- [31] US Department of the Interior, and US Geological Survey, "Landsat 8," April 2018, <https://landsat.usgs.gov/landsat-8>.
- [32] Amazon Web Services Inc, "Landsat on AWS," March 2018, <https://aws.amazon.com/public-datasets/landsat/>.
- [33] Amazon Web Services Inc, "MODIS on AWS," June 2018, <https://docs.opendata.aws/modis-pds/readme.html>.
- [34] Suez Canal Authority, "New Suez Canal," June 2017; <https://www.suezcanal.gov.eg/English/About/SuezCanal/Pages/NewSuezCanal.aspx>.
- [35] N. Gorelick, M. Hancher, M. Dixon, S. Ilyushchenko, D. Thau, and R. Moore, "Google Earth Engine: planetary-scale geospatial analysis for everyone," *Remote Sensing of Environment*, vol. 202, pp. 18–27, 2017.
- [36] P. S. Chavez, "Image-based atmospheric corrections-revisited and improved," *Photogrammetric Engineering and Remote Sensing*, vol. 62, no. 9, pp. 1025–1035, 1996.
- [37] Apache Software Foundation, "Tuning Spark," June 2018, <http://spark.apache.org/docs/latest/tuning.html#tuning-spark>.

## Research Article

# Weighted Voronoi Diagram-Based Simulation and Comparative Analysis of Ecosystem Service Coverage: Case Study of the Zhongyuan Urban Agglomeration

Pengyan Zhang,<sup>1</sup> Wenlong Jing<sup>2,3,4</sup> and Yunzeng Chen<sup>1</sup>

<sup>1</sup>College of Environment and Planning, Henan University, Kaifeng 475004, China

<sup>2</sup>Guangzhou Institute of Geography, Guangzhou 510070, China

<sup>3</sup>Key Laboratory of Guangdong for Utilization of Remote Sensing and Geographical Information System, Guangzhou 510070, China

<sup>4</sup>Guangdong Open Laboratory of Geospatial Information Technology and Application, Guangzhou 510070, China

Correspondence should be addressed to Wenlong Jing; [jingwl@reis.ac.cn](mailto:jingwl@reis.ac.cn) and Yunzeng Chen; [yzchen@henu.edu.cn](mailto:yzchen@henu.edu.cn)

Received 27 April 2018; Accepted 5 July 2018; Published 5 August 2018

Academic Editor: Yichun Xie

Copyright © 2018 Pengyan Zhang et al. This is an open access article distributed under the Creative Commons Attribution License, which permits unrestricted use, distribution, and reproduction in any medium, provided the original work is properly cited.

The future of ecology lies on the promotion of eco-economy, a resource saving and environment-friendly society, and the research of ecosystem services. This article applied weighted Voronoi diagram to simulate the ecosystem service capacity in Zhongyuan Urban Agglomeration, China, using remote sensing and geographic information systems. The results show that (1) compared with the traditional Voronoi diagram, the weighted Voronoi diagram expresses more accurate on the ecosystem service range, (2) the total value of the ecosystem service in the study area was 575.7 billion yuan in 2015. The maximum value was about 253.8 billion yuan greater than the minimum value. The unit forest ecosystem has been improved after the coefficient was modified, and the value of ecosystem services reached 32,638.87 yuan/hm<sup>2</sup>, (3) the service value of construction ecosystem has a great effect on the total value of ecosystem services; the overall pulldown effect of Kaifeng City is most considerable, and (4) the region with strong ecosystem service capacity has strong effect in annexing the nearby areas with weak ecosystem service capacity. And the distance of the annexing is inversely proportional. The closer the distance is, the stronger the annex will be.

## 1. Introduction

The survival of human societies is determined by the carrying capacity of their ecosystems [1, 2]. The idea that natural resources and environments are free causes ecological resource development to exceed ecosystems' basic carrying capacities. This, in turn, leads to the reduction or complete loss of ecosystem service functions [3, 4]. Now, more than two-thirds of services provided by ecosystems worldwide have already begun to decrease [5]; this trend may not be effectively reversed in the next 50 years [3, 4, 6]. Resource, ecological, and environmental crises have already seriously threatened China's development; for China to develop in a sustainable manner, scientific studies must establish macroscopic ecological security patterns and define key ecological spaces for prior protection. Therefore, exploring a scientific and effective method for delineating the range of ecosystem

services is of positive significance in promoting the balanced development of ecosystem services and establishing and improving the ecosystem protection policy.

Ecosystem service functions are defined as "the natural benefits which human survival relies on and which are created and maintained by ecosystems and ecological processes" [7]. To describe ecosystem service functions more intuitively, Costanza et al. [8] conducted an assessment of ecosystem service values, which has become a key ecological research topic. Estoque and Murayama [9] found that the area of urban in the city of Baguio, the summer capital of the Philippines, expanded continuously during the study period, while the ecosystem service value dropped to 40% of that at the beginning of the study. Gómez-Baggethun and Barton [10] discovered that traditional monotonous urban planning is one-sided, and that a single socioeconomic indicator cannot assure the balanced ecological and economic development of

a society. Moreover, introducing ecosystem service values has a positive impact on the development of human societies. Su et al. [11] primarily studied the Hangjiahu Plain agroecological zone, the Tianmu Mountain forest ecological zone, the Hangzhou urban ecological zone, and the Qiandao Lake Basin forest and wetland ecological zone and analyzed the effects of urbanization on regional ecosystems. Using research from around the world [12–17], Costanza et al. [6] summarized ecosystem service value assessments and further improved their evaluation. However, key research on ecosystem service values remains: for example, how should coverage of ecosystem services be delimited? How should a method of ecosystem service coverage quantification be developed?

Voronoi diagrams are partitioning that have been shown to be highly similar to some natural structures; as such, they have been studied extensively in fields including meteorology, geology, surveying and mapping, archaeology, molecular chemistry, ecology, and computer science [18, 19]. Voronoi diagrams are mainly applied to site selection and the determination of the scope of influence of different objects. Qin and Shi [20] utilized Voronoi diagrams to examine the spatial distribution of large-scale residential areas, ultimately making suggestions for planning in the region. Fan et al. [21] integrated Voronoi diagrams with spatial interaction models to investigate the Horqin Left Middle Banner, in Inner Mongolia, and proposed a method for improving this model by substituting town centrality for population size and integrating the model with weighted Voronoi diagrams. Traditional Voronoi diagrams are often used to describe the evenness of ground objects and are based on the principle of even distribution; however, they can better solve practical problems after some reasonable improvement. For example, introducing weights can compensate for the defects of traditional uniform Voronoi diagrams [22–25]. Li et al. [26] and Miao et al. [27] used Voronoi diagrams to examine parks in Shenyang and the wetland functional zone in Beijing, respectively, confirming the possibility of employing this method in ecosystem research. Nevertheless, there is still room for development in studying ecosystem services and enhancing its assessment accuracy.

To explore a suitable method of studying ecosystem service coverage areas, we introduce Voronoi diagrams and weighted Voronoi diagrams into ecosystem service value research and analyze ecosystem services coverage based on actual conditions. This approach helps quantify ecosystem service research not only at fixed points but also across regions. The Zhongyuan Urban Agglomeration is one of seven major urban agglomerations in China; it is the key development area of the Zhongyuan Economic Zone. Recent rapid social and economic development in this area has changed the types of ecosystems in the region, which in turn has led to changes in ecosystem service values in the coverage areas. In order to explore a reasonable method for estimating ecosystem service coverage areas, we will value the ecosystem services, that is, use economic methods to describe the strength of ecosystem services. Furtherly, we introduce the Voronoi diagram and the weighted Voronoi diagram to simulate and analyze the ecosystem service areas. The Voronoi

diagram, the Euclidean distance map, and the rank assignment map are compared at various levels to explore the practicality of the weighted Voronoi diagram, thereby improving the spatially estimation practices of ecosystem service and providing the scope for future ecosystem service research.

## 2. Study Area and Data Resources

*2.1. Study Area.* The Zhongyuan Urban Agglomeration (shown in Figure 1) is located in central Henan Province, China; it has a total area of 58,700 square kilometers and includes nine cities: Zhengzhou, Luoyang, Kaifeng, Xixiang, Jiaozuo, Xuchang, Luohe, Pingdingshan, and Jiyuan. This area is an important growth pole, not only of Henan Province but also of the Zhongyuan Economic Zone. In 2015, the gross national product of the agglomeration was  $2.19 \times 10^9$  yuan and its population was  $4.15 \times 10^8$ . It has a nice natural environment with a wide distribution of varied land resources, a temperate monsoon climate, high topography in the west and north, and low topography in the east and south. The eastern part of the Zhongyuan Urban Agglomeration is located in the North China Plain, which is an essential grain production base and consists mainly of farmland. The Taihang Mountains in the west and north are important production sites of forest resources. Given the premise that ecological and economic development must be constantly promoted, it is necessary to protect regional ecologies to maintain balance in regional ecosystem services. Thus, we investigate the ecosystem service coverage of different ecosystems in the region and make suggestions for regional planning.

*2.2. Data Sources.* We aim to verify the applicability of weighted Voronoi diagrams to ecosystem service value research and place little emphasis on spatial and temporal variations in ecosystem service values. Weighted Voronoi diagrams of the ecosystem service value of the Zhongyuan Urban Agglomeration in 2015 are created to examine their meaning in ecosystem service research. Land use types significantly control the functions of regional ecosystem services and are commonly used as indicators of the values of regional ecosystem services [28]. We acquired land use map of the study area by interpreting Landsat OLI images in April 2015, which is in the growing seasons and the images with low cloud cover percentages were selected. We used a manual interpretation method to derive land use maps from the remote sensing images. The land use is classified into four main types: farmland, forest, water, and construction area. To evaluate the accuracy of the land use map, we selected 110 random points from the map. The Land Use Atlas in Henan Province (1:1:100000) and high-resolution satellite images from Google Earth were referred to validate the map. As a result, the overall accuracy of the land use map is 91.3%, and the Kappa coefficient is 0.88.

## 3. Research Methods

Based on Costanza's and Daly's [13] measurement and calculation of global ecosystem service values and the

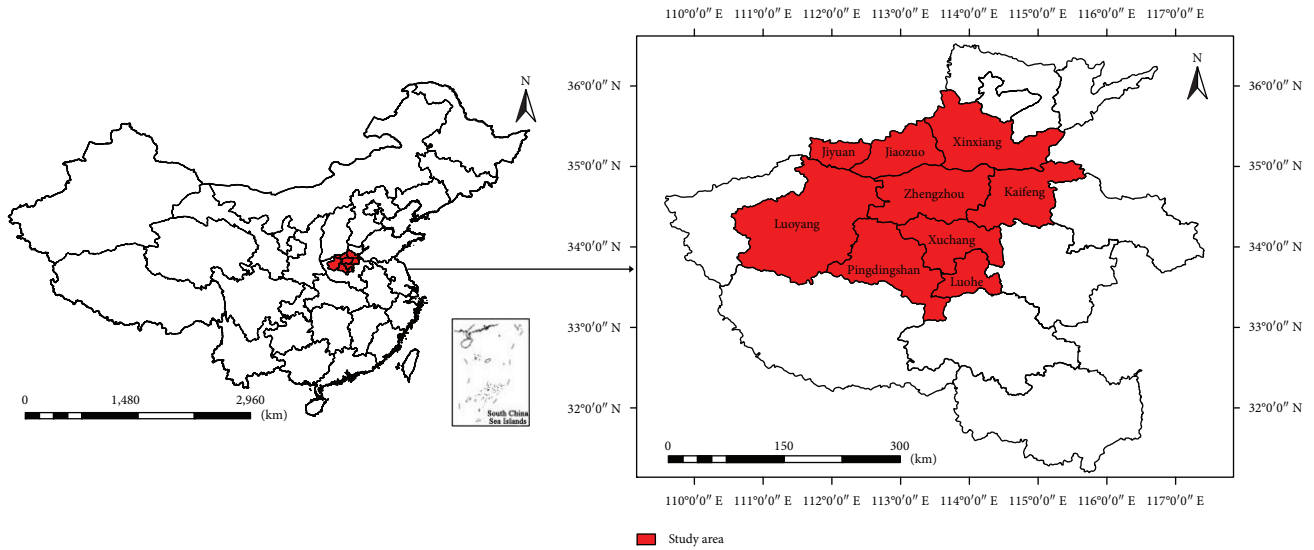


FIGURE 1: The location of the study area.

“Ecological Service Value Equivalence per Ecosystem Unit Area in China” table established by Xie et al. [29] based on actual conditions in China, this paper considers the actual condition of the Zhongyuan Urban Agglomeration to propose a novel research method, which is introduced into the correction coefficient of the study area’s ecosystem service value. ArcGIS 10.1 and MATLAB are utilized to describe the spatial distribution of ecosystem service values in the Zhongyuan Urban Agglomeration. The results are compared in color gradings, traditional Voronoi diagrams, and weighted Voronoi diagrams to analyze these methods’ advantages and drawbacks in ecosystem service value assessment (Figure 2) and provide a new perspective on ecosystem service value research.

3.1. *The Correction Coefficient Model of Ecosystem Service Values.* Based on previous research [13, 29, 30] and real-world regional conditions, the assessment coefficient of ecosystem service values (as shown in Table 1) is improved. We propose an improved model based on grain yields (1) and a correction coefficient model of ecosystem service values (2).

$$E_a = \frac{1}{7} \left( \frac{m_c p_c q_c}{M_c} \right), \quad (1)$$

$$VC_{ij} = e_{ij} E_a, \quad (2)$$

where  $E_a$  is the value of food supply services per unit agroecosystem per unit ecosystem (yuan),  $m_c$  is the crop area ( $\text{hm}^2$ ),  $q_c$  is the crop yield per unit area ( $\text{kg}/\text{hm}^2$ ),  $p_c$  is the notional average price of crops (yuan/kg),  $M_c$  is the total sown area ( $\text{hm}^2$ ),  $VC_{ij}$  denotes the equivalent value of ecosystem  $i$  for function  $j$ , and  $e_{ij}$  is the function of ecosystem service  $j$  in the  $i$ th ecosystem type relative to the food supply services provided by the agroecosystem. The  $E_a$  of the study area was calculated to be 1493.77

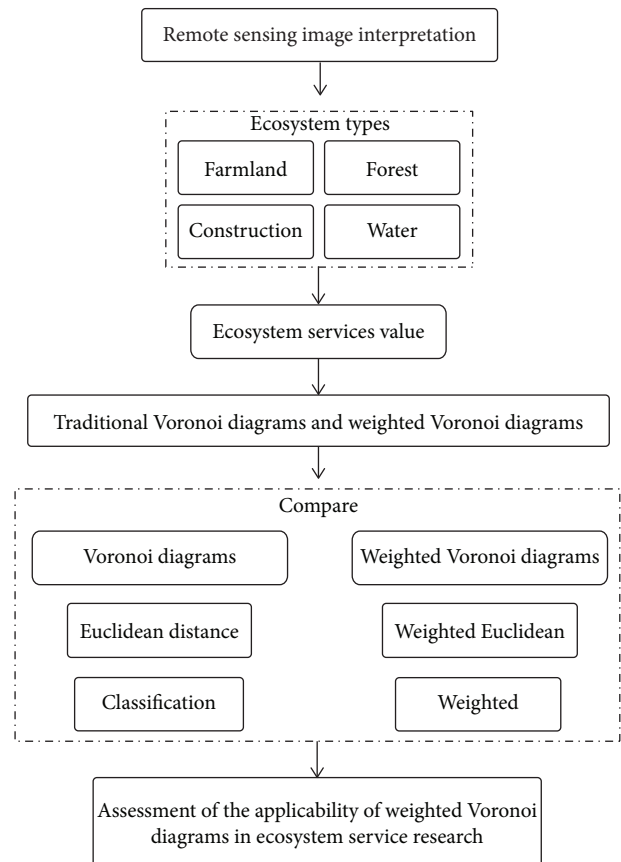


FIGURE 2: Research flowchart.

yuan/ $\text{hm}^2$ . The correction coefficient of ecosystem service value is listed in Table 1.

3.2. *The Ecosystem Service Value (ESV) Model.* The ecosystem service value (ESV) model is effective for estimating ecosystem service values based on different ecological types [30] and is expressed as illustrated in (3) and (4).

TABLE 1: Correction coefficient of ecosystem services values (y/hm<sup>2</sup>·a).

Service type	Forest ecosystem	Farm ecosystem	Water ecosystem	Construction ecosystem
Gas regulation	5228.19	746.88	0.00	0.00
Climate regulation	4033.17	1329.45	687.13	0.00
Water conservation	4780.06	896.26	30443.03	-14325.25
Soil formation and protection	5825.70	2180.90	14.93	0.00
Waste disposal	1956.83	2449.78	27156.73	-4660.56
Biodiversity conservation	4869.69	1060.57	3734.42	0.00
Food production	149.37	1493.77	448.13	0.00
Raw material	3883.80	149.377	104.56	0.00
Entertainment culture	1912.02	14.9377	8290.42	0.00
Total	32638.87	10321.95	93674.31	-18985.81

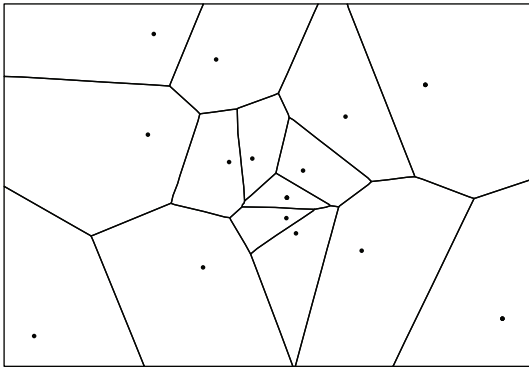


FIGURE 3: Traditional Voronoi diagram.

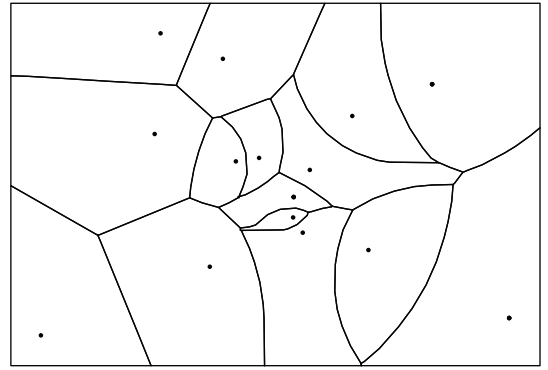


FIGURE 4: Weighted Voronoi diagram.

$$ESV_{ij} = A_i \times VC_{ij}, \quad (3)$$

$$ESV_i = \sum_{j=1}^n ESV_{ij}, \quad (4)$$

where  $ESV$  is the ecosystem service value (yuan),  $A_i$  is the area of the  $i$ th ecosystem type, and  $VC_{ij}$  denotes the equivalent coefficient of function  $j$  for ecological land  $i$ .

**3.3. Voronoi Diagrams.** Voronoi diagrams (abbreviated as  $V$  diagrams, as shown in Figure 3) were proposed by Ukrainian mathematician Voronoi in 1908 and were applied to high-dimensional spaces. By assuming that for a set of discrete points on Euclidean plane  $P = \{P_1, P_2, \dots, P_n\}$ , where any two arbitrary points are noncoincident (i.e.,  $P_i \neq P_j, i \neq j, 1 \leq i, j \leq n$ ) and any four arbitrary points are nonconcyclic,  $V(P_1) \cdots V(P_i)$  is calculated as

$$V(P_i) = \bigcap_{i \neq j} \{P | d(P, P_i) < d(P, P_j)\} \quad j = 1, 2, \dots, n, \quad (5)$$

where  $d(P, P_i)$  is the Euclidean distance between points  $P$  and  $P_i$ . Thus, the distance from each point  $P$  that belongs to  $V(P_i)$  is closer to  $P_i$  than any other points  $P_j (i \neq j)$  of discrete point set  $P$ .

**3.4. Weighted Voronoi Diagrams.** Although Voronoi diagrams can depict the basic characteristics of some natural

environments, they are unable to present the condition of some relatively complex ground objects. Based on traditional Voronoi diagrams, weighted Voronoi diagrams (as shown in Figure 4) introduce weight indices and convert traditional Euclidean distances into weighted Euclidean distances [31]. Given that  $P = \{P_1, P_2, \dots, P_i\}$ , nonnegative real number weights  $\lambda_i (i = 1, 2, \dots, n)$  are introduced; hence, the weighted distance between points  $P$  and  $P_i$  is

$$D(P, P_i) = \frac{d(P, P_i)}{\lambda_i}. \quad (6)$$

Then,  $V(P_i)$  should be revised to

$$V(P_i) = \bigcap_{i \neq j} \{P | D(P, P_i) < D(P, P_j)\} \quad j = 1, 2, \dots, n. \quad (7)$$

When  $\lambda_1 = \lambda_2 = \dots = \lambda_n$ , weighted Voronoi diagrams become traditional Voronoi diagrams.

## 4. Results and Analysis

**4.1. Ecosystem Service Value Assessment.** The Zhongyuan Economic Zone has lately been an important economic development region in China; more importantly, it is also the key region for stimulating the development of the central region of China and promoting balance in China's economic development. Because the Zhongyuan Urban Agglomeration is the key region of the Zhongyuan Economic Zone,

TABLE 2: Comparison of different types of ecosystem service value coefficient.

Ecosystem service value coefficient	Forest ecosystem	Farm ecosystem	Water ecosystem	Construction ecosystem
Costanza [13] (yuan·hm <sup>-2</sup> ·a <sup>-1</sup> )	8035.3	761	26487.4	None
Xie et al. [29] (yuan·hm <sup>-2</sup> ·a <sup>-1</sup> )	12628.69	3547.89	44963.9	None
Modified (yuan·hm <sup>-2</sup> ·a <sup>-1</sup> )	32638.87	10321.95	93674.31	-18985.81

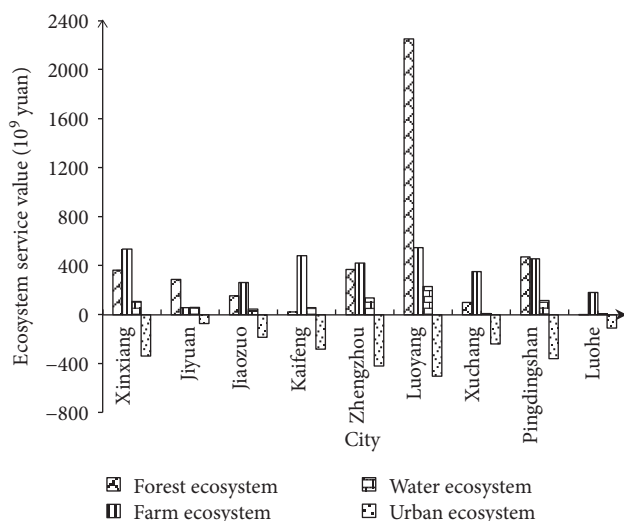


FIGURE 5: Ecosystem service values of nine cities in the Zhongyuan Urban Agglomeration.

its overall economic development acts as a model for the development of other regions. Therefore, proper ecosystem planning in the agglomeration and balanced ecological and economic development of the region enhances its competitiveness and encourages the development of other regions.

Before ecosystem service value assessment was completed, Costanza and Daly [13] and Xie et al. [29] performed coefficient correction of ecosystem service values according to real-world conditions in the study area. The results are listed in Table 2.

The coefficients of ecosystem service values in Table 2 and the ecosystem of different land use areas in the Zhongyuan Urban Agglomeration after satellite image interpretation were integrated to assess the ecosystem service value of each land use of the region. The results are shown in Figure 5.

The total ecosystem service value of the Zhongyuan Urban Agglomeration in 2015 was 575.7 billion yuan. The ecosystem service value of Luoyang was the highest, accounting for 43.93% of the regional total; in contrast, that of Luohe was only 1.42% of the regional total. Furthermore, the forest ecosystems of Luoyang contributed the most to the total ecosystem service value of the city, accounting for 89.09% of the total. The total ecosystem service value of Kaifeng was 28.259 billion yuan, of which the value of farm ecosystem was 48.216 billion yuan, whereas the loss in value caused by construction ecosystem expansion was up to 28.037 billion yuan. The ecosystem types combined with the administrative area could lead to the differences of ecosystem service values. Specifically, higher proportion of forest and water ecosystems in a region would increase the region's ecosystem

service values and furtherly have positive influences upon the neighbor ecosystems.

**4.2. Simulation of Ecosystem Service Coverage.** Similar to social services, ecological services have coverage directly related to their intensity. Past ecosystem service studies could not determine the areas of influence of multiple service functions. For example, the ecosystem service function of climate regulation by forest ecosystems is affected by several factors and it is not possible to accurately assess specific service coverage. Hence, selecting an appropriate angle for measuring and calculating ecosystem service coverage can compensate for shortcomings in previous research.

Ecosystem service values quantify all kinds of ecosystem service functions and present them intuitively. The appearance of this variable allows ecosystem service coverage to be simulated and analyzed using an economic approach. The resulting Voronoi diagrams are shown in Figure 6 in a map showing a uniform distribution; however, there are considerable differences in ecosystem service values between cities. A uniform distribution cannot correctly depict the actual coverage of ecosystem services. Therefore, ecosystem service values of different regions are presented as weighted Voronoi diagrams, which partly compensate for defects in the expression of service coverage by traditional Voronoi diagrams.

The ecosystem service values of all cities in the Zhongyuan Urban Agglomeration were used as weight indices to improve the original Voronoi diagrams, as illustrated in Figure 7. These results, together with the data in Figure 5, demonstrate that the ecosystem service value of Luoyang accounts for a significant portion of the total ecosystem service value of the Zhongyuan Urban Agglomeration. Its influence is considerably greater than those of other cities. Integration of the different service boundaries of Figures 5 and 7 shows that, taking Luoyang as an example, the ecosystem service value coverage of the city expands significantly, which is highly related to the larger ecosystem service value of the city. For regions with lower service values, such as Jiyuan and Luohe, except for certain preserved coverage, areas are impacted by regions with greater ecosystem service values. That is, if the ecosystem service value is greater, the service coverage is more extensive. To an extent, these areas affect and compensate for areas with smaller ecosystem service values.

To highlight the interactions and relationships between ecosystem services of different regions, we classified ecosystem service coverage using the Jenks natural breaks classification method into five types: high-, medium to high-, medium-, medium to low-, and low-impact areas. The traditional Voronoi diagrams are compared with the weighted ones in Figure 8.

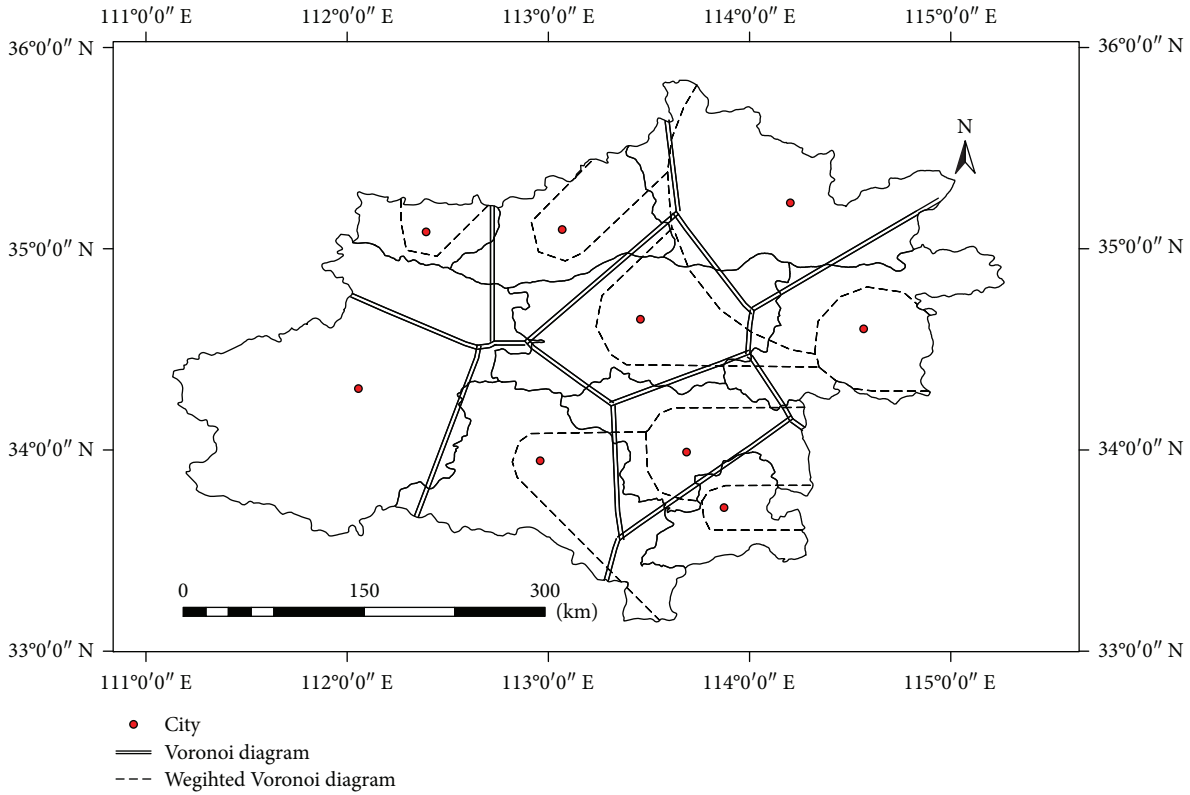


FIGURE 6: Comparison of the traditional and weighted Voronoi diagrams of the study area.

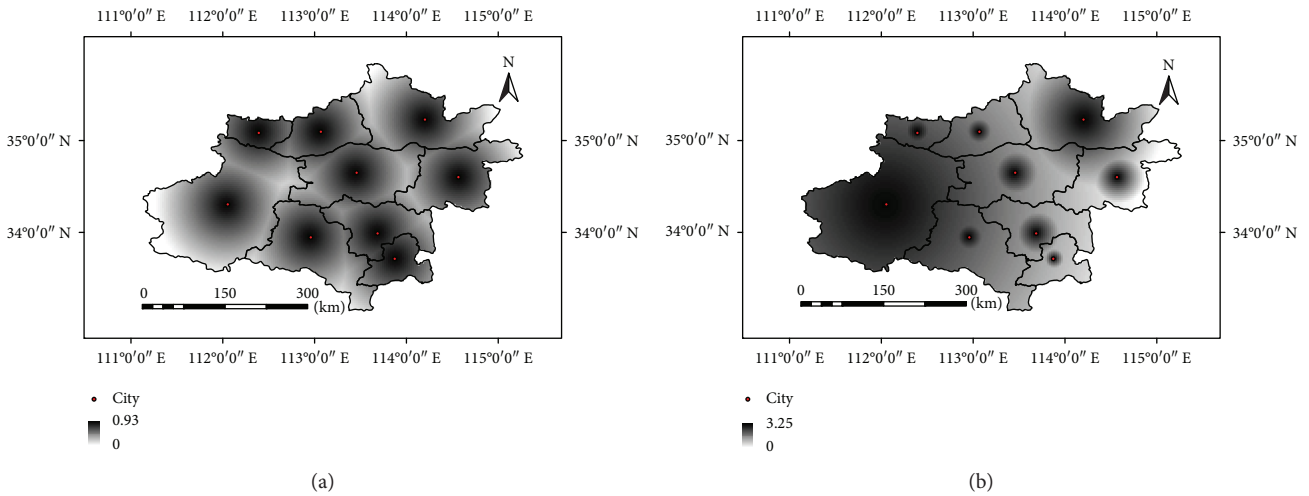


FIGURE 7: Comparison of Euclidean distances between (a) the traditional Voronoi diagrams and (b) weighted Voronoi diagrams of the study area.

As shown in Figure 8, regions may have various effects on each other, although the center of each region is mainly influenced by the region itself. In addition, regions with greater ecosystem service capabilities compensate for regions with lower capabilities, which conceal the originally insignificant ecosystem service capabilities of regions with lower service capacities. The ecosystem service interactions engulfing different regions can be monitored and controlled artificially. Rational distribution of ecosystems over the study area will

considerably enhance a region’s ecosystem service capability and thus its ecosystem service quality. If the stepwise progressive decreases of different kinds of ecosystem service capabilities can be successfully determined, it would be possible to more accurately evaluate the influences and coverage of ecosystem services.

From the total ecosystem service value in Figure 8, the type of ecosystem that dominates the total ecosystem services can be seen and various types of ecosystem service coverage

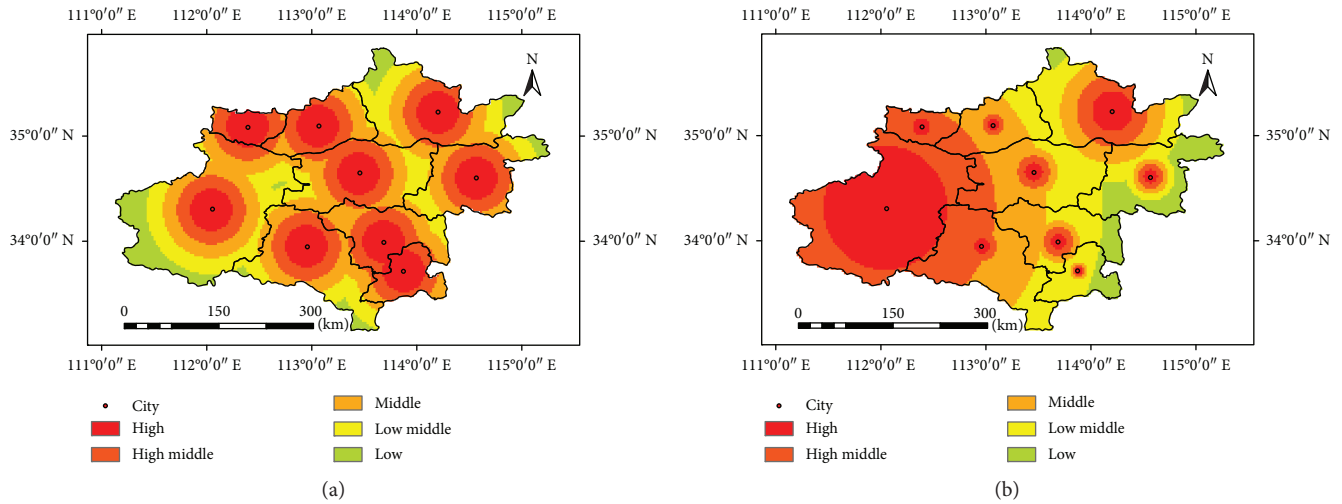


FIGURE 8: Comparison of ecosystem service classification between (a) traditional Voronoi diagrams and (b) weighted Voronoi diagrams of the study area.

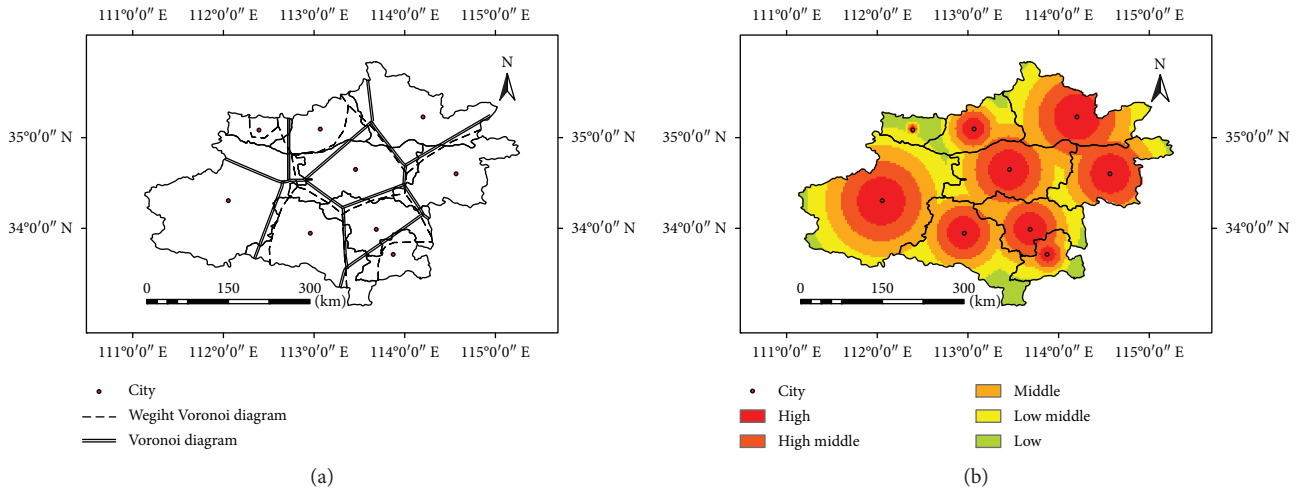


FIGURE 9: Service impact ranges of (a) traditional Voronoi diagram and (b) weighted Voronoi diagram in farmland ecosystem.

can be studied. Thus, the uneven distribution of land use types between regions can be obtained. We illustrate the ecosystem service capabilities and coverage of farm ecosystem, forest ecosystems, water ecosystems, and construction ecosystems of regions in the Zhongyuan Urban Agglomeration in Figures 9–12.

Excluding Jiyuan, Luohe, and Jiaozuo, the farmland ecosystem service values of the study area were 40–60 billion yuan. According to Figures 9–12, it is obvious that regions with less farmland ecosystem service capability are more considerably affected by regions with greater capabilities. For regional division, compared to traditional Voronoi diagrams, the weighted Voronoi diagrams also consider the actual spatial distribution of farmland. Additionally, compared to the traditional Voronoi diagrams, which use color grading to represent ecosystem service values, the weighted diagrams reflect the progressive reduction over space and the nonuniformity of ecosystem services, more closely representing reality. Traditional ecosystem service value evaluation only

considers the ecosystem service capabilities of cities, but not the direct interactions between cities, whereas weighted Voronoi diagrams can better explain these interactions. Construction ecosystems cause negative ecosystem service values and lower overall ecosystem service capabilities. Therefore, during calculation, all construction was assigned positive values. High-impact areas are those that are more greatly affected by construction ecosystems. The ecosystem service value losses of these areas are significantly higher than those of other areas. Areas with higher levels of urbanization and more extensive construction experience stronger reduction. In the study area, there are more forest ecosystems in the west and fewer in the east. Thus, areas with higher forest ecosystem service capabilities impose greater influences on areas with lower capabilities. Luoyang has vast forest ecosystems. Strong forest ecosystem service capability is the basic characteristic of the city’s ecosystem services; Luoyang’s ecosystem service value is 6.91, 7.32, 15.06, 119.42, 10.15, 27.3, 27.3, and 323.29 times of those of Xinxiang, Jiyuan, Jiaozuo,

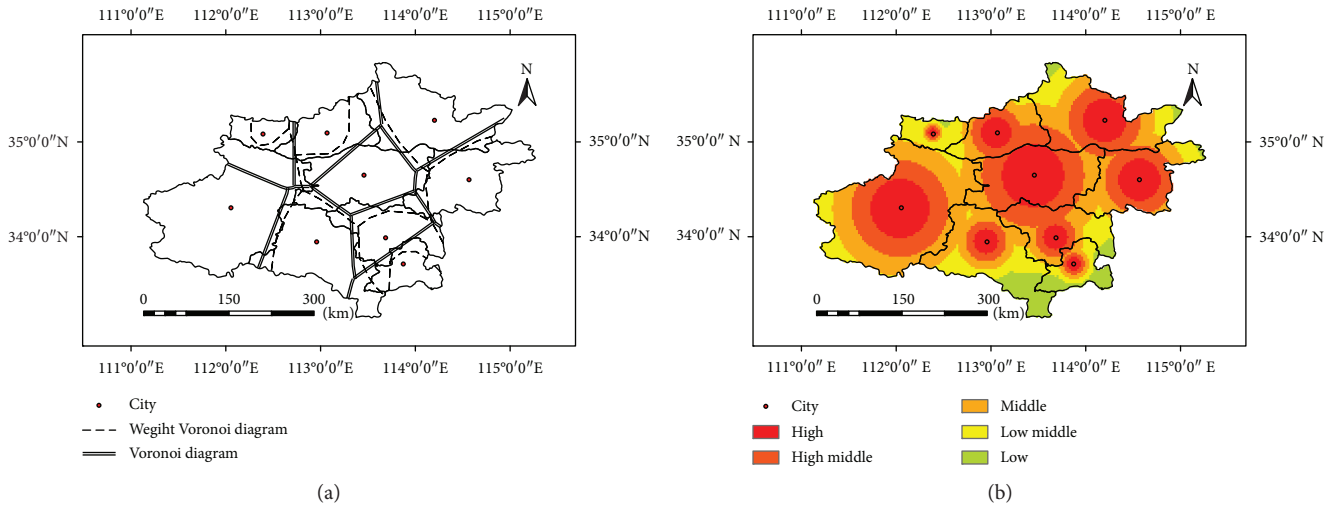


FIGURE 10: Service impact ranges of (a) traditional Voronoi diagram and (b) weighted Voronoi diagram in construction ecosystem.

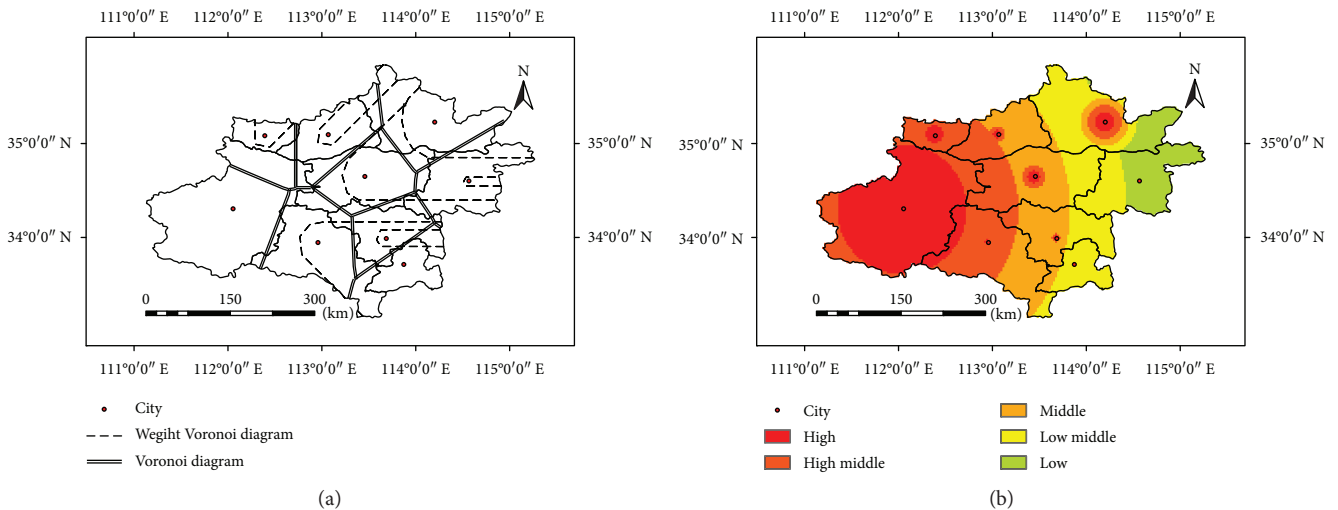


FIGURE 11: Service impact ranges of (a) traditional Voronoi diagram and (b) weighted Voronoi diagram in forest ecosystem.

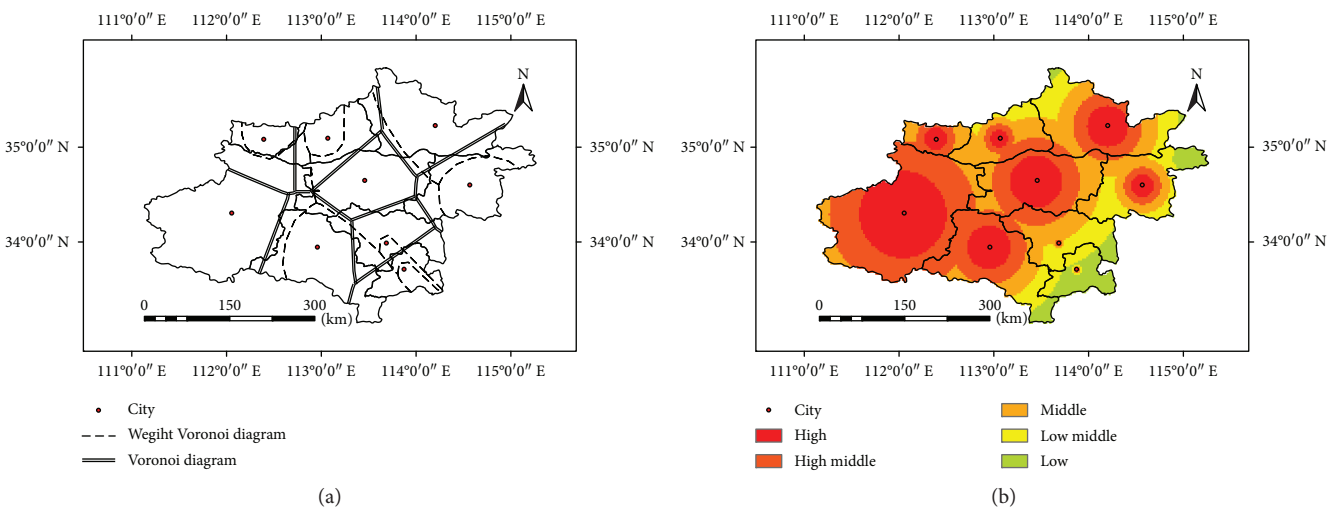


FIGURE 12: Service impact ranges of (a) traditional Voronoi diagram and (b) weighted Voronoi diagram in water ecosystem.

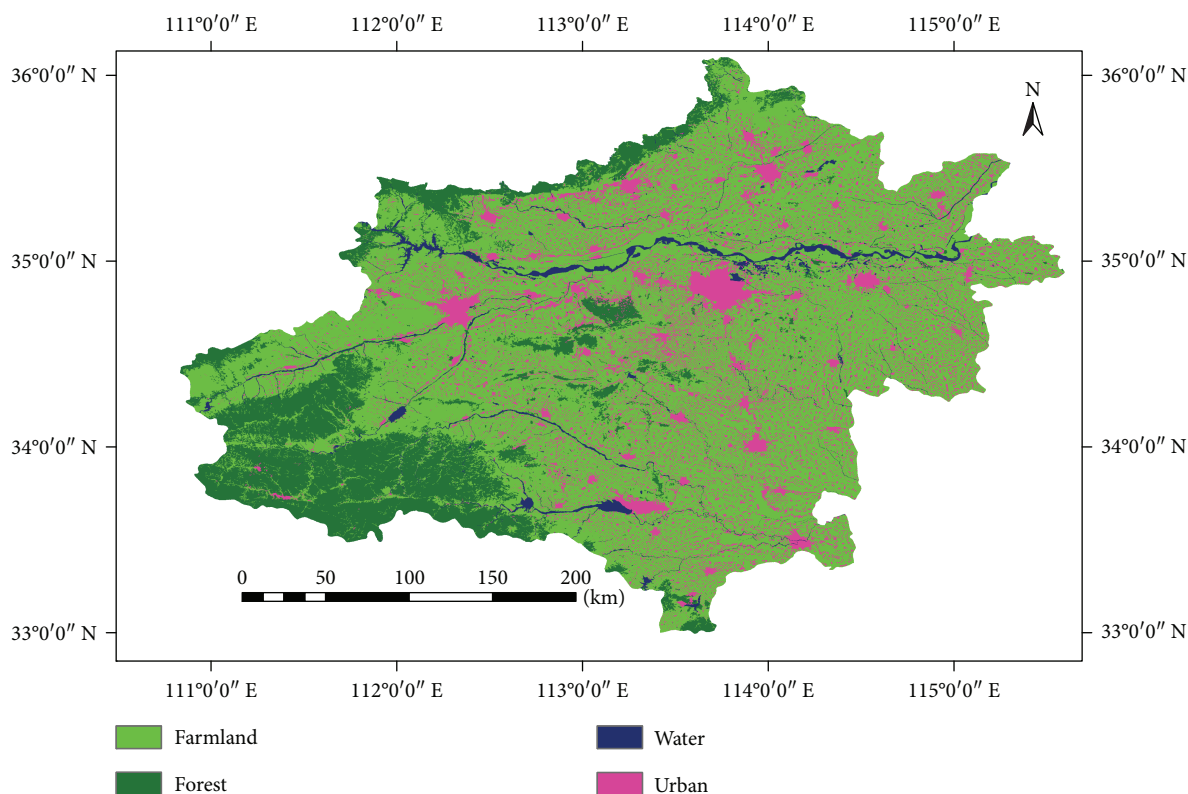


FIGURE 13: Remote sensing image interpretation data of the Zhongyuan Urban Agglomeration in 2015.

Kaifeng, Zhengzhou, Xuchang, Pingdingshan, and Luohe, respectively. Engulfing effects and compensation due to the forest ecosystem services of Luoyang gradually weaken with distance. However, the low-impact forest ecosystem service area of the city still has relatively significant effects on other areas. The weighted Voronoi diagrams, compared to the traditional Voronoi diagrams, have the advantage of intuitively presenting ecosystem service capabilities and their coverage over space. The coverage of water ecosystem services and the actual distribution of water ecosystems are relatively strongly correlated. The Yellow River runs through the central and the central-north regions of the Zhongyuan Urban Agglomeration. Rivers in Luoyang are widely distributed, which places Luohe in a low-impact water ecosystem service area. This distribution of high-impact areas in the northwest and low-impact areas in the northeast matches the satellite image interpretation results. Comparison between the satellite image interpretation (Figure 13) and ecosystem service coverage map reveals that high-, medium-, and low-impact ecosystem service areas are directly related to the distinct types of ecosystems in different cities, further confirming that weighted Voronoi diagrams are suitable for simulation of ecosystem service coverage and provide a new method and direction for these studies.

## 5. Discussion and Conclusion

**5.1. Discussion.** This study employs cities as central points for investigating ecosystem service coverage. This method

considers an entire region and thereby presents the spatial distribution of ecosystem services, providing a new perspective for ecosystem service coverage research. Nevertheless, this method neglects nonuniform ecosystem distributions, ecosystem distribution within the region, and the interactions between ecosystems, which reduce the accuracy of ecosystem service coverage research. Thus, in future studies, better results can be obtained if fixed point studies can be conducted for different land use types.

Ecosystem service capabilities were classified using the Jenks natural breaks classification method. Although this method can partly reveal the basic features of research topics and data, it neglects the gradual reduction in service distance of service providers and the acceptance capabilities of service. Proper investigation of the gradual decrease of different ecosystem services over distance, and the acceptance rates of different service providers, allows the new method to be better applied to the actual production activities.

**5.2. Conclusions.** The total ecosystem service value of the Zhongyuan Urban Agglomeration in 2015 was 575.7 billion yuan. The total ecosystem service value of Luoyang was the highest, at 267.665 billion yuan; that of Luohe was the lowest, at only 13.881 billion yuan. The differences between regions are huge. Forest ecosystems have the greatest ecosystem service value per unit area—up to 32.639 thousand yuan per hm. Meanwhile, construction ecosystem service values significantly reduce the service values of different ecosystem types. Continuous expansion of construction ecosystems has

decreased the ecosystem service value of Zhengzhou by 37.012 billion yuan, with the most remarkable decline seen in Kaifeng.

Compared to traditional Voronoi diagrams, weighted Voronoi diagrams are more suitable for studying ecosystem service coverage. Comparison between the two indicates that the spatial coverage of ecosystem services presented by the weighted Voronoi diagrams better fit actual conditions. Traditional Voronoi diagrams describe uniform ecosystem services and neglect the discrepancies in actual service coverage caused by regional differences. In weighted Voronoi diagrams, regions with higher ecosystem service capabilities partly engulf and compensate for regions with lower capabilities. These engulfing and compensating actions are inversely proportional to the distance between two regions. When two ecosystems are closer to each other, their interactions are stronger. The region with lower capability is more easily engulfed by the region with higher capability, and the ecosystem services of the former are enhanced. These actions partly contribute to the spatial and temporal distribution of ecosystems in the region and promote the union of different regions, thereby enhancing overall regional ecosystem service capability.

The ecosystem service coverage of farm ecosystem, forest ecosystems, water ecosystems, and construction ecosystems was studied separately, and the results compared to actual conditions. We found that the two agree relatively well, again proving that weighted Voronoi diagrams perform well in assessing ecosystem service coverage. The service coverage of different ecosystem types was also examined. We discovered that, for larger differences in ecosystem type and size between different regions, weighted Voronoi diagrams differ more significantly than their traditional counterparts. This result demonstrates that, for two regions whose ecosystem service differences are relatively large, traditional Voronoi diagrams do not match actual service coverage.

## Data Availability

The readers can contact the authors to access the data in the manuscript.

## Disclosure

The content does not represent the official position of the Chinese government and is entirely the responsibility of the authors.

## Conflicts of Interest

The authors declare that they have no conflicts of interest.

## Acknowledgments

This paper was supported by the National Natural Science Foundation of China (41601175 and 41771380). The Key Scientific Research Project of Henan Province (16A610001), supported by the Program for Innovative Research Team (in Science and Technology) in the University of Henan

Province (16IRTSTHN012), the GDAS' Project of Science and Technology Development (2017GDASCX-0101 and 2018GDASCX-0904), the Guangdong Innovative and Entrepreneurial Research Team Program (2016ZT06D336), the Science and Technology Program of Guangdong Province (2017B010117008), and the Science and Technology Program of Guangzhou (201604016047).

## References

- [1] D. E. Campbell, "Emergy analysis of human carrying capacity and regional sustainability: an example using the state of Maine," *Environmental Monitoring and Assessment*, vol. 51, no. 1/2, pp. 531–569, 1998.
- [2] E. S. Nakajima and E. Ortega, "Carrying capacity using emergy and a new calculation of the ecological footprint," *Ecological Indicators*, vol. 60, pp. 1200–1207, 2016.
- [3] N. M. Haddad, L. A. Brudvig, J. Clobert et al., "Habitat fragmentation and its lasting impact on Earth's ecosystemse1500052," *Science Advances*, vol. 1, no. 2, 2015.
- [4] N. M. Haddad, L. A. Brudvig, J. Clobert et al., "Habitat fragmentation and its lasting impact on Earth's ecosystems," *Science Advances*, vol. 1, no. 2, article e1500052, 2015.
- [5] Millennium Ecosystem Assessment, *Ecosystems and Human Well-Being: Biodiversity Synthesis*, WorldResources Institute, Washington DC, 2005.
- [6] R. Costanza, R. de Groot, P. Sutton et al., "Changes in the global value of ecosystem services," *Global Environmental Change*, vol. 26, no. 1, pp. 152–158, 2014.
- [7] Z. Ouyang, T. Zhao, X. Wang, and H. Miao, "Ecosystem services analyses and valuation of China terrestrial surface water system," *Acta Ecologica Sinica*, vol. 24, no. 10, pp. 2091–2099, 2004.
- [8] R. Costanza, R. d'Arge, R. de Groot et al., "The value of the world's ecosystem services and natural capital," *Nature*, vol. 387, no. 6630, pp. 253–260, 1997.
- [9] R. C. Estoque and Y. Murayama, "Landscape pattern and ecosystem service value changes: implications for environmental sustainability planning for the rapidly urbanizing summer capital of the Philippines," *Landscape and Urban Planning*, vol. 116, pp. 60–72, 2013.
- [10] E. Gómez-Baggethun and D. N. Barton, "Classifying and valuing ecosystem services for urban planning," *Ecological Economics*, vol. 86, pp. 235–245, 2013.
- [11] S. Su, R. Xiao, Z. Jiang, and Y. Zhang, "Characterizing landscape pattern and ecosystem service value changes for urbanization impacts at an eco-regional scale," *Applied Geography*, vol. 34, pp. 295–305, 2012.
- [12] J. F. Barlow, "A change effects all the organisms in the ecosystem," *South Dakota Journal of Medicine*, vol. 47, no. 6, p. 186, 1994.
- [13] R. Costanza and H. E. Daly, "Natural capital and sustainable development," *Conservation Biology*, vol. 6, no. 1, pp. 37–46, 1992.
- [14] E. Matthews, "Global vegetation and land use: new high-resolution data bases for climate studies," *Journal of Applied Meteorology*, vol. 22, no. 3, pp. 474–487, 1983.
- [15] D. Pauly and V. Christensen, "Primary production required to sustain global fisheries," *Nature*, vol. 374, no. 6519, pp. 255–257, 1995.

- [16] H. Jack Ruitenbeek, "Functions of nature: evaluation of nature in environmental planning management and decision making," *Ecological Economics*, vol. 14, no. 3, pp. 211–213, 1995.
- [17] J. H. Ryther, "Photosynthesis and fish production in the sea," *Science*, vol. 166, no. 3901, pp. 72–76, 1969.
- [18] J. Liu, X. Sun, and S. Liu, "Weighted node network Voronoi diagram and its application to optimization of chain stores layout," *International Journal of Machine Learning and Cybernetics*, vol. 7, no. 4, pp. 679–688, 2016.
- [19] A. Okabe, B. Boots, and K. Sugihara, "Nearest neighbourhood operations with generalized Voronoi diagrams: a review," *International Journal of Geographical Information Science*, vol. 8, no. 1, pp. 43–71, 1994.
- [20] Y. Qin and X. Y. Shi, "Optimizing spatial distribution of residential areas based on Voronoi diagram," *Science of Surveying and Mapping*, vol. 1, pp. 136–138, 2012.
- [21] Q. Fan, H. X. Zhang, Y. H. Li, and J. X. Wang, "Quantitative analysis and urban system planning of county area based on spatial-interaction model: a case in Horqin Left Middle Banner," *Inner Mongolia, Scientia Geographica Sinica*, vol. 34, no. 5, pp. 601–607, 2014.
- [22] C. Xy, L. Jp, L. Chen, and H. Yj, "Intraspecific and interspecific competition analysis of *Cunninghamia lanceolata* ecological forest based on weighted Voronoi diagram," *Chinese Journal of Ecology*, vol. 35, no. 9, pp. 2553–2561, 2016.
- [23] J. Y. Gu, Y. G. Zhou, and L. M. Guo, "Urban influence regions and spatial relation of Beijing-Tianjin Hebei region based on weighted Voronoi diagram and breakpoint theory," *Geography and Geo-Information Science*, vol. 30, no. 1, pp. 65–69, 2014.
- [24] X. W. Qin, S. Q. Zhang, X. F. Li, X. D. Na, X. Pan, and H. Yu, "Assessment of red-crowned crane's habitat suitability based on weights-of-evidence," *Acta Ecologica Sinica*, vol. 29, no. 3, pp. 1074–1082, 2009.
- [25] S. Xie, X. Feng, J. Wang, and W. Lu, "Radiation domain of commercial centers in Nanjing based on analysis of road network weighted Voronoi diagram," *Acta Geographica Sinica*, vol. 64, no. 12, pp. 1467–1476, 2009.
- [26] X. M. Li, C. F. Liu, and W. Wu, "Recreational pressure of urban parks in Shenyang," *Chinese Journal of Ecology*, vol. 28, no. 5, pp. 992–998, 2009.
- [27] L. L. Miao, W. G. Jiang, S. D. Wang, and L. Zhu, "Comprehensive assessments and zoning of ecological service functions for Beijing wetland based on RS and GIS," *Remote Sensing for Land and Resources*, vol. 25, no. 3, pp. 102–108, 2013.
- [28] P. H. Verburg, K. H. Erb, O. Mertz, and G. Espindola, "Land system science: between global challenges and local realities," *Current Opinion in Environmental Sustainability*, vol. 5, no. 5, pp. 433–437, 2013.
- [29] G. D. Xie, L. Zhen, C. X. Lu, Y. Xiao, and C. Chen, "Expert knowledge based valuation method of ecosystem services in China," *Journal of Natural Resources*, vol. 23, no. 5, pp. 911–919, 2008.
- [30] F. Zhou, S. Y. Chen, and M. F. Wu, "Land utility structure changing trend and its response to ecological service functions—a case study in Zhanjiang City," *Journal of Safety and Environment*, vol. 7, no. 5, pp. 76–79, 2007.
- [31] S. M. Feng, "Study on service coverage of distribution center based on Voronoi diagram," in *2009 International Conference on Information Engineering and Computer Science*, vol. 29no. 3, pp. 142–144, Wuhan, China, December 2009.

## Research Article

# Detection of *Firmiana danxiaensis* Canopies by a Customized Imaging System Mounted on an UAV Platform

Chun Liu <sup>1</sup>, Mengchi Ai <sup>1</sup>, Zhuo Chen <sup>1</sup>, Yuan Zhou,<sup>2</sup> and Hangbin Wu <sup>1</sup>

<sup>1</sup>College of Surveying and Geo-Informatics, Tongji University, Shanghai 200092, China

<sup>2</sup>Tongfang Surveying Engineering and Technology Co. Ltd., Shanghai 200092, China

Correspondence should be addressed to Mengchi Ai; 1610954@tongji.edu.cn

Received 1 February 2018; Accepted 27 March 2018; Published 27 May 2018

Academic Editor: Zongyao Sha

Copyright © 2018 Chun Liu et al. This is an open access article distributed under the Creative Commons Attribution License, which permits unrestricted use, distribution, and reproduction in any medium, provided the original work is properly cited.

The objective of this study was to test the effectiveness of mapping the canopies of *Firmiana danxiaensis* (FD), a rare and endangered plant species in China, from remotely sensed images acquired by a customized imaging system mounted on an unmanned aerial vehicle (UAV). The work was conducted in an experiment site (approximately 10 km<sup>2</sup>) at the foot of Danxia Mountain in Guangdong Province, China. The study was conducted as an experimental task for a to-be-launched large-scale FD surveying on Danxia Mountain (about 200 km<sup>2</sup> in area) by remote sensing on UAV platforms. First, field-based spectra were collected through hand-held hyperspectral spectroradiometer and then analyzed to help design a classification schema which was capable of differentiating the targeted plant species in the study site. Second, remote-sensed images for the experiment site were acquired and calibrated through a variety of preprocessing steps. Orthoimages and a digital surface model (DSM) were generated as input data from the calibrated UAV images. The spectra and geometry features were used to segment the preprocessed UAV imagery into homogeneous patches. Lastly, a hierarchical classification, combined with a support vector machine (SVM), was proposed to identify FD canopies from the segmented patches. The effectiveness of the classification was evaluated by on-site GPS recordings. The result illustrated that the proposed hierarchical classification schema with a SVM classifier on the remote sensing imagery collected by the imaging system on UAV provided a promising method for mapping of the spatial distribution of the FD canopies, which serves as a replacement for field surveys in the attempt to realize a wide-scale plant survey by the local governments.

## 1. Introduction

Forests play a vital role on global carbon cycle. Understanding constitution and spatial distribution patterns of plant species in forestry is a major concern of botanists and environmentalists [1]. Great effort has been input to distinguish the plant species of forests and analyze their distribution. As an effective tool to acquire land coverage over vast regions, remote sensing technology has been applied on detection of forests. Several studies have conducted mapping of forest distribution and extraction of the species composition by applying remote sensing mounted on satellites and unmanned aerial vehicles (UAVs) [2]. The obvious advantage of satellite remote sensing is its capability in monitoring vegetation condition and forest resources over a large-scale area in a fast and cost-effective manner [3]. For instance,

satellite remote sensing data has been approved effective in mapping the outline of a forest area in order to monitor the deforestation [4]. Remote sensing products supported by satellite platforms range from high spatial resolution to low resolution. Typical examples of high-resolution imagery from satellite platforms include Spot and WorldView-2 images which were used to identify urban tree species to assess the ecological services [5]. More coarse remote sensing imageries, such as the medium-resolution products from Landsat Thematic Mapper (TM) and high-resolution imagery Enhanced Thematic Mapper Plus (ETM+), were probably only suitable for mapping distribution of grouped plant species with an advantage of covering a larger area [6]. Recently, applications of remote sensing imagery acquired by an UAV have increased dramatically in various fields. Compared to satellite remote sensing, UAV remote sensing enhanced the

ability to acquire high-spatial resolution images [7]. The application of UAV remote sensing included vegetation health monitoring, detailed composition analysis of plant species, and biomass estimation [8]. Further, remotely sensed images by UAVs provided important data resources for building high-resolution airborne orthophoto maps and point clouds which have been extensively applied in ecological studies [9].

In the area of forest monitoring, dynamic mapping of plant composition, properties of plant canopies, and forest health is an important task and remote sensing technology has been widely used as a data acquisition tool for such a purpose. For example, a metric camera mounted on an UAV was used to classify riparian forest species and to analyze the composition of forests [10]. Hill et al. examined whether such an UAV would be capable of creating accurate maps of the extent of patches of a single invasive plant, called IRIS (*Iris pseudacorus* L.) and they found that manual interpretation of the UAV-acquired imagery produced the most accurate maps, suggesting that more studies on automatic extraction of plant species are still needed to improve the classification performance from UAV images [11]. Other studies used the high-spatial resolution images acquired on UAV platforms to investigate detailed plant communities [12]. Recent advances in UAV-based remote sensing technology provide a way for obtaining highly densified point clouds from remotely sensed targets, which are useful for building a 3-D canopy structure for trees in forestry [13]. When 3-D data derived from images on UAV platforms and a digital elevation model were combined, it is possible to measure the height of plants and calculate the magnitude of changes in shape for the mapped plant species with great flexibility [14]. Zhang et al. designed a remote sensing system mounted on a light-weight drone for long-term forest monitoring and, based on the acquired data, built the canopy height model (CHM), which was useful for analyzing the species richness and abundance distributions [15]. In another application, an imaging system with near-infrared and RGB channels mounted on an UAV platform was used to investigate diseases and insect pests of vegetation [16]. Numerous studies have tested the effectiveness of mapping plant species of forests from remote sensing images. To better extract plant species and evaluate their health, Nāsi et al. used RGB orthoimages, along with hyperspectral imagery collected on UAV platforms, to identify plants and map bark beetle damage on an individual tree level [17]. However, in some cases where vegetation species presented low dissimilarity in spectra and texture in remote sensing images, it was difficult to distinguish among them. For instance, *Firmiana danxiaensis* (FD), a Chinese unique and endangered Indus species, is one example that is difficult to be detected due to its growth condition and characteristics [18].

While recent advancement in remote sensing platforms provided possible data sources from which plant species could be potentially detected, an alternative approach for improving the result in vegetation mapping looks for advanced image classifiers. Many classification methods such as random forest (RF), artificial neural network (ANN), decision trees (DT), and support vector machine (SVM) have

been proposed and applied for extracting vegetation cover from remotely sensing images. For example, Michez et al. used RF to detect riparian invasive plant species with unmanned aerial systems imagery [19]. Kwon et al. used ANNs to classify the forest vertical structure from digital images and Lidar data [20]. Frick et al. used a DT model to classify and analyze the vegetation composition in rewetted peat land from satellite imagery [21]. Han et al. detected the cropping area in the middle of Heihe River Basin based on SVM using multitemporal vegetation index data [22]. Compared to other classifiers, SVM-based classifiers are built on statistical learning theory which classify objects through the maximal margin hyperplane established from very limited input features called support vector [23]. A few studies have shown that in most cases, SVM was less sensitive to the training samples and the performance was better than other classifiers with the same number of training samples [24]. Therefore, SVM is often preferred for classification purposes when only very limited truth samples are available. The objective of this study is to verify the feasibility of mapping FD canopies from remotely sensed images acquired by a customized UAV imaging system and to test the effectiveness of a proposed image classifier, a hierarchical classification schema powered by SVM, to extract FD from the remotely sensed imagery.

The objective of this study is to verify the feasibility of mapping FD canopies from remotely sensed images acquired by a customized UAV imaging system and to test the effectiveness of a proposed image classifier, a hierarchical classification schema powered by SVM, to extract FD from the remotely sensed imagery.

## 2. Study Site

As the main habitat of FD, Danxia Mountain (located at 113°36'E, 24°51'N), Shaoguan City, Guangdong Province, China, was being studied (Figure 1). The total area of Danxia Mountain was around 200 km<sup>2</sup>. The climate was characterized as subtropical monsoon, with an annual mean temperature of 19.7°C and annual precipitation of 1715 mm. The land surface was mainly covered by bare stones, conglomerates, and red soil. Dominant families of the flora included *Osteomeles subrotunda*, *Trichophorum subcapitatum*, *Engelhardtia chrysolepis*, *Lithocarpa uvariifolia*, *Acer oblongum*, *Helieia kwangtungensis*, resurrection plant, and *Firmiana danxiaensis* (FD). FD is a rare and endangered plant in China, and thus, protecting the plant species has become a significant task for both botanists and local governments.

FD mainly grows in shallow soil in Danxia Mountain (Figure 2). In fact, FD is the only tree species dominant in Mt. Danxia and was listed as a threatened species in China Species Red List [25]. Some characteristics about the species are listed in Table 1. The morphological form of FD canopies varies in shape, which makes them difficult to be extracted from other plant species purely through remote sensing images. FD reaches mature growing status during summertime which is also the season that an FD plant develops into its typical shape. Local governments as well as botanists are eager to map the spatial distribution of FD canopies and

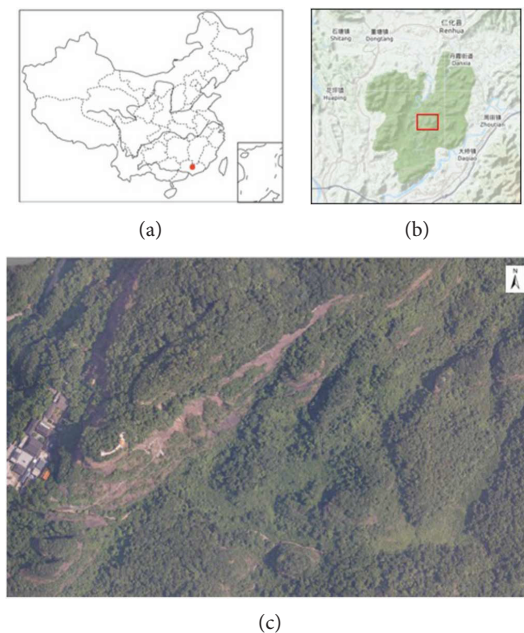


FIGURE 1: Study region. (a) Location of Danxia Mountain in the country, (b) outline of the study site, and (c) the experiment site.

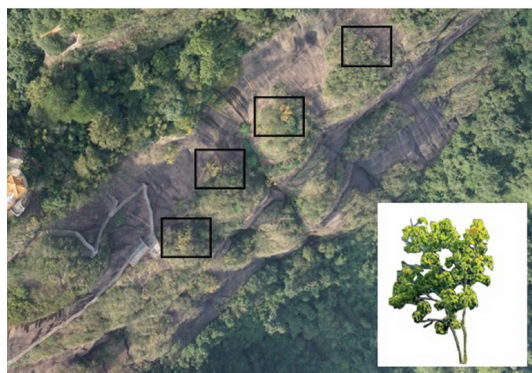


FIGURE 2: Examples of FD distribution. The black squares denote a few examples of FD locations, and the typical canopy structure of the plant is illustrated in the inset figure.

TABLE 1: Physical descriptions of FD.

Characteristics	Description
Category	<i>Arbor</i>
Height	3 m–8 m
Canopy area	12.5–30 m <sup>2</sup>
Blade shape (outline)	Mostly ellipse but with variations
Blade color	Turquoise

may design policies to protect the plant. But accurate positioning of the plant species is so far hard to obtain. The ground survey serves as a traditional method to map FD distribution but was limited due to the steep terrain, which makes some data impossible to be collected [26]. Therefore, alternative methods having more efficiency were desired. Satellite remote sensing could be too coarse to detect FD due to its small crowns, and plant texture information in

imagery could not be captured, resulting in unsatisfactory extraction results of FD detection. Instead, data acquisition with UAVs could solve the issue because of the high-spatial resolution of UAV-collected images. However, considering the large area of the mountain (200 km<sup>2</sup>), a typical experiment site with a small area (3 km × 4 km) was decided as a testing project before conducting wide-scale FD mapping by an UAV platform in this study.

### 3. Materials and Methods

#### 3.1. Customized Multispectral Imaging System

3.1.1. *Ground Spectra Collection and Selection of Spectral Bands.* As a preliminary step, we distinguished the spectra among the plant species by acquiring on-site spectral signals of each plant species and the bare ground (denoted as Ground, hereafter) where there is no vegetation/plant covered. The on-site spectral signals were collected on July 11, 2016, using a field spectrometer (Avafield-2). This spectrometer recorded the spectral signals at wavelengths ranging from 350 nm to 1000 nm. The field of view was 25°. At each measuring unit, the signal of the reference panel was collected first for calibration. The reference panel was a sulfate plate with approximately 98% reflectance with the diameter size of 20 cm. The probe was put vertically down with the distance to the samples about 1 m. In order to avoid accidental error, each observation was repeated for five times. The averaged reflectance curves for each ground features were shown in Figure 3. Preliminary analysis indicated that Ground could be easily excluded by the signals in the near-infrared region. Four plant species, which was termed as high-spectral dissimilarity classes (HSD-classes hereafter), including *Osteomeles surotunda*, *Engelhardtia chrysolepis*, *Trichophorum subcapitatum*, and *Helieia kwangtungensis*, seem to have significant dissimilarity

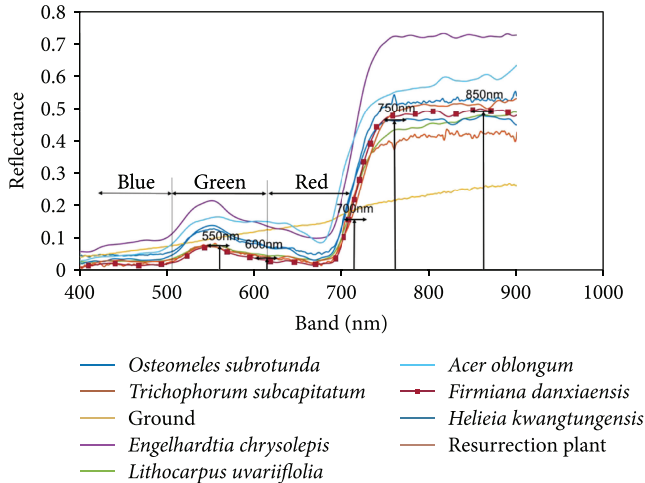


FIGURE 3: Mean spectral reflectance from field-collected spectra for eight vegetation species and the bare ground.

in spectra from the rest of the other four species. Therefore, it is possible to separate the HSD-classes and Ground from the other species using purely spectra information. The left four species, which was termed as low spectral dissimilarity class (LSD-classes hereafter), are difficult to be separated based on the spectra only. Thus, other geometric or texture information must be considered in the design of the classification schema.

**3.1.2. Customized Multispectral Imaging System.** Based on the analysis of the spectral signatures collected on-site as well as general knowledge of the spectral responses from green vegetation, a customized multispectral imaging system was designed for our study objective. The designed imaging system captured eight spectral bands, including three wide channels (by RGB camera) and five multispectral channels, as shown in Figure 4. Standard deviation (std) of reflectance for the selected wavelengths were calculated, resulting in 0.0623, 0.0512, 0.0838, 0.1881, and 0.1965 for 550 nm, 600 nm, 700 nm, 750 nm, and 850 nm, respectively. The imaging system was simplified by looking for suitable commercial cameras on the market. In the end, the camera Sony A 6000 was used directly for capturing the RGB channels. For the five multispectral bands, Sony A 6000 worked great after they were combined with specific band-pass filters, which realized the capturing signal channel at particular wavelengths. The main characteristics of the designed imaging system were shown in Table 2. The transmittance of the filter was 95%. Bandwidth FWHM (full width at half maximum) was 10 nm. The imaging system acquired six bands simultaneously with one exposure, and the time interval was 4 s. The spatial resolution was 12 cm when the flight height was set at 1000 m.

### 3.2. Remote Sensing Data Acquisition and Preprocessing

**3.2.1. Imaging Data Acquisition.** Image acquisition was carried out on July 14, 2016, a sunny day, using the customized imaging system mounted on an UAV platform. A ground control station software was used (Mission Planner, [http://](http://ardupilot.org/planner)

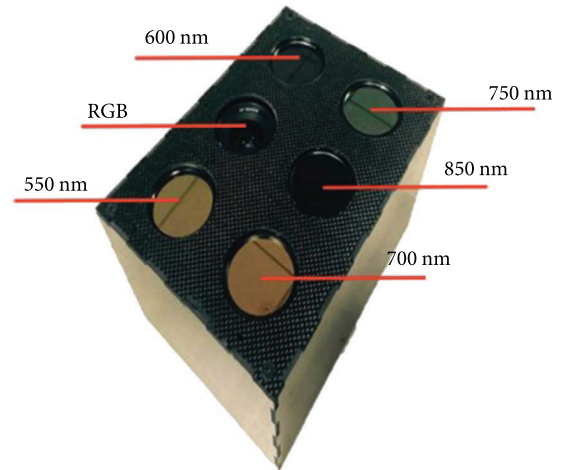


FIGURE 4: The customized imaging system with multispectral and RGB channels.

TABLE 2: Characteristics of the designed imaging system.

Parameters	Value
Bandwidth FWHM	10 nm
Exposure interval	4 s
Filter transmittance	95%
Frame image size	4000 × 6000
GND resolution (1000 m alt.)	12 cm

ardupilot.org/planner) to plan and control the flight. A route planning was designed based on the land terrain in order to balance the efficiency of data acquisition and the requirement of the overlapped area for building a fully qualified image dataset. In the end, images were acquired in a continuous mode for the whole experiment site (an area of about 10 km<sup>2</sup>), resulting in 50% side overlap and 70% forward overlap at the altitude of 1000 m. The total number of exposures was 721 times. Each exposure produced eight images (including three RGB channels and 5 multispectral channels) which were saved in tiff format.

**3.2.2. Image Data Preprocessing.** Geometric distortion influenced mapping accuracy and must be diminished. Calibration on the digital numbers to radiance was necessary to extract the spectral reflectance from the plants and the ground. Further, calibrated images were used to generate a mosaicked orthoimage and a DSM map. Overall, the image preprocessing included three steps, optical calibration, radiometric calibration and matching, and image mosaicking.

Optical calibration processing included geometric calibration and removal of vignetting. Geometric calibration determined the lens distortion parameters and principal points of the imaging system. The coefficients of lens distortion included radial and tangential distortions. Radial distortion was the curving effect due to the subtle radial shift. The distortion brought the pincushion effect in value position. Tangential distortion affected a planar shift in the perspective of the image due to the nonalignment of the lens [27]. The calibration toolbox in Matlab was used for geometric

calibration [28]. The calibration of vignetting used a look-up table which recorded the vignetting parameters obtained in the laboratory on a per-pixel basis.

Radiometric processing was used to transform DNs (digital numbers) to radiance (Rad) for each image band. Laboratory calibration and empirical line method were adopted to determine the quantum efficiency function and to calculate the necessary parameters [29]. Quantum efficiency defined the fraction of photon flux that contributes to the photocurrent in a photodetector or a pixel. The relationship between DNs and Rad can be expressed in

$$\text{DN} = \text{Rad} \times \text{QE}_{\text{band}}, \quad (1)$$

where DN is the gray value at a pixel in an image and Rad is the radiance value of the pixel.  $\text{QE}_{\text{band}}$  is the quantum efficiency of an imaging system. In our study, laboratory calibration was used to derive  $\text{QE}_{\text{band}}$ . The experiment determined the parameters on a per-pixel basis by establishing a function between the luminance of standard light source with known radiance and DN of the imaging system.  $\text{QE}_{\text{band}}$  was then used to transform DNs to radiance values.

RGB and multispectral images and point clouds were generated from the calibrated images using Pix4D software [30]. Those calibrated images had enough overlapped regions. Orthoimages were computed based on the RGB and multispectral channels separately and clipped to make a stacked image which covered the study area. The vegetation indices, as listed in Table 3, were derived from the stacked image. The DSM was generated from the point clouds by inverse distance weighing [31] and smoothed by a 5-by-5-pixel averaging filter.

**3.3. Canopy Segmentation for UAV Imagery.** Image segmentation is a fundamental task of image processing that partitions the image by grouping pixels into homogeneous regions or patches. Object-based image segmentation proved to be useful for complicated images [32]. To do so, it is necessary to design a combined homogeneity index (referred to as  $H$ ) based on which the variance of the index presented in each patch can be evaluated. In this study, the geometry, texture, and spectral features of different plant species appearing in the acquired imagery were fully considered. Given a patch that consists of a set of image pixels,  $H$  is an index that comprehensively reflects the homogeneity of the patch. A bottom up region-merging algorithm was adopted to realize image segmentation. Region merging starts from a single pixel and looks for its surrounding pixels that must satisfy  $H$  index if they are merged. The criterion for object merging is to minimize  $H$  index. In each step, adjacent objects are selected based on the smallest growth of the heterogeneity. A predefined parameter,  $H_A$ , is given based on a trial-and-error test. If the heterogeneity is higher than  $H_A$ , the merging process will stop.  $H$  is defined as [33]

$$H = w_{\text{sp}} \times \Delta h_{\text{sp}} + w_{\text{sh}} \times \Delta h_{\text{sh}}, \quad (2)$$

where  $w_{\text{sp}}$  and  $w_{\text{sh}}$  are the weights of the spectral index and shape index and the sum of  $w_{\text{sp}}$  and  $w_{\text{sh}}$  is 1,  $\Delta h_{\text{sp}}$  is a spectral index which captures the spectra characteristics, and  $\Delta h_{\text{sh}}$  is a

shape index reflecting the shape characteristics of a merged object. Spectral feature was defined by weighing each channel number of candidate objects  $n_{\text{merge}}$  and standard deviation  $\sigma$ . Shape feature was determined by compactness feature, smooth feature, and the ratio of them. The given object denoted as obj1 and another object denoted as obj2 to be merged to obj1,  $\Delta h_{\text{sp}}$ , and  $\Delta h_{\text{sh}}$  were calculated by (3) and (4):

$$\Delta h_{\text{sp}} = \sum_{i=1}^N w_i \left( n_{\text{merge}} \sigma_i^{\text{merge}} - \left( n_{\text{obj1}} \sigma_i^{\text{obj1}} - n_{\text{obj2}} \sigma_i^{\text{obj2}} \right) \right), \quad (3)$$

where  $N$  is the number of layers (bands) that participated in segmentation and  $w_i$  is the weight assigned to band  $i$  to represent its importance ( $\sum_{i=1}^N w_i = 1$ ),  $n_{\text{merge}}$  is the total number of pixels in the merged object,  $\sigma_i^x$  is standard deviation of spectra for pixels contained in an object ( $x$  is obj1, obj2, or the merged object), and  $n_{\text{obj1}}$  and  $n_{\text{obj2}}$  are the number of pixels in obj1 and obj2, respectively, before they are merged.  $\Delta h_{\text{sp}}$  indicates the dissimilarity of obj1 and obj2 from the spectral perspective.

$$\Delta h_{\text{sh}} = w_{\text{comp}} \cdot \Delta h_{\text{comp}} + w_{\text{sm}} \cdot \Delta h_{\text{sm}}. \quad (4)$$

In (4),  $\Delta h_{\text{comp}}$  and  $\Delta h_{\text{sm}}$  were the index of the shape compactness and smoothness defined by (5) and (6), respectively.

$$\Delta h_{\text{comp}} = n_{\text{merge}} \cdot \frac{l_{\text{merge}}}{\sqrt{n_{\text{merge}}}} - \left( n_{\text{obj1}} \cdot \frac{l_{\text{merge}}}{\sqrt{n_{\text{merge}}}} \right), \quad (5)$$

$$\Delta h_{\text{sm}} = n_{\text{merge}} \cdot \frac{l_{\text{merge}}}{b_{\text{merge}}} - \left( n_{\text{obj1}} \cdot \frac{l_{\text{obj1}}}{b_{\text{obj1}}} + n_{\text{obj2}} \cdot \frac{l_{\text{obj2}}}{b_{\text{obj2}}} \right). \quad (6)$$

In (5) and (6),  $l_x$  and  $b_x$  represent the perimeter and the bounding box of object  $x$  ( $x = \text{obj1}, \text{obj2},$  or the merged object) and the other parameters are the same as in (3).

In this study, we used eCognition Developer (Trimble, 2015) to segment the processed image for the study area. The eight bands (RGB bands and multispectral bands) were involved and equally weighted ( $w_i = 1/8, i = 1, 2, \dots, 8$ ). A weight of 0.6 was given to the compactness weight ( $w_{\text{comp}}$ ) and 0.4 was given to the smoothness ( $w_{\text{sm}}$ ), considering that compactness before merging should be given more priority. An equal weight was given to the shape parameter ( $w_{\text{sh}}$ ) and the spectral parameter ( $w_{\text{sp}}$ ). One difficulty then was to decide the threshold ( $H_A$ ) based on which the merging process could be stopped if the calculated  $H$  index was greater than the threshold. High  $H_A$  would result in larger size of patches which could include more than one plant species in the patches. Conversely, too small  $H_A$  might result in a single FD crown separated into several patches. Therefore, the determination of the threshold was realized by a trial-and-error strategy by setting a range of  $H_A$  and the one that segmented the area into patches making most FD located in a single patch, judged from field trothing data, was taken as the result. In the end,  $H_A$  was given to 35, which seemed

TABLE 3: Three vegetation indices used in the study.

Vegetation index	Equation
Normalized difference vegetation index (NDVI)	$(R_{850\text{nm}} - R_R)/(R_{850\text{nm}} + R_R)$
Structurally insensitive pigment index (SIPI)	$(R_{850\text{nm}} - R_B)/(R_{850\text{nm}} + R_B)$
Red edge normalized difference vegetation index (RENDVI)	$(R_{750\text{nm}} - R_R)/(R_{750\text{nm}} + R_R)$
Photochemical reflectance index (PRI)	$(R_G - R_{600\text{nm}})/(R_G + R_{600\text{nm}})$

appropriate in terms of FD grouping which appeared in the segmented patches.

**3.4. Design of Image Classification Schema.** In order to classify the canopy of FD, a hierarchical classification method, for discriminating nine classes (including Ground), was decided and established based on the analysis of the spectral characteristics of the targeted plant species as well as the typical morphological form of FD canopies. The hierarchical classification method simplified the classification process into three levels. Each level allowed using specific algorithm and rules to classify the desired classes. The flowchart of classification strategy was shown in Figure 5. At the first level, segmented objects (patches) were classified into Ground and non-Ground (vegetation) objects, which was implemented after computing vegetation indices (VIs), indicators of the green density, from remote sensing images. VIs have also been used to separate vegetation species in many other studies [34]. Out of the VIs, normalized difference vegetation index (NDVI) is probably the most popular one which is calculated by comparing the magnitude of spectral reflectance at wavelengths red and near infrared, given by [35]

$$\frac{R_{850\text{nm}} - R_R}{R_{850\text{nm}} + R_R}, \quad (7)$$

where  $R_{850\text{nm}}$  is the reflectance at wavelength 850 nm and  $R_R$  is the reflectance at wavelength 705 nm or of the red channel in a RGB image.

In addition to NDVI, there are other vegetation indices (VIs) which were proposed for the similar purpose (Table 3). Those VIs were formulated by taking the characteristics of spectral reflectance of green vegetation from different aspects. For example, the spectral reflectance of vegetation usually presents a green peak located at wavelength 550 nm in the spectrum and strong spectral absorption in the blue and red regions of the spectrum. Furthermore, the red edge effect from vegetation is typically observed for vegetation reflectance in that a rapid increase of reflectance occurs starting at the red region (around 700 nm in the spectrum) to the near-infrared region (usually at 750 nm or 850 nm). Those information provided the basis for designing the spectral channels of our customized multi-spectral imaging system on UAVs.

A simple filter based on the processed VIs was applied to exclude ground patches. At level 2, plant species were classified as four HSD-classes and an LSD-class. The HSD-classes included four plant species, namely, *Osteomeles surotunda*, *Engelhardtia chrysolepis*, *Trichophorum subcapitatum*, and

*Helieiakwangtungensis*. The left plant species, including FD, were assigned as a combined LSD-class which could not be separated by purely spectral information due to low dissimilarity in spectra. At this level, SVM was used to classify the 5 classes (four HSD-classes and a combined LSD-class) using the spectral features (the eight bands and vegetation indices) only. The mean spectra value and vegetation indices (NDVI, SIPI, RENDVI, and PRI, in Table 3) of all the pixels located within each patch were calculated and used in the SVM classifier. At level 3, the combined LSD-class was further divided into four plant species, including FD, based on the geometric feature, terrain feature, and texture features by another SVM classifier. Here, SVM, a nonparameter-supervised classifier, was chosen as the classifier for both levels 2 and 3 because it has advantage achieving good classification results without sensitivity to sample size [36].

Terrain properties, geometric properties, and texture characteristics were used at level 3 to identify patches covered by FD canopies. Terrain properties, including slope, aspect, and DSM, were input to the classifier because the FD was observed to appear mainly at medium terrain height and southern slope. Because we did not have DEM data with spatial resolution comparable to the processed images, a smoothed DSM was used to process slope and aspect data.

Texture and geometric information denoted the shape of the targeted patch. In this study, Gray-level Co-occurrence Matrix (GLCM) was used to represent texture [37]. Four GLCM indices were included in classification (Table 4). For geometric properties, three indices were formulated and used in the classifier (Table 4).

Standard radial Gaussian was used as the kernel function for the SVM classifier. The main parameters to be decided in the classifier included  $C$  (the penalty parameter which stands for an error term) and  $\gamma$  (controlling training efficiency). As there was no prior knowledge which  $C$  and  $\gamma$  were acceptable, they were determined based on a recursive loop with different combinations. During the process, a good pair of  $C$  and  $\gamma$  could be identified [38].

Field trip was arranged to collect ground truth data for model training and result validation. The date of ground data collection was conducted on July 21, 2016, one week after the UAV flight. A GPS device (Trimble R2 GNSS) was used to record the coordinate of FD trunk location, and the general shape for each recorded FD canopy was drafted. RTK (Real-Time Kinematic) was set as the operating mode, producing an absolute positioning accuracy within 1-2 cm. Two thirds of the recordings were used for model training purposes, and the rest were used for result validation. eCognition Developer was used to implement the

TABLE 4: The equation and description of index.

Type	Index	Equation and description of index
Texture <sup>#</sup>	GLCM_homogeneity	$\sum_{i=0}^I \sum_{j=0}^J P \frac{(i, j)}{(1 + (i - j)^2)}$
	GLCM_contrast	$\sum_{i=0}^I \sum_{j=0}^J P(i, j) \times (i - j)^2$
	GLCM_dissimilarity	$\sum_{i=0}^I \sum_{j=0}^J P(i, j) \times  i - j $
	GLCM_Entropy	$- \sum_{i=0}^I \sum_{j=0}^J P(i, j) \times \ln P(i, j)$
Geometry <sup>*</sup>	Shape index	$s = \frac{e}{4 \bullet \sqrt{A}}$
	Density	$d = \frac{\sqrt{n}}{1 + \sqrt{\text{Var}(X) + \text{Var}(Y)}}$

<sup>#</sup> $P_{i,j}$  is the probability of a gray level pair,  $i$  and  $j$ , in the GLCM defined by a position operator, and  $I$  and  $J$  are the maximum values given in each dimension of GLCM, respectively. <sup>\*</sup> $e$  and  $A$  were the perimeter and area, respectively, of the targeted patch,  $n$  was the number of pixels, and  $X$  and  $Y$  were the width and length of the bounding box of the patch.

hierarchical classification strategy. The segmented patches, a DSM layer, slope layer, and aspect layer participated in the classification process. Spectra, geometric, and texture indices were calculated during the classification process by customized functions.

## 4. Result

**4.1. UAV-Collected Imagery.** The orthoimage processed from the spectra collected by UAV sensors showed clear differentiation, in terms of spectral, texture, and geometry, in the distribution of different plant species and the bare ground (Figure 6). The DSM, ranging from 214 m to 302 m, showed the spatial variations of surface height. Such height reflects the changes over the space in both DEM and the plant species. When combined with other topography information such as the slope and aspect, better understanding of the preferred locations of each plant species could be analyzed. The acquired images from UAV allowed producing various vegetation indices which could be helpful data input for classifying the plant species and the ground. For example, red edge normalized difference vegetation index (RENDVI) processed from the multispectral band at 775 nm and red band of RGB showed clearly the differentiated patterns in the distribution of the bare ground and plant species. One advantage of applying UAV platform is that the high-spatial resolution of those images provided enough detail information for building advanced image classifiers, which otherwise is impossible for other satellite platforms.

**4.2. Classification Result of FD Canopy.** SVM, using radial Gaussian used as the kernel function, was used to classify HSD-classes and LSD-classes. At level 2,  $C$  and  $\gamma$  were determined as (5, 10) for the SVM classifier. At level 3,  $C$  and  $\gamma$

were determined as (2, 10) for the classifier. The different parameter settings allowed optimized classification result at different classification steps. The final classification result, denoted as FD species, non-FD species, and Ground, for the study site was shown in Figure 7(a).

The result indicated that the FD species only covered very small part of the area, which was in agreement with the reality. Though FD could spread over the whole study area, the spatial distribution of FD tended to cluster and was dominantly located close to the bare ground and the cliff (Figure 7(b)). This finding may serve as important clue for local botanists to evaluate the FD distribution.

**4.3. Accuracy Test.** The GPS recordings from the field trip were used to validate the classification result. Those points that were recorded as FD were overlaid on top of the classified segments (Figure 8). The locations of FD species generally matched well with the segments assigned to FD which, after merged with adjacent ones, had an area ranging from 10 m<sup>2</sup> to 32 m<sup>2</sup> (Figure 8(b)), comparable to the statistics of the canopy size from field samples (Table 1). Classification results by the proposed hierarchical classifier showed that the overall classification accuracy at levels 2 and 3 reached 87.4% and 75.3%, respectively (Table 5). For the SVM classifier at level 2, there were 17.6% cases from HSD-classes that were mistakenly assigned to LSD classes, though most LSD-classes were labeled correctly (accuracy = 92.4%). There were 331 cases classified as LSD-class, including 53 cases which were actually HSD-class. Out of the 52 FD samples in the testing set, 6 cases were wrongly mapped as HSD-class (Table 5(a)) and the remaining 46, along with randomly selected 51 non-FD samples, were entered into the next SVM classifier at level 3 for testing. The result indicated that the SVM classifier at level 3 performed slightly worse than that at level 2, mainly due to the fact that almost one-third of non-FD samples were wrongly classified as FD. The hierarchical classification powered by SVM classifier for FD species reached an overall accuracy of 76.9%, a reasonable result considering the complex terrain and multiple plant species.

## 5. Discussion

Remote sensing image acquisition by sensors mounted on UAV platforms has been widely used in the classification of forests [39]. There are several advantages by applying UAV-based remote sensing. Firstly, UAV platforms can fly at low-altitude and thus images having high-spatial resolution can be acquired. Low-altitude remote sensing decrease the distance between the target objects and the sensors and thus the quantity of acquired images is improved. Because of the high-spatial resolution, extracting FD from UAV images also has less impact from mixed pixel issue. Furthermore, the collected images are less affected by the atmosphere and luminous impact. Secondly, the flight route and flight height can be customized based on the actual need and thus UAV platforms provide more flexibility for data acquisition. Sensors mounted on UAVs can be used to map most places on the land surface, and setting an appropriate flight height can balance

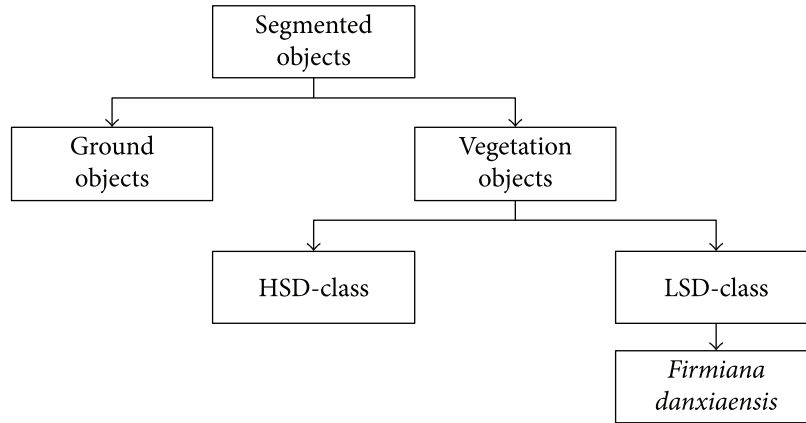


FIGURE 5: The flow chart of the classification strategy. The hierarchical classification strategy included three levels. At the last level (level 3), FD canopies were identified from the segmented objects.

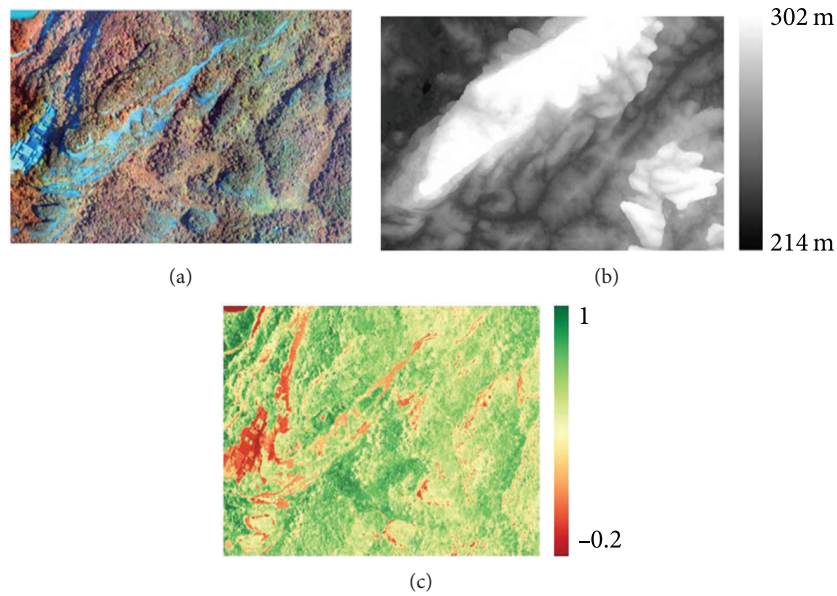


FIGURE 6: Example of data products computed from the spectra collected by the image system on UAVs. (a) Mosaicked orthoimage, (b) the smoothed DSM, and (c) NDVI index. One of the vegetation indices is used to distinguish vegetation area and soil area and to input to the SVM classifier at level 2 in the classification schema.

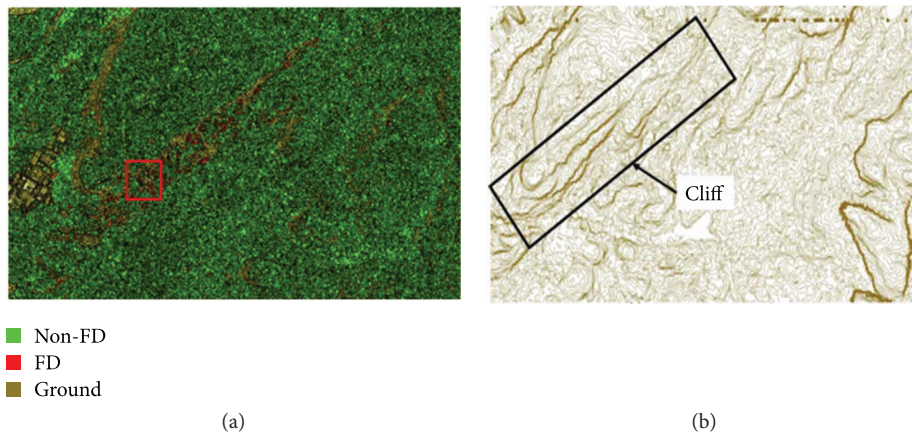


FIGURE 7: Classification result for the segmented patches of the image collected on an UAV platform. (a) Overall classification map for the study site. (b) The corresponding DSM contour line showing the cliff area (steep terrain) in the black rectangle where FD densely populated.

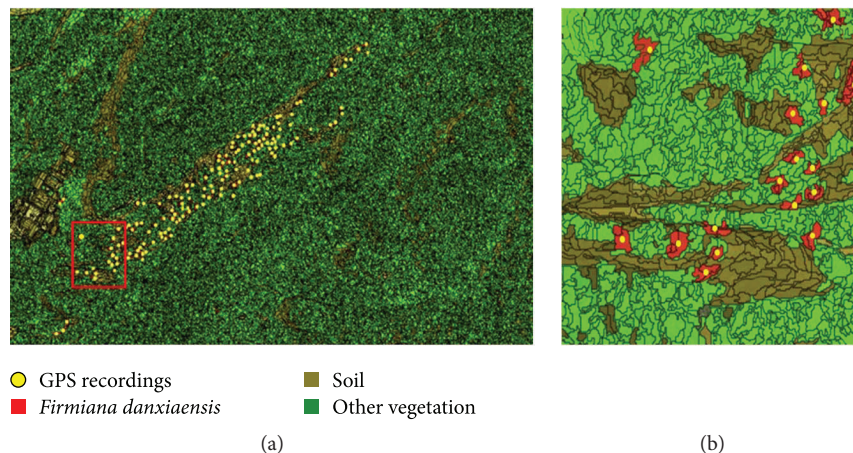


FIGURE 8: Validation of the classification result based on field trip. Yellow points are GPS recordings showing the FD locations. (a) Overall classification map overlaid by FD locations from GPS recordings and (b) detail of FD labeled segments/patches (in red) and the ground truth/GPS points (yellow dots).

TABLE 5: Accuracy assessment of the FD classification for the segmented patches.

(a) Confusion matrix at level 2

Reference class	Map class		Producer's accuracy
	HSD-class	LSD-class	
HSD-classes	248	53	82.4%
LSD-classes	23 (6*)	278	92.4%
User's accuracy	91.5%	84.0%	87.4%

\*Number of FD samples located in the cell. Kappa = 0.748.

(b) Confusion matrix at level 3

Reference class	Map class		Producer's accuracy
	FD	Non-FD	
FD	40	6	87.0%
Non-FD	18	33	64.7%
Accuracy	67.0%	84.7%	75.3%

Total number of FD: 52; number of FD correctly labeled: 40; accuracy for FD extraction: 76.9; Kappa = 0.535.

the coverage and spatial resolution of the acquired data; thus, the efficiency of data collection can be improved because the flight range can be determined as required. Thirdly, UAV platforms can support any cameras designed to collect images for particular spectral wavelengths. As the study conducted here, RGB channels and 5 multispectral channels were designed by using particular band-pass filters on the commonly commercial cameras. By collecting and analyzing the diversity of spectra, imaging systems can be customized to collect spectra based on the mapping purposes. However, unlike satellite remote sensing platforms which can cover a large area in one glance, UAVs are usually suitable for mapping small area only due to the limited viewing angles and relatively low flight height. Further, the demand for georegistering and mosaicing multiple images collected at adjacent flight routes also introduces extra input for remote sensing by

UAVs. Possible solutions may integrate UAV images with other imagery products from satellite remote sensing.

In our study, we proposed a hierarchical classification approach after the analysis of the spectral features of the plant species. Such strategy allowed us to separate different classes in a progressive manner and proved to be suitable for extracting FD from the acquired imagery. For example, the bare ground could be easily excluded based on the computed VIs simply by using threshold filters, namely, segmented patches with VIs lower than predefined thresholds were labeled as Ground. SVM has been proved effective in classifying remote sensing imagery when a limited number of samples are available [40]. Several studies have been using the hierarchical classification method and SVM algorithm to classify specific plants [41]. For example, SVM was used as a binary classifier to detect seminatural habitats [42]. The combination of a hierarchical classification schema and SVM algorithm has three main advantages. Firstly, the process for building such classification structure is readily available in several existing software packages such as eCognition and Matlab [43]. After necessary datasets, including the orthoimages, DSM, and segmented patches in this study, are ready, the classifier could be quickly setup with those input datasets. The main work of building the classifier involved establishment of the rules to label the input patches based on related data (e.g., DSM and the orthoimages in this work). The second advantage is that the classification schema can simplify the classification process. The hierarchical classification approach separates the candidate classes into several levels, and thus, the classification can be divided into a few subobjectives. When combined by appropriate algorithms at each level, improving the overall classification accuracy can be realized. Lastly, the hierarchical classification combined with SVM is efficient for extraction of a single class (e.g., FD in this study) from multiple class labels. The basic SVM classifier only supports binary classification issues, namely, 0-1 cases. SVM also supports classifying multiple classes called K-class classifier which split the process into k steps [44]. In the current study, SVM was applied to classify

LSD-class and non-LSD-class at level 2 and to classify FD and non-FD at level 3, both of which were binary classification, though there were multiple plant species involved. In fact, there was no need to classify the species within HSD-classes or to classify each species within the LSD-classes, considering the very specific objective of the study.

There are two steps which may introduce uncertainties in the ultimate classification result based on the proposed hierarchical classification schema; they are image segmentation and classification of segmented patches. First, detection of FD canopy is highly dependent on the result of image segmentation which was performed based on a bottom up region-merging algorithm in this study. A homogeneity index,  $H$ , was used to control the process of object merging. It is clear that the result of image classification depends on the criteria adopted for the  $H$  index. Factors involving the spectra and geometry of produced patches were considered in computing the index. The weight assignment for each of the factors is critically important. In addition, the threshold value ( $H_A$ ) in the study determined the process of segmentation: either continuing the merging process or stopping it. The factors and their weighing schema as well as the threshold all determine the size of the segmented patches. Though we used a trial-and-error strategy to determine  $H_A$ , we observed that there was still a small part of the patches (which were FD canopy tested by field GPS recordings) which were either too small or too big, resulting in mislabeling in the next hierarchical classification step by the SVM classifier. The next step, hierarchical classification for the segmented patches, also introduced certain uncertainties. There were three levels in the proposed hierarchical classification schema. We observed that there was very few mislabeled cases at the first level. However, the SVM classifiers at levels 2 and 3 did produce mislabeled patches, including cases that either non-FD patch was labeled as FD or FD patch was labeled otherwise. While SVM is regarded as an advanced classifier that has been successfully applied in many image classification studies [45], the data quality used to train the model and the data quality in the testing samples can surely have much impact on the result. Spectra as well as spectra-derived vegetation indices were taken as input in the SVM classifier at the second level. It was pointed out that mixed spectra in remote sensing imagery would inevitably lead to side effect on the classification result [46]. Still, though the study took terrain properties, geometric properties, and texture characteristics in the SVM classifier at the third level, certain confusion between FD and other plant species might also exist, making the wrong assignment of labels to some segmented patches. Terrain properties were probably the most important factors that should be taken to differentiate LSD-classes, as FD are distributed mainly close to cliff area where the slope index played a vital role in the classifier. Other factors related to geometry and texture could be examined and selected in more detail for the SVM classifier. Nevertheless, our work demonstrated the effectiveness of applying the designed object-based image segmentation and hierarchical classification schema in the extraction of FD canopy from remotely sensed images on the UAV platform.

## 6. Conclusion

Recent applications of UAVs make the equipment rapidly evolve into easy-to-use platforms for sensors deployable to acquire fine-scale vegetation data over large areas in a timely and cost-effective way. Customized imaging systems mounted on UAV platforms possess the capability and flexibility of collecting low-altitude remote sensing data for classifying land cover with plant species. In this work, we designed a customized imaging system mounted on UAV and acquired RGB and multispectral images covering part of Danxia Mountain where most of *Firmiana danxiaensis* (FD), a rare and endangered plant in China, are distributed. The identification of FD distribution has been desired by local practitioners as well as researchers in academia for a long time. However, large-scale FD mapping, based on traditional field survey, was called a halt due to the high cost and even safety issues associated with the work. With advances in remote sensing technology, especially UAV applications, this study tried to test the possibility of mapping FD through the customized imaging system mounted on an UAV platform. To this end, a limited number of field spectra collection were conducted first to help analyze the characteristic of FD and other plant species, which enabled the design of a reasonable hierarchical classification schema for the acquired UAV images. Various image products, including DSM and vegetation indices, were derived from the imaging system and involved in the classification process. Support vector machine was integrated to achieve good extraction of FD canopies from the UAV imagery. Spectra, terrain, geometric, and texture properties were fed into the proposed classifier so that the plant species could be separated. The accuracy of detection was evaluated by the ground truth GPS recordings. The study proved that UAV could be a promising platform to conduct FD surveying and mapping, which provides fundamental data to protect the rare plant species. Future work may focus on fusing UAV-based images with other products from satellite remote sensing so that the efficiency for mapping FD could be further improved.

## Data Availability

The data used to support the findings of this study are available from the corresponding author upon request.

## Conflicts of Interest

The authors declare that there is no conflict of interest regarding the publication of this paper.

## Acknowledgments

This research is funded by the National Natural Science Foundation of China (no. 41771481, no. 41671451, and no. 41701524), the Fundamental Research Funds for the Central Universities and China Postdoctoral Science Foundation (Grant no. 2017M621530), and Shanghai Municipal Commission of Economy and Informatization (no. JMRH-2018-1016). The authors thank Tongfan Surveying Engineering

and Technology Co. Ltd. and Aerospace ShuWei High Tech. Co. Ltd. for their help in data measurements.

## References

- [1] X. Chen and B. L. Li, "Spatial distribution of forest biome energetics in China," *Forestry*, vol. 78, no. 5, pp. 461–469, 2005.
- [2] C. Toth and G. Józków, "Remote sensing platforms and sensors: a survey," *ISPRS Journal of Photogrammetry and Remote Sensing*, vol. 115, pp. 22–36, 2016.
- [3] M. Fagan, R. DeFries, S. Sesnie et al., "Mapping species composition of forests and tree plantations in northeastern Costa Rica with an integration of hyperspectral and multitemporal Landsat imagery," *Remote Sensing*, vol. 7, no. 5, pp. 5660–5696, 2015.
- [4] S. Zaman and M. Kato, "Assessment of forest covers change in tropical moist deciduous forest in Thakurgaon, Bangladesh using ALOS data (multipurpose forest management)," *Journal of Forest Planning*, vol. 16, pp. 285–292, 2017.
- [5] Y. T. Mustafa and H. N. Habeeb, "Object based technique for delineating and mapping 15 tree species using VHR WorldView-2 imagery," in *Proceedings Volume 9239, Remote Sensing for Agriculture, Ecosystems, and Hydrology XVI, 92390G*, Amsterdam, Netherlands, October 2014.
- [6] M. Ozdogan, "A practical and automated approach to large area forest disturbance mapping with remote sensing," *PLoS One*, vol. 9, no. 4, article e78438, 2014.
- [7] I. Colomina and P. Molina, "Unmanned aerial systems for photogrammetry and remote sensing: a review," *ISPRS Journal of Photogrammetry and Remote Sensing*, vol. 92, pp. 79–97, 2014.
- [8] B. Lu, Y. He, and H. Liu, "Investigating species composition in a temperate grassland using unmanned aerial vehicle-acquired imagery," in *2016 4th International Workshop on Earth Observation and Remote Sensing Applications (EORSAA)*, pp. 107–111, Guangzhou, China, July 2016.
- [9] O. Nevalainen, E. Honkavaara, S. Tuominen et al., "Individual tree detection and classification with UAV-based photogrammetric point clouds and hyperspectral imaging," *Remote Sensing*, vol. 9, no. 3, p. 185, 2017.
- [10] R. Dunford, K. Michel, M. Gagnage, H. Piégay, and M. L. Trémelo, "Potential and constraints of unmanned aerial vehicle technology for the characterization of Mediterranean riparian forest," *International Journal of Remote Sensing*, vol. 30, no. 19, pp. 4915–4935, 2009.
- [11] D. J. Hill, C. Tarasoff, G. E. Whitworth, J. Baron, J. L. Bradshaw, and J. S. Church, "Utility of unmanned aerial vehicles for mapping invasive plant species: a case study on yellow flag iris (*Iris pseudacorus* L.)," *International Journal of Remote Sensing*, vol. 38, no. 8–10, pp. 1–23, 2017.
- [12] J. W. Karl, J. K. Gillan, N. N. Barger, J. E. Herrick, and M. C. Duniway, "Interpretation of high-resolution imagery for detecting vegetation cover composition change after fuels reduction treatments in woodlands," *Ecological Indicators*, vol. 45, pp. 570–578, 2014.
- [13] K. Lim, P. Treitz, M. Wulder, B. St-Onge, and M. Flood, "LiDAR remote sensing of forest structure," *Progress in Physical Geography: Earth and Environment*, vol. 27, no. 1, pp. 88–106, 2003.
- [14] M. Dalponte, L. Bruzzone, and D. Gianelle, "Fusion of hyperspectral and LIDAR remote sensing data for classification of complex forest areas," *IEEE Transactions on Geoscience and Remote Sensing*, vol. 46, no. 5, pp. 1416–1427, 2008.
- [15] J. Zhang, J. Hu, J. Lian, Z. Fan, X. Ouyang, and W. Ye, "Seeing the forest from drones: testing the potential of lightweight drones as a tool for long-term forest monitoring," *Biological Conservation*, vol. 198, pp. 60–69, 2016.
- [16] J. Albetis, S. Duthoit, F. Guttler et al., "Detection of *Flavescence dorée* grapevine disease using unmanned aerial vehicle (UAV) multispectral imagery," *Remote Sensing*, vol. 9, no. 4, p. 308, 2017.
- [17] R. Näsi, E. Honkavaara, P. Lyytikäinen-Saarenmaa et al., "Using UAV-based photogrammetry and hyperspectral imaging for mapping bark beetle damage at tree-level," *Remote Sensing*, vol. 7, no. 11, pp. 15467–15493, 2015.
- [18] S. F. Chen, M. W. Li, H. J. Jing et al., "De novo transcriptome assembly in *Firmiana danxiaensis*, a tree species endemic to the Danxia landform," *PLoS One*, vol. 10, no. 10, article e0139373, 2015.
- [19] A. Michez, H. Piégay, L. Jonathan, H. Claessens, and P. Lejeune, "Mapping of riparian invasive species with supervised classification of unmanned aerial system (UAS) imagery," *International Journal of Applied Earth Observation & Geoinformation*, vol. 44, pp. 88–94, 2016.
- [20] S.-K. Kwon, H.-S. Jung, W.-K. Baek, and D. Kim, "Classification of forest vertical structure in South Korea from aerial orthophoto and Lidar data using an artificial neural network," *Applied Sciences*, vol. 7, no. 10, p. 1046, 2017.
- [21] A. Frick, P. Steffenhagen, S. Zerbe, T. Timmermann, and K. Schulz, "Monitoring of the vegetation composition in rewetted peatland with iterative decision tree classification of satellite imagery," *Photogrammetrie - Fernerkundung - Geoinformation*, vol. 2011, no. 3, pp. 109–122, 2011.
- [22] H. Han, M. Ma, and X. Wang, "Classifying cropping area of middle Heihe River Basin in China using multitemporal normalized difference vegetation index data," *Journal of Applied Remote Sensing*, vol. 8, no. 1, article 083654, 2014.
- [23] G. M. Foody and A. Mathur, "Toward intelligent training of supervised image classifications: directing training data acquisition for SVM classification," *Remote Sensing of Environment*, vol. 93, no. 1–2, pp. 107–117, 2004.
- [24] G. Mountrakis, J. Im, and C. Ogole, "Support vector machines in remote sensing: a review," *ISPRS Journal of Photogrammetry & Remote Sensing*, vol. 66, no. 3, pp. 247–259, 2011.
- [25] S. Wang and Y. Xie, *China Species Red List*, vol. 1, Higher Education Press, Beijing, China, 2004.
- [26] J. Ouyang, H. Peng, X. Luo, Z. Chen, A. Zhang, and Y. Ma, "Environmental features of the micro-landforms of the spatial distribution of the national rare species of *Firmiana danxiaensis* on the Danxiashan Mountain," *Scientia Geographica Sinica*, vol. 37, no. 10, pp. 1585–1592, 2017.
- [27] J. Kelcey and A. Lucieer, "Sensor correction of a 6-band multispectral imaging sensor for UAV remote sensing," *Remote Sensing*, vol. 4, no. 5, pp. 1462–1493, 2012.
- [28] J. Y. Bouguet, "Camera Calibration Toolbox for Matlab," *High Speed Vision System & Object Tracking*, 2013, [http://www.vision.caltech.edu/bouguetj/calib\\_doc/index.html](http://www.vision.caltech.edu/bouguetj/calib_doc/index.html).
- [29] D. Olsen, C. Dou, X. Zhang, L. Hu, H. Kim, and E. Hildum, "Radiometric Calibration for AgCam," *Remote Sensing*, vol. 2, no. 2, pp. 464–477, 2010.

- [30] F. J. Mesas-Carrascosa, J. Torres-Sánchez, I. Clavero-Rumbao et al., "Assessing optimal flight parameters for generating accurate multispectral orthomosaics by UAV to support site-specific crop management," *Remote Sensing*, vol. 7, no. 10, pp. 12793–12814, 2015.
- [31] R. Buffat, T. Sarjakoski, M. Santos, and L. Sarjakoski, "Feature-aware surface interpolation of rooftops using low-density Lidar data for photovoltaic applications," in *Geospatial Data in a Changing World*, Lecture Notes in Geoinformation and Cartography, Springer, Cham, 2016.
- [32] V. Dey, Y. Zhang, and M. Zhong, "A review on image segmentation techniques with remote sensing perspective," *Pattern Recognition*, vol. 38, no. 9, pp. 1277–1294, 2010.
- [33] M. Baatz and A. Schäpe, "Multiresolution segmentation: an optimization approach for high quality multi-scale image segmentation," in *Angewandte Geographische Informations-Verarbeitung XII*, J. Strobl, T. Blaschke, and G. Griesbner, Eds., pp. 12–23, Wichmann Verlag, Karlsruhe, Germany, 2000.
- [34] R. M. Igamberdiev, R. Bill, H. Schubert, and B. Lennartz, "Analysis of cross-seasonal spectral response from kettle holes: application of remote sensing techniques for chlorophyll estimation," *Remote Sensing*, vol. 4, no. 11, pp. 3481–3500, 2012.
- [35] R. S. Defries and J. R. G. Townshend, "NDVI-derived land cover classifications at a global scale," *International Journal of Remote Sensing*, vol. 15, no. 17, pp. 3567–3586, 1994.
- [36] Z. Sha and Y. Bai, "Mapping grassland vegetation cover based on support vector machine and association rules," in *2013 Ninth International Conference on Natural Computation (ICNC)*, pp. 44–49, Shenyang, China, July 2014.
- [37] Q. Yu, P. Gong, N. Clinton, G. Biging, M. Kelly, and D. Schirokauer, "Object-based detailed vegetation classification with airborne high spatial resolution remote sensing imagery," *Photogrammetric Engineering & Remote Sensing*, vol. 72, no. 7, pp. 799–811, 2006.
- [38] D. Giveki, M. A. Soltanshahi, and G. A. Montazer, "A new image feature descriptor for content based image retrieval using scale invariant feature transform and local derivative pattern," *Optik - International Journal for Light and Electron Optics*, vol. 131, pp. 242–254, 2017.
- [39] Y. Yuan and X. Hu, "Random forest and objected-based classification for forest pest extraction from Uav aerial imagery," in *ISPRS - International Archives of the Photogrammetry, Remote Sensing and Spatial Information Sciences, XLI-B1*, pp. 1093–1098, Prague, Czech Republic, July 2016.
- [40] L. Bruzzone, M. Chi, and M. Marconcini, "A novel transductive SVM for semisupervised classification of remote-sensing images," *IEEE Transactions on Geoscience and Remote Sensing*, vol. 44, no. 11, pp. 3363–3373, 2006.
- [41] B. Lu and Y. He, "Species classification using unmanned aerial vehicle (UAV)-acquired high spatial resolution imagery in a heterogeneous grassland," *ISPRS Journal of Photogrammetry and Remote Sensing*, vol. 128, pp. 73–85, 2017.
- [42] C. Schuster, T. Schmidt, C. Conrad, B. Kleinschmit, and M. Förster, "Grassland habitat mapping by intra-annual time series analysis – comparison of RapidEye and TerraSAR-X satellite data," *International Journal of Applied Earth Observation and Geoinformation*, vol. 34, no. 34, pp. 25–34, 2015.
- [43] M. J. Huang, *Development of Knowledge-based Classification System: Urban-feature Extraction Using Aerial Imagery with Airborne LiDAR Data*, VDM Verlag Dr. Müller, 2009, <http://www.vdm-verlag.de>.
- [44] Z. Li, S. Tang, and S. Yan, "Multi-class SVM classifier based on pairwise coupling," in *Pattern Recognition with Support Vector Machines*, vol. 2388pp. 321–333, Springer, Berlin, Heidelberg.
- [45] P. Du, J. Xia, W. Zhang, K. Tan, Y. Liu, and S. Liu, "Multiple classifier system for remote sensing image classification: a review," *Sensors*, vol. 12, no. 4, pp. 4764–4792, 2012.
- [46] C. Hecker, M. van der Meijde, H. van der Werff, and F. D. van der Meer, "Assessing the influence of reference spectra on synthetic SAM classification results," *IEEE Transactions on Geoscience and Remote Sensing*, vol. 46, no. 12, pp. 4162–4172, 2008.

## Research Article

# A Research on the Combination Strategies of Multiple Features for Hyperspectral Remote Sensing Image Classification

Yuntao Ma,<sup>1</sup> Ruren Li<sup>1</sup> ,<sup>1</sup> Guang Yang,<sup>2</sup> Lishuang Sun,<sup>1</sup> and Jingli Wang<sup>1</sup>

<sup>1</sup>School of Transportation Engineering, Shenyang Jianzhu University, Shenyang 110168, China

<sup>2</sup>School of Geography, South China Normal University, Guangzhou 510631, China

Correspondence should be addressed to Ruren Li; [rurenli@163.com](mailto:rurenli@163.com)

Received 30 December 2017; Accepted 4 April 2018; Published 13 May 2018

Academic Editor: Yichun Xie

Copyright © 2018 Yuntao Ma et al. This is an open access article distributed under the Creative Commons Attribution License, which permits unrestricted use, distribution, and reproduction in any medium, provided the original work is properly cited.

It has been common to employ multiple features in the identification of the images acquired by hyperspectral remote sensing sensors, since more features give more information and have complementary properties. Few studies have discussed the combination strategies of multiple feature groups. This study made a systematic research on this problem. We extracted different groups of features from the initial hyperspectral images and tried different combination scenarios. We integrated spectral features with different textural features and employed different dimensionality reduction algorithms. Experimental results on three widely used hyperspectral remote sensing images suggested that “dimensionality reduction before combination” performed better especially when textural features performed well. The study further compared different combination frameworks of multiple feature groups, including direct combination, manifold learning, and multiple kernel method. The experimental results demonstrated the effectiveness of direct combination with an autoweight calculation.

## 1. Introduction

The analysis of hyperspectral images has been more and more discussed in recent years. In the classification problem, it has been widely accepted that features from different views help to better recognize objects. It is common to extract multiple features before the classification procedure. Therefore, researchers have made great efforts in several aspects. First, for a long time, people have been striving to extract desirable and suitable features from hyperspectral remote sensing images for better representation [1–6]. It has been recognized that linear features are less effective than nonlinear features [7], while it reduces efficiency to obtain nonlinear features in many cases. Some efforts have been made to combine both features simultaneously [8]; second, more recently, many researchers have successfully designed different frameworks [9–12] to organize different types of features, like texture features, shape features, and spectral features, because the views from different feature spaces have particular statistical

properties [13]. Finally, great efforts have been made in the classification process. Classifiers based on kernels [14] have dealt well with the Hughes phenomenon [15]. It has led to a trend towards multiple kernel learning (MKL) [16–18], in which different groups of features have different kernel matrices and finally a composite kernel is yielded.

In general, the above approaches combine features extracted from peculiar bands or features (e.g., top principal component) with the initial hyperspectral bands and then put different groups of features into dimensionality reduction (DR) frameworks or classifiers [19, 20]. However, complementary properties of multiple features have not been widely considered or analyzed. Few approaches have taken global features which can be transformed or converted from the complete hyperspectral bands as a group of input features. More frequently, approaches like principal component analysis (PCA) [21], linear discriminant analysis (LDA) [22], isometric feature mapping (ISOMAP) [23], and Laplacian eigenmaps (LE) [24] have been only exploited as global

dimensional reduction techniques. The low-dimensional output features have reduced the contribution of each group of features [9, 10].

In this paper, we first made a systematic research on two schemes for hyperspectral image classification based on multiple features by utilizing different DR tools (linear and nonlinear) and different types of features. One scheme was combining spectral features with other features before the DR process; the other was reducing the dimensionality of the original hyperspectral features before combining with other extracted features. Based on the experimental results on three hyperspectral datasets, we suggested that alternative decisions should be made in different circumstances. Based on the research, we further compared different combination frameworks in hyperspectral remote sensing image classification. We selected complementary features including linear and nonlinear global features (in this paper, we take features converted from all the bands as “global features”) and two kinds of textural features (extracted from certain bands or layers). Three combination frameworks were tested on three frequently used hyperspectral datasets, which comprised two scenes collected by airborne visible/infrared imaging spectrometer (AVIRIS) over the Indian Pine region and Salinas valley, and one scene collected by the reflective optics spectrographic imaging system (ROSIS) over Pavia University.

The remainder of the paper is organized as follows. Section 2 provides the details about the source of three hyperspectral remote sensing datasets employed in the experiments and the process of the proposed method. Then, the experimental results are reported in detail in Section 3, including the comparison of two classification schemes based on multiple features and the test of the combination frameworks with the results both in accuracy and visual perspectives. Discussions based on the classification results are also included in this section. Finally, a general summary of the paper is represented in Section 4.

## 2. Methodology

### 2.1. Multiple Feature Extraction

*2.1.1. Dimensionality Reduction of Spectral Features.* In this paper, we consider features achieved from all the spectral bands as global features (GF). Generally, GF are divided into two categories. One is linear features, which commonly derive the information from the original spectral image bands by multiplying a transformation matrix. Among them, PCA is a conventional linear transition without class label information and has quite high time efficiency; the other is nonlinear features including manifold learning features and kernel features [25, 26]. More and more investigators have focused on absorbing or exploiting nonlinear features in the classification problems because linear features do not take into account the underlying nonlinear class boundaries [27]. However, linear and nonlinear global features are rarely combined in previous studies and the complementary properties of two types of features have not been widely discussed.

Representative manifold learning algorithms for DR comprise locally linear embedding (LLE) [28], ISOMAP,

Laplacian eigenmaps (LE), and local tangent space alignment (LTSA) [29]. This paper extracts ISOMAP and LE features from the hyperspectral datasets.

*2.1.2. Textural Feature Extraction.* In this paper, we take textural features derived from certain spectral bands or features as TF (textural feature). Many approaches have supplemented TF to spectral features because they complement features from different perspectives and give some detailed information. Two frequently used textural features are exploited in the scheme, including filter-based Gabor features and statistical GLCM features.

(1) *2D Gabor Textural Feature.* We consider the procedure in [30]; a Gabor function is defined as

$$\Psi_{s,d}(x, y) = \Psi_{\bar{\mathbf{k}}}(\bar{\mathbf{x}}) = \frac{\|\bar{\mathbf{k}}\|}{\delta^2} \cdot \exp\left(-\frac{\|\bar{\mathbf{k}}\|^2 \cdot \|\bar{\mathbf{x}}\|^2}{2\delta^2}\right) \cdot \left[ \exp(i\bar{\mathbf{k}}\bar{\mathbf{x}}) - \exp\left(-\frac{\delta^2}{2}\right) \right], \quad (1)$$

where  $\bar{\mathbf{x}} = (x, y)$  is the image location in spatial domain and frequency vector  $\bar{\mathbf{k}}$  determines the scales and directions of Gabor functions. It is defined as

$$\bar{\mathbf{k}} = \frac{\pi}{2f^s} \cdot \exp\left(i \cdot \left(\frac{\pi d}{8}\right)\right). \quad (2)$$

In our experiment, parameter  $f$  is fixed to 2. The scale parameter  $s$  ranges from 0 to 3, and the direction parameter  $d$  ranges from 0 to 7, which stands for 4 scales and 8 directions.  $s$  and  $d$  are both integers. Parameter  $\delta$  is fixed to  $2\pi$  which represents the number of oscillations under the Gaussian envelope. According to [10], the textural images derived from Gabor filters are the real part of convolving the image  $I(x, y)$  with different  $s$  and  $d$ .

$$F_{s,d}(x, y) = G_{s,d}(x, y) * I(x, y). \quad (3)$$

(2) *GLCM Textural Feature.* The gray-level cooccurrence matrix (GLCM) [31] textural feature is a widely used statistical feature. Given a certain distance and a direction, a gray-level cooccurrence matrix is built by calculating the probability of the occurrence of two gray levels from a pixel. Various features can be obtained from GLCM, and we extract 8 features for the combination in the experiment, including mean value, variance, homogeneity, contrast, dissimilarity, entropy, second moment, and correlation (details of calculation process can be found in [31]). In the experiment, the grayscale quantization level is fixed to 64 and the preprocess window is  $3 \times 3$ .

### 2.2. Combination Scenarios

*2.2.1. Weight Estimation by Average Distance Measurement.* Different types of features make different contributions to various classification problems. The paper automatically estimates the weights of different feature groups based on the

average distance measurement in Euclidean space. The procedure is as follows:

- (1) Concatenate and normalize different groups of features.
- (2) Calculate the mean values and variances of all classes for each feature from the sample set and compute the standardized distances between each two classes for each feature. The standardized distance is calculated as follows:

$$d = \frac{\mu_s - \mu_t}{\sigma_s + \sigma_t}, \quad (4)$$

where  $d$  is the standardized distance for each feature,  $\mu_s$  and  $\mu_t$  represent the mean values of class  $s$  and class  $t$ , and  $\sigma_s$  and  $\sigma_t$  represent the standard deviation of class  $s$  and class  $t$ . According to the standardized distances, if a couple of selected features give rise to the smallest distance within classes and the biggest distance between classes, the best classification result is likely to be yielded. Next, we extend the method to fit multiple classes and multiple features.

- (3) Calculate the sum of the standardized distances between each two classes for each feature and allocate the weight multipliers for different feature groups: the expression of a sample is defined as  $X = [x_{i1}, x_{i2}, \dots, x_{iL(i)}]_{i=1}^n$ , in which  $L(i)$  is the number of the  $i$ th group of features and  $n$  is the number of feature groups ( $n = 4$ ; PC, LE or ISOMAP, Gabor, and GLCM). We define  $w_i$  as the weight multiplier of the  $i$ th group.  $w_i$  can be calculated by

$$w_i = \frac{\sum_{k=1}^{L(i)} d_k^i / L(i)}{\sum_{i=1}^n \sum_{k=1}^{L(i)} d_k^i / \sum_{i=1}^n L(i)}, \quad (5)$$

in which

$$d_k^i = \frac{\sum_{p=1}^l \sum_{q=p}^l d_{pqk}^i}{l(l-1)/2}, \quad (6)$$

where  $d_{pqk}^i$  is the average standardized distance of the  $k$ th feature in the  $i$ th group between classes  $p$  and  $q$  (4) and  $l$  is the number of all the classes.

- (4) Renew the representation of the sample  $X = [w_i x_{i1}, w_i x_{i2}, \dots, w_i x_{iL(i)}]_{i=1}^n$ .

The advantages of the weight estimation method are as follows:

- (i) Each type of features has its own weights, which maintains the specific properties of different features.
- (ii) The weight multipliers are around 1, so the method does not influence much on the normalized values of the features.

- (iii) The method has high time efficiency without iterative procedure.

**2.2.2. Combination and Classification.** As discussed before, we have got several global features and two kinds of textural features. For GF, we select the first 10 PC, 10 ISOMAP features, and 10 LE features, while for TF, 32 Gabor features (4 scales associated with 8 directions) and 8 GLCM features are extracted from the PCA top component. The two textural features have been recognized to have complementary properties [32]. For GF, 10 features not only avoid large amount of the calculation but also give sufficient information, while for TF, the 8 GLCM features are employed frequently as well as the Gabor features. Although different studies have selected different numbers of scales and directions for Gabor features, we use relatively fewer features in order to increase the efficiency of the calculation procedure. We do not analyze the properties of different parameters in detail in this paper. For the first 2 datasets, ISOMAP features are employed as the only features based on manifold learning while for the third dataset, we try to utilize LE features instead of ISOMAP. As described before, the features actually contain 4 different types, including 10 linear GF (PC), 10 nonlinear GF (ISOMAP or LE), 32 filter-based TF (2D Gabor), and 8 statistical TF (GLCM). Features are normalized before inputting the following approaches.

The paper addressed three scenarios to combine multiple features.

- (i) Scenario 1: direct combination

We directly combine different types of feature vectors, such as GF and TF; thus, a longer feature vector is formed.

- (ii) Scenario 2: dimensionality framework

The state-of-the-art dimensionality algorithm LE has been widely discussed and utilized in many studies [33]. We consider the method reported in [9].

- (iii) Scenario 3: multiple kernel method

The existing multiple kernel learning algorithms have to calculate the weight factors through an iterative process. To avoid the complex iterative calculation, we estimate the weight of different features before classification. We design the method by the distance measurement. Finally, the basis kernels are multiplied by the relevant weight factors. Then, it is converted to a simple kernel classifier. When the combinations are decided, the SVM [34] classifier is employed to test on these features with its parameters  $C$  and  $g$  confirmed through cross-validation with the training samples [35].

### 3. Experimental Section

**3.1. Hyperspectral Image Data.** Three commonly used datasets were tested in the experiments. All of them were acquired by hyperspectral sensors with different spatial resolutions. Researchers have been trying to improve the classification performance on these scenes for a long time. In this paper,

TABLE 1: Sample distribution of IP dataset.

Number	Class	Train sample	Number	Number	Class	Train sample	Number
1	Corn-notill	72	1434	7	Soybean-notill	48	968
2	Corn-mintill	42	834	8	Soybean-mintill	123	2468
3	Corn	12	234	9	Soybean	31	614
4	Grass-pasture	25	497	10	Wheat	11	212
5	Grass-trees	37	747	11	Woods	65	1294
6	Hay-windrowed	24	489	12	Building-road	19	380

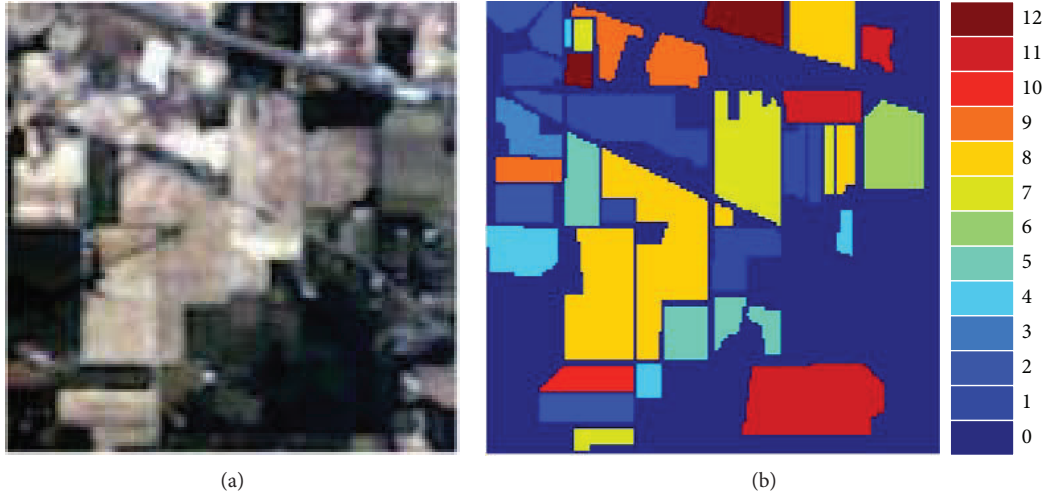


FIGURE 1: IP dataset: (a) IP scene; (b) labeled pixels.

experiments are carried out on these scenes under similar experiment conditions.

**3.1.1. Indian Pine Scene.** The Indian pine (IP) dataset, derived from the airborne visible/infrared imaging spectrometer (AVIRIS), is one of the most commonly used hyperspectral image data for test. The resolution of the image is 30 m, and the size is  $145 \times 145$  pixels. The sensor contains 220 bands in which 62 bands have to be discarded due to water absorption or noise and finally 158 valid bands are reserved in the area. The dataset mainly covers agricultural lands with 10171 labeled data points divided into 12 classes. In the experiment, 5% of the labeled data points are considered as training samples for each class. Table 1 lists the exhaustive class information and the number of samples. Figure 1 shows the image and the labeled condition.

**3.1.2. Salinas Scene.** Salinas (SL) dataset (Figure 2) was also acquired by AVIRIS. 204 valid bands are selected from the total 224 bands. The resolution of the scene is 3.7 m, and the size is  $512 \times 217$  pixels in which 54129 pixels are labeled. 1% of the labeled pixels are considered as training samples for each class. The dataset is divided into 16 classes with the details listed in Table 2.

**3.1.3. Pavia University Scene.** The Pavia University (PU) dataset (Figure 3) was acquired by ROSIS, and the location is Pavia University, Italy. The resolution is 1.3 m which ranks

the highest among the three datasets. The image size is  $610 \times 340$  pixels, including 207400 data points. 113 valid bands are selected from the total 115 bands with 2 noisy bands removed. Different from the former scenes, PU mainly covers artificial lands. 2% of 42776 labeled pixels are considered as training samples for each class. The land cover details are listed in Table 3.

**3.2. Research on Different Dimensionality Reduction Scenarios.** A systematic research is made on two DR scenarios for hyperspectral image classification based on multiple features. Different DR tools (linear and nonlinear) and different types of textural features are employed. One scenario is the conventional procedure characterized by combining hyperspectral bands with other features before reducing the dimensionality; the other is featured by reducing the dimensionality of the original hyperspectral bands before combining other extracted features. In addition, classification scenarios by only spectral features and only textural features help to compare and analyze the results. As a result, four scenarios are listed in Table 4. In scenario 3, we search the best output dimension  $d$  among 5-45 with the interval of 5 for each dataset. In scenario 4, the first 10 features are selected after the DR process.

We repeat ten times of independent experiments for each case. In each trial, the samples are randomly selected from all the labeled pixels and the selection strategy is stratified by

TABLE 2: Sample distribution of SL dataset.

Number	Class	Train sample	Number	Number	Class	Train sample	Number
1	Broccoli 1	20	2009	9	Grape 2	62	6203
2	Broccoli 2	37	3726	10	Corn	33	3278
3	Fallow 1	20	1976	11	Lettuce 1	11	1068
4	Fallow 2	14	1394	12	Lettuce 2	19	1927
5	Fallow 3	27	2678	13	Lettuce 3	9	916
6	Stubble	40	3959	14	Lettuce 4	11	1070
7	Celery	36	3579	15	Grape 3	73	7268
8	Grape 1	113	11271	16	Grape 4	18	1807

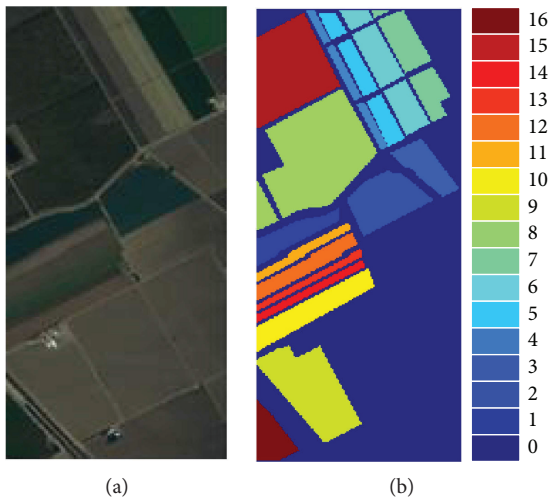


FIGURE 2: SL dataset: (a) SL scene; (b) labeled pixels.

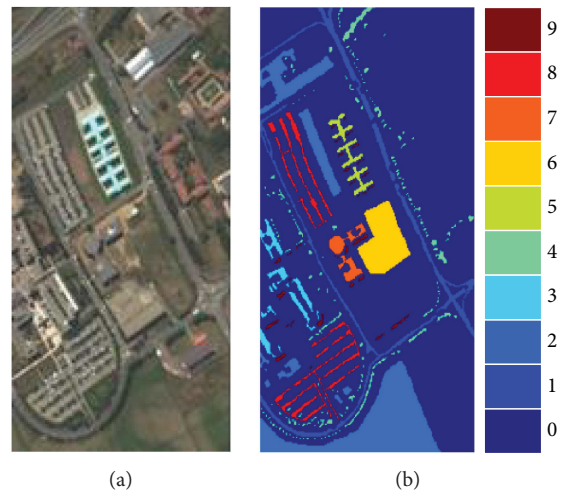


FIGURE 3: PU dataset: (a) PU image; (b) labeled pixels.

classes. We calculated the average overall accuracy, kappa index, and the best  $d$  for DR scheme in scenario 3. The parameters are optimized by the training samples.

Three datasets (IP, SL, and PU) are tested, and the performance is reported in Table 5. For each method,  $d$  relates to the best performance in scenario 3. We can get from Table 5 that the classification accuracies in scenario 4 are generally higher than those in scenario 3, especially when textural features perform well by themselves. Even if textural features do not perform well, scenario 3 is not always superior to scenario 4. We may explore the reason referring to scenario 1 and scenario 2. When textural features outperform spectral features and have less numbers, scenario 4 obviously outperforms scenario 3. Features with a larger number may be dominated during a global DR transformation after the feature combination, regardless of whether the DR tool is linear or nonlinear. As a result, a higher accuracy yield is in scenario 4, owing to the good performance and sufficient feature numbers of textural features, like Gabor features. On the contrary, the initial hyperspectral features with both larger numbers and worse performance influence and reduce the accuracy (scenario 3). However, when spectral features outperform textural features, accuracies in scenario 3 are close or superior to those in scenario 4 according to the “PC-GLCM” and “LE-GLCM” methods in Table 5. In addition,

Table 5 shows that, regardless of whether the DR algorithm is linear or nonlinear, it is not easy to find the empirical  $d$  during the procedure of DR.

With the development of textural feature extraction technique, the performance of textural features researchers exploited often outperforms the initial hyperspectral features with less numbers. As a result, it is proper to reduce the dimensionality of hyperspectral features before combining with textural features or other features. Generally, we cannot exactly predict the performance of different groups of features, so we just reduce the dimensionality of hyperspectral features to a certain extent and select moderate numbers of low representation.

**3.3. Combination Frameworks.** In the experiment, we design 5 feature selection scenarios for comparison: hyperspectral bands only, GF only, TF only, integrating GF and TF, and integrating GF, TF, and hyperspectral bands. The results of 5 groups of features associated with 3 combining strategies are listed. In addition, for IP scenes, details of the DR framework (with the dimensions no more than 60) will be presented; for SL scenes, the classification accuracies with different groups of features will be shown in an intuitive way; for PU scenes, we will investigate the complementary properties of different feature groups.

TABLE 3: Sample distribution of PU dataset.

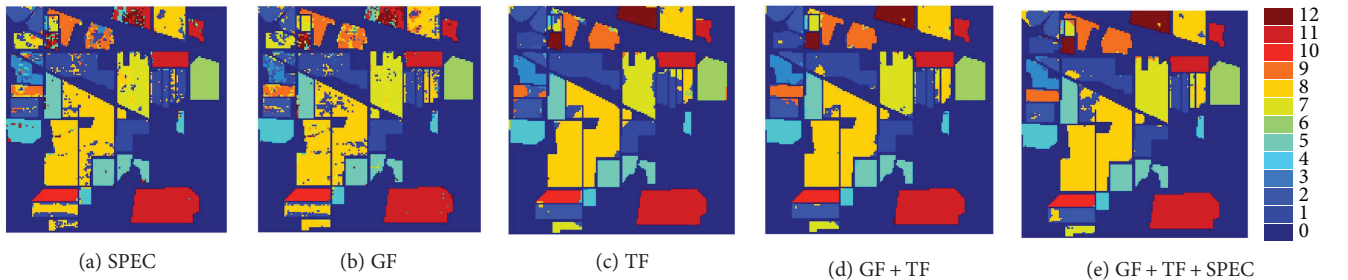
Number	Class	Train sample	Number	Number	Class	Train sample	Number
1	Asphalt road	133	6631	6	Bare ground	101	5029
2	Grass	373	18649	7	Asphalt roof	27	1330
3	Gravel	42	2099	8	Tile	74	3682
4	Trees	61	3064	9	Shadow	19	947
5	Metal roof	27	1345				

TABLE 4: Details of experimental scenarios.

Scenario	Features
Scenario 1	Spectral features
Scenario 2	Textural features
Scenario 3	Combine both features and reduce the dimensionality as a whole
Scenario 4	Combine textural features with low-dimensional spectral features

TABLE 5: Experimental results of different datasets associated with different scenarios. ‘‘Sc.’’ represents different scenarios in Table 4.

Method	IP				SL				PU			
	Sc.1	Sc.2	Sc.3	Sc.4	Sc.1	Sc.2	Sc.3	Sc.4	Sc.1	Sc.2	Sc.3	Sc.4
PC	81.31	93.60	94.31	<b>96.08</b>	89.52	95.9	98.28	<b>98.44</b>	82.87	85.7	97.44	<b>98.67</b>
Gabor	0.784	0.927	0.935	<b>0.955</b>	0.833	0.954	0.981	<b>0.983</b>	0.765	0.807	0.966	<b>0.983</b>
			$d = 30$				$d = 35$				$d = 40$	
PC	81.31	48.19	<b>78.52</b>	77.25	89.52	57.16	<b>89.69</b>	<b>89.72</b>	82.87	65.83	<b>91.17</b>	87.36
GLCM	0.784	0.365	<b>0.752</b>	0.737	0.833	0.508	<b>0.885</b>	<b>0.885</b>	0.765	0.503	<b>0.882</b>	0.83
			$d = 20$				$d = 30$				$d = 25$	
LE	81.31	93.60	80.11	<b>95.66</b>	89.52	95.9	95.51	<b>98.78</b>	82.87	85.7	96.17	<b>97.26</b>
Gabor	0.784	0.927	0.772	<b>0.95</b>	0.833	0.954	0.95	<b>0.986</b>	0.765	0.807	0.949	<b>0.964</b>
			$d = 40$				$d = 40$				$d = 35$	
LE	81.31	48.19	61.92	<b>68.02</b>	89.52	57.16	83.66	<b>85.34</b>	82.87	65.83	<b>85.51</b>	81.98
GLCM	0.784	0.561	0.561	<b>0.628</b>	0.833	0.508	0.817	<b>0.837</b>	0.765	0.503	<b>0.805</b>	0.754
			$d = 35$				$d = 35$				$d = 35$	

FIGURE 4: Classification maps of the IP dataset with directly combined features; (a)–(e), respectively, represent different groups of input features: spectral features, GF, TF, GF combined with TF, and all features along with the spectral features.  $d$  is the feature dimension for input.

Also, complementary properties of linear and nonlinear features will be discussed. Finally, classification results with weight estimation and without weight estimation will be compared in accuracy.

10 independent experiments are repeated for each case. In each trial, the samples are randomly selected from all the labeled pixels and the selection strategy is stratified by classes. Overall accuracy (OA) is calculated by ten trails. We also get

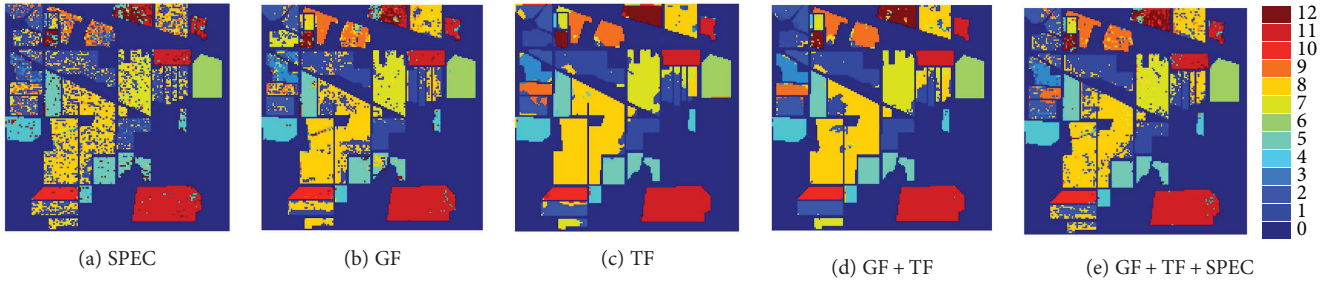


FIGURE 5: Classification maps of the IP dataset with features under a manifold-based framework; (a)–(e), respectively, represent different groups of input features: spectral features, GF, TF, GF combined with TF, and all features along with the spectral features.  $d$  is the dimension associated with the best performance.

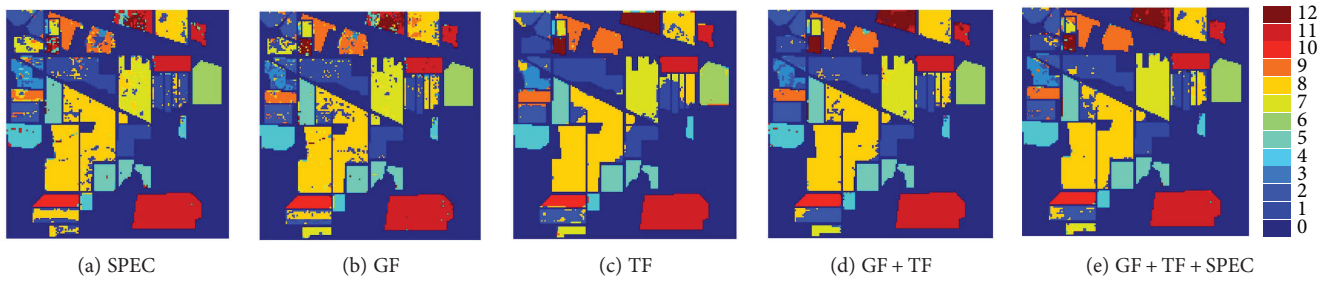


FIGURE 6: Classification maps of the IP dataset by the multiple kernel method; (a)–(e), respectively, represent different groups of input features: spectral features, GF, TF, GF combined with TF, and all features along with the spectral features.  $d$  is the feature dimension for input.

the average kappa index, execution times, and the best  $d$  for the DR scheme in scenario 3. The parameters are also optimized by the training samples.

**3.3.1. IP Scenes.** Figures 4–6 present classification results based on different groups of features associated with 3 combining strategies. The accuracies can be seen in Table 6. In each figure, GF + TF has the best performance both in accuracy and visual perspectives. Figures 4(a), 5(a), and 6(a) yield the most misclassifications, and Figures 4(b), 5(b), and 6(b) show better results than do Figures 4(a), 5(a), and 6(a) with less features. Figures 4(c), 5(c), and 6(c) have much better results than Figures 4(b), 5(b), and 6(b) have, owing to better textural features. With the help of the integration of GF and TF, Figures 4(d), 5(d), and 6(d) have the fewest classification errors. It has to be mentioned that there is no need to add initial hyperspectral features in the proposed method, because the accuracy reduces when the spectral features are added referring to the results in Figures 4(e), 5(e), and 6(e). As a result, 60 input features yield the best result. It can also be discovered from Table 6 that nonlinear LE dimensionality reduction tools spend more time when dealing with the combined features. According to the comparison of three organization schemes, it can be concluded that the overall calculation amount of the nonlinear DR procedure is greater than that of the classification procedure with relatively higher inputted dimensions. Also, we find that Figure 4 outperforms Figures 5 and 6. So the dimensionality framework or multiple kernel method has not given rise to a better classification

TABLE 6: Classification results by different features for IP dataset, including OA, kappa index, and the execution time.

IP		SPEC	GF	TF	GF + TF	TF + GF + SPECT
Direct combine	OA (%)	81.30	80.49	94.59	<b>96.39</b>	<b>96.02</b>
	Kappa	0.784	0.775	0.938	0.959	0.954
	Time (s)	3.3	0.99	1.46	1.77	4.18
LE framework	OA (%)	62.31	78.42	90.98	93.76	79.36
	Kappa	0.568	0.751	0.897	0.929	0.764
	Best $d$	50	20	35	55	40
Multiple kernel	Time (s)	4.23	2.44	2.73	3.38	4.06
	OA (%)	81.30	85.89	93.72	94.36	92.88
	Kappa	0.784	0.838	0.928	0.935	0.918
	Time (s)	3.3	4.48	4.62	6.91	7.48

result than the direct way of combination. In addition, it is not easy to find a desirable dimension in the dimensionality reduction process (Figure 7).

**3.3.2. SL Scenes.** The SL dataset has more feature numbers and a higher resolution. Extremely high accuracy is yielded

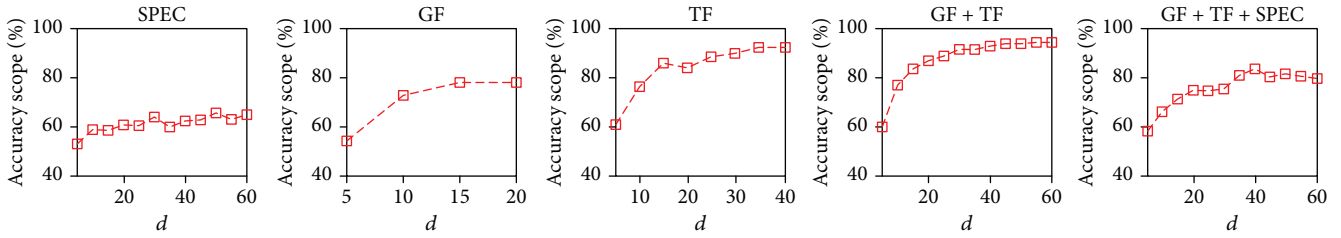


FIGURE 7: Relationship of  $d$  and accuracy in the IP dataset ( $d \leq 60$ ).

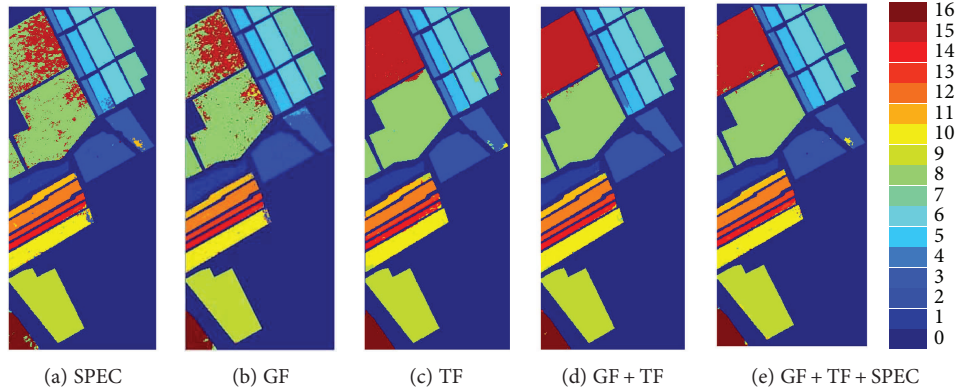


FIGURE 8: Classification maps of the SL dataset with directly combined features; (a)–(e), respectively, represent different groups of input features: spectral features, GF, TF, GF combined with TF, and all features along with the spectral features.  $d$  is the feature dimension for input.

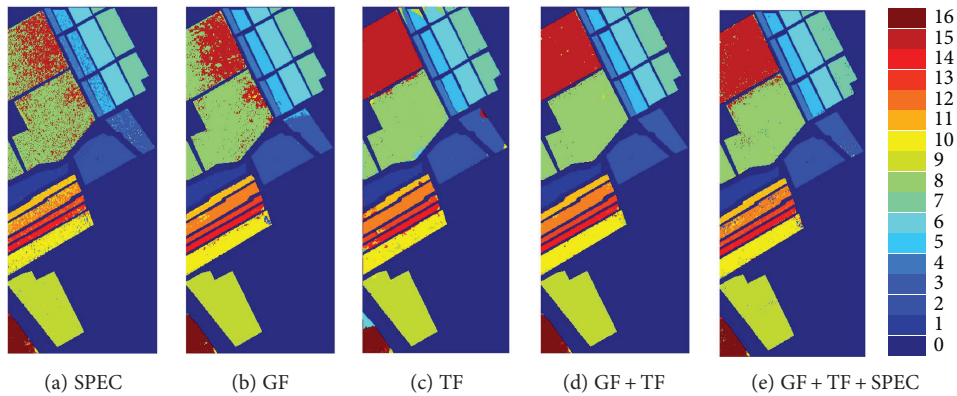


FIGURE 9: Classification maps of SL dataset with features under manifold based framework; (a)–(e), respectively, represent different groups of input features: spectral features, GF, TF, GF combined with TF, and all features along with the spectral features.  $d$  is the dimension associated with the best performance.

with the proposed scenario, and similar regulations in IP dataset can be found. The results are listed in Figures 8–10. Table 7 lists the accuracies by different scenarios. Among the 16 classes, it is challenging to distinguish class 8 and class 15, while the GF+TF strategy shows the perfect accuracy rate.

However, no matter what kinds of combination strategy are employed, the results have not varied a lot for one group of features and often remain in a certain range. The accuracies change more obviously and regularly with the variation of the input features (Figure 11). So we can suggest that the

selection of features is more important than combining approaches in hyperspectral image classification.

However, no matter what kinds of combination strategy are exploited, the results do not vary a lot within a fix group of features. The accuracies just remain in a certain scope. The accuracies change more obviously and regularly with the variation of input features (Figure 11). So we can suggest that the selection of features is more important than the combination approaches in hyperspectral image classification. In addition, we can conclude that the proposed strategy applies to different combination schemes.

TABLE 7: Classification results by different features for SL dataset, including OA, kappa index, and execution time.

SL		SPEC	GF	TF	GF + TF	TF + GF + SPEC
Direct combine	OA (%)	89.68	89.89	97.47	<b>98.95</b>	<b>98.5</b>
	Kappa	0.885	0.887	0.972	0.988	0.983
	Time (s)	10.9	3.88	5.98	6.63	9.7
LE framework	OA (%)	83.28	89.86	95.57	<b>98.18</b>	95.69
	Kappa	0.813	0.887	0.951	0.980	0.952
	Best $d$	35	20	35	35	45
Multiple kernel	Time (s)	11.21	5.42	7.82	7.29	9.743
	OA (%)	89.68	90.01	96.83	97.74	97.34
	Kappa	0.885	0.899	0.964	0.974	0.970
	Time (s)	10.9	3.88	5.98	6.63	15.7

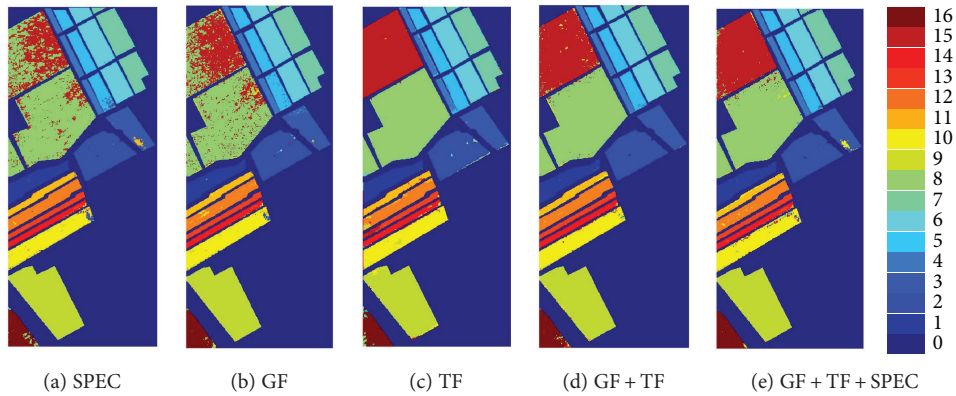
FIGURE 10: Classification maps of the SL dataset with directly combined features; (a)–(e), respectively, represent different groups of input features: spectral features, GF, TF, GF combined with TF, and all features along with the spectral features.  $d$  is the feature dimension for input.

TABLE 8: Classification results by different features for PU dataset, including OA, kappa index, and execution time.

PU		SPEC	GF	TF	GF + TF	TF + GF + SPEC
Direct combine	OA (%)	83.61	85	92.78	<b>98.6</b>	<b>98.48</b>
	Kappa	0.775	0.797	0.904	0.982	0.980
	Time (s)	8.91	4.36	2.38	6.6	8.5
LE framework	OA (%)	80.89	83.66	91.78	<b>98.44</b>	97.69
	Kappa	0.741	0.778	0.89	0.979	0.969
	Best $d$	25	15	40	55	45
Multiple kernel	Time (s)	9.23	5.48	6.62	7.91	8.48
	OA (%)	83.61	84.91	96.11	98.08	97.86
	Kappa	0.775	0.796	0.948	0.975	0.972
	Time (s)	8.91	4.76	5.96	7.03	12.05

3.3.3. *PU Scenes*. Among the three datasets, PU has the highest resolution and the most pixels. Table 8 lists the accuracies by different scenarios. In this high-resolution dataset, the complementary properties of GF and TF have a more apparent representation. For example, in Figures 12, 13, and 14(a) and 14(b), with GF, the misclassification occurs frequently

between class 2 (grass) and class 6 (bare soil), while TF discriminates the class pair well; class 1 (asphalt road) and class 4 (tree) are challenging classes for TF because of the close location, but GF or spectral features perform well between the 2 classes. Figure 15 presents a direct perspective of the complementary properties of different feature groups.

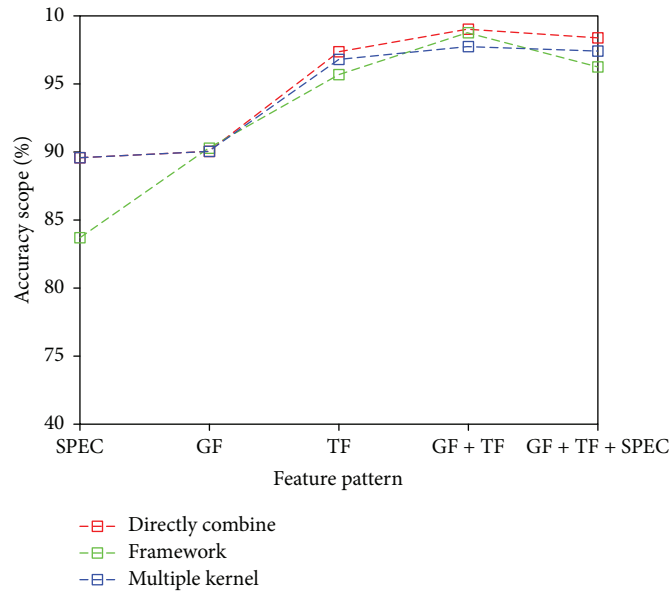


FIGURE 11: Accuracy change range with features and strategies on the SL dataset.

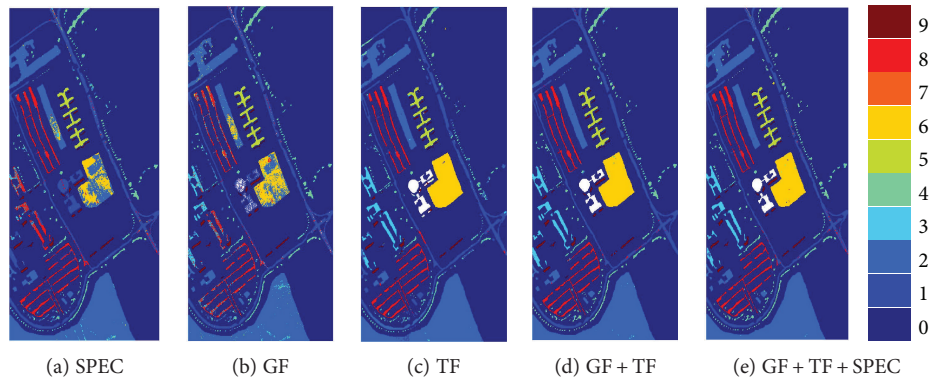


FIGURE 12: Classification maps of the PU dataset with features under a manifold-based framework; (a)–(e), respectively, represent different groups of input features: spectral features, GF, TF, GF combined with TF, and all features along with the spectral features.  $d$  is the feature dimension for input.

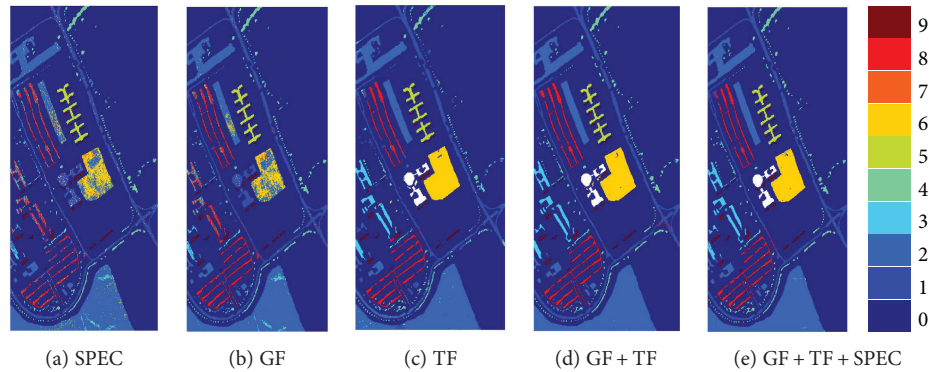


FIGURE 13: Classification maps of the PU dataset by the multiple kernel method; (a)–(e), respectively, represent different groups of input features: spectral features, GF, TF, GF combined with TF, and all features along with the spectral features.  $d$  is the dimension associated with the best performance.

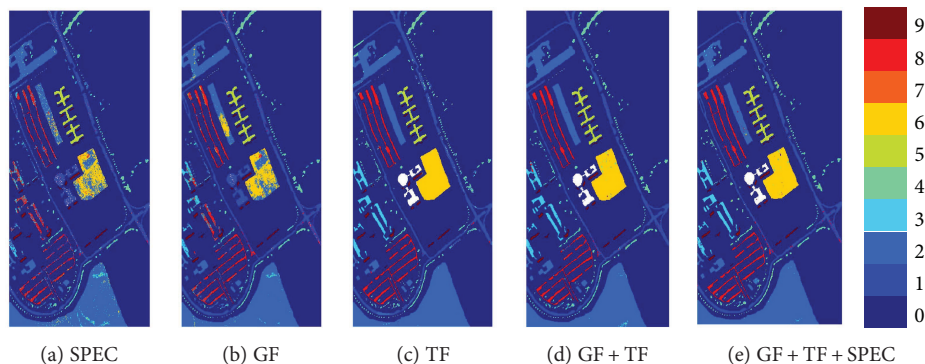


FIGURE 14: Classification maps of the PU dataset with directly combined features; (a)–(e), respectively, represent different groups of input features: spectral features, GF, TF, GF combined with TF, and all features along with the spectral features.  $d$  is the feature dimension for input.

TABLE 9: The effect of autoweighting method in the GF + TF strategy.

Method	IP		SL		PU	
	Directly combine	LE framework	Directly combine	LE framework	Directly combine	LE framework
Autoweight	96.39	93.76	98.95	98.18	98.6	98.44
Without weight	95.87	93.01	98.47	97.61	97.23	96.9

As has been discussed before, different groups of features have their specific properties. Different feature extraction algorithms yield different feature numbers, so it seems necessary to add weight factors to different groups of features in different circumstances. We can find the improvement of the autoweighting method in the proposed GF + TF strategy in Table 9.

**3.4. Discussions.** It is necessary to discuss the experimental results on the hyperspectral datasets.

The summary of the experiments with different DR schemes is as follows: textural features combined with a low-dimensional spectral features prove to be a more appropriate strategy according to experiments in Section 3.2, especially when textural features perform well and have less numbers. When textural features do not work well, it is not always the case. However, great efforts have been made to extract favorable textural features for hyperspectral image expression, so for most circumstances, the textural features we select are empirically superior. As a result, scenario 4 in Table 4 is recommended.

The summary of the experiments with the combination scenarios is as follows: for all the datasets, the GF + TF method performs best both in accuracy and visual perspectives; “global features” and “textural features” present clear complementary properties in the classification results. The GF + TF combination with only 60 input features works well without the incorporation of the original hyperspectral bands. The weight estimation method proves to be effective when dealing with multiple features. In addition, the number of the input features of the GF + TF strategy is independent of the band number of the images or the types of sensors.

The summary of the experiments with different feature combination frameworks is as follows: the results yielded by different combination strategies do not vary a lot if the input

features are confirmed; compared with the “framework” strategy, the “direct combination” strategy with the only 60 GF + TF input features not only performs better but also avoids great calculating amount and large number of dimensions; multiple kernel method and nonlinear DR framework sometimes lead to desirable results, but the best  $d$  is hard to determine, which can be reflected both in our experiments and in other studies.

We can conclude by the experimental results and the discussions above that what kinds of features to be combined influences the classification results to a larger extent than the strategies of integrating multiple features. In addition, multiple features with complementary properties lead to good classification results. In this paper, we exploit 4 different features for combination, including linear and nonlinear “global features” and filter-based and statistics-based “textural features,” which ensure the complementary and diverse properties.

Pattern recognition has been applied in many fields. Hyperspectral remote sensing image classification is a peculiar application and has its own characteristics. Compared with image recognition (like in [9, 13]) and medicine field (such as gene and protein classification [7]), remote sensing image classification problems have a relatively lower dimension or at least a smaller  $d/N$  ( $d$  represents dimension and  $N$  represents labeled samples). According to an overall statistics in [15], when  $d \gg N$  (like some cases in body, face, object image recognition, or gene classification), the accuracy appears low (Figure 16). In this case, a DR algorithm will help to improve both the results and the classification efficiency. However, in the case of  $N > d$ , the accuracy appears pretty well and a DR framework does not lead to evidently better results. In addition, it is not easy to find the best  $d$  in different cases according to our experimental results and Figure 7. In fact, researchers have not found an effective way of

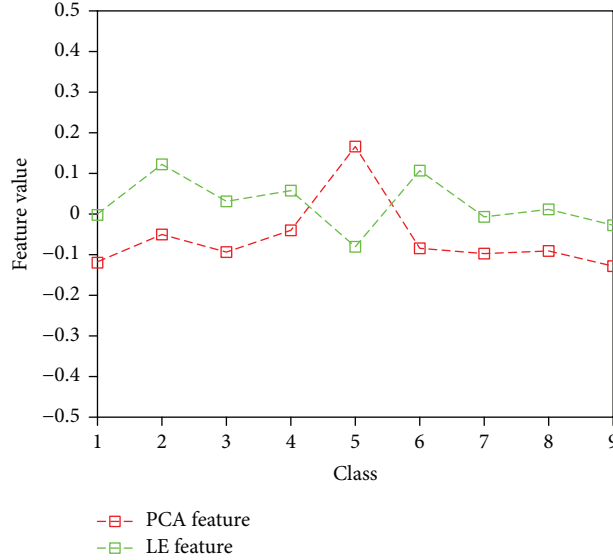


FIGURE 15: Complementary properties of PC and LE features for all classes in the PU dataset.

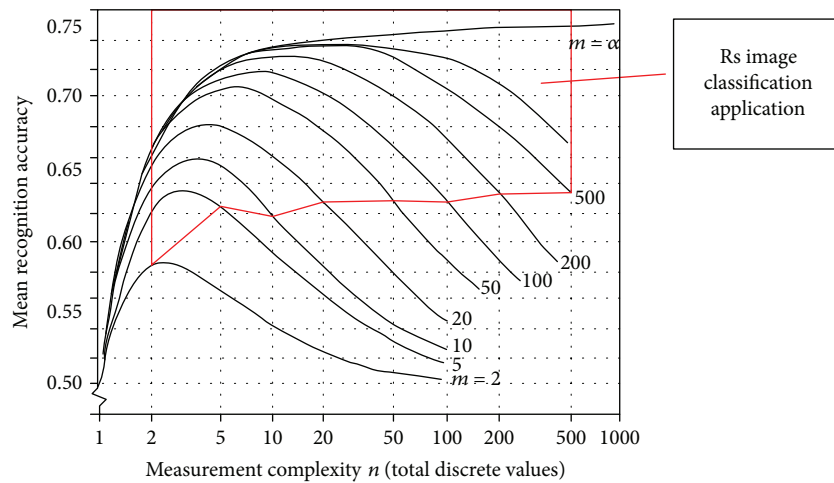


FIGURE 16: Hughes curves labeled by common application of remote sensing image classification.

confirming the most desirable  $d$ . The latter case (a smaller  $d/N$ ) may be the common application of hyperspectral remote sensing image classification in the temporary period of development (Figure 16). With the development of the hyperspectral sensors, the bands may increase; thus, the area of the red frame in Figure 16 may grow. However, the proposed GF + TF strategy may still be practical for use because it is independent of the bands of the sensors.

#### 4. Conclusions

Hyperspectral sensors provide more details in spectra; however, problems are yielded along with the advantages. One is the high-dimension problem, and the other is the possibility of extracting multiple features from the hyperspectral images. In this paper, a systematic research is made to find an appropriate strategy to deal with classification problems

of multiple features. Then, we further exploit the complementary features to improve hyperspectral image classification performance. Experiments on 3 hyperspectral datasets suggest that the scheme GF + TF is effective. The main contribution can be concluded as follows: first, based on the experiments, we suggest DR algorithms work better as feature acquirement methods than just reducing the dimensions. The paper further selects features from a different perspective in multiview problem. In the previous work, there have been feature combination ideas characterized by “spectral and nonspectral” or more recent schemes like “linear and nonlinear.” However, we present “global and nonglobal” strategy and take linear and nonlinear global features (like PC, ISO-MAP, and LE) as a portion of features for the first time. We have also got the conclusion that features with different types are more likely to have complementary properties. Second, concluded from the experimental results, feature selection

proves to be more important than how to organize multiple features in hyperspectral image classification problems. Third, a systematic research has been made on the combination frameworks of multiple features, including direct combination, manifold learning, and multiple kernel method. We have found that complex methods like manifold framework and multiple kernel do not lead to the increase in accuracy; instead, the direct combine strategy with an autoweight calculation performs the best. Finally, we have compared hyperspectral image classification problems with other applications of pattern recognition and clearly analyzed the characteristics of the former.

As future work, we will continue to find more complementary features for integration in hyperspectral remote sensing image classification based on the experiments. For example, shape features have been widely developed recently and have not been considered in the study. In addition, we will further discuss the internal redundancy of each group of features.

### Conflicts of Interest

The authors declare no conflict of interests.

### Authors' Contributions

Yuntao Ma is the main author who proposed the basic idea, completed the experiments, and carefully revised this manuscript. Ruren Li and Guang Yang provided the useful suggestions on designing the approaches involved in our proposed strategy. Lishuang Sun and Jingli Wang helped to modify the manuscript.

### Acknowledgments

The study was funded by the National Natural Science Foundation of China "Study on environmental impact mechanism of surface deformation monitoring in open pit mine and inversion methods under low coherence environment based on GB-SAR" (no. 51774204) and "TGRA Forest Cover and Dynamic Change Detection Based on Time Series Remote Sensing Images" (no. 2014QC018).

### References

- [1] H. Song and Y. Wang, "A spectral-spatial classification of hyperspectral images based on the algebraic multigrid method and hierarchical segmentation algorithm," *Remote Sensing*, vol. 8, no. 4, p. 296, 2016.
- [2] M. Diani, N. Acito, M. Greco, and G. Corsini, "A new band selection strategy for target detection in hyperspectral images," *Lecture Notes in Computer Science*, vol. 5179, pp. 424–431, 2008.
- [3] M. Fauvel, J. Chanussot, and J. A. Benediktsson, "A spatial-spectral kernel-based approach for the classification of remote-sensing images," *Pattern Recognition*, vol. 45, no. 1, pp. 381–392, 2012.
- [4] A. Plaza, P. Martinez, J. Plaza, and R. Perez, "Dimensionality reduction and classification of hyperspectral image data using sequences of extended morphological transformations," *IEEE Transactions on Geoscience and Remote Sensing*, vol. 43, no. 3, pp. 466–479, 2005.
- [5] S. Z. Wang, Y. Li, and W. Cheng, "Distributed classification of localization attacks in sensor networks using exchange-based feature extraction and classifier," *Journal of Sensors*, vol. 2016, Article ID 8672305, 18 pages, 2016.
- [6] P. H. Hsu, "Feature extraction of hyperspectral images using wavelet and matching pursuit," *ISPRS Journal of Photogrammetry and Remote Sensing*, vol. 62, no. 2, pp. 78–92, 2007.
- [7] G. Lee, C. Rodriguez, and A. Madabhushi, "Investigating the efficacy of nonlinear dimensionality reduction schemes in classifying gene and protein expression studies," *IEEE/ACM Transactions on Computational Biology and Bioinformatics*, vol. 5, no. 3, pp. 368–384, 2008.
- [8] G. Yang and S. Fang, "Improving remote sensing image classification by exploiting adaptive features and hierarchical hybrid decision trees," *Remote Sensing Letters*, vol. 8, no. 2, pp. 156–164, 2016.
- [9] T. Zhang, D. Tao, X. Li, and J. Yang, "Patch alignment for dimensionality reduction," *IEEE Transactions on Knowledge and Data Engineering*, vol. 21, no. 9, pp. 1299–1313, 2009.
- [10] L. Zhang, L. Zhang, D. Tao, and X. Huang, "On combining multiple features for hyperspectral remote sensing image classification," *IEEE Transactions on Geoscience and Remote Sensing*, vol. 50, no. 3, pp. 879–893, 2012.
- [11] J. Li, X. Huang, P. Gamba et al., "Multiple feature learning for hyperspectral image classification," *IEEE Transactions on Geoscience & Remote Sensing*, vol. 53, pp. 1592–1606, 2015.
- [12] A. Rakotomamonjy, F. R. Bach, S. Canu, and Y. Grandvalet, "Simple MKL," *Journal of Machine Learning Research*, vol. 9, pp. 2491–2521, 2008.
- [13] T. Xia, D. Tao, T. Mei, and Y. Zhang, "Multiview spectral embedding," *IEEE Transactions on Systems, Man, and Cybernetics, Part B (Cybernetics)*, vol. 40, no. 6, pp. 1438–1446, 2010.
- [14] H. Liu, J. Yang, H. Yang, and F. Yi, "Soft sensor of vehicle state estimation based on the kernel principal component and improved neural network," *Journal of Sensors*, vol. 2016, Article ID 9568785, 8 pages, 2016.
- [15] G. Hughes, "On the mean accuracy of statistical pattern recognizers," *IEEE Transactions on Information Theory*, vol. 14, no. 1, pp. 55–63, 1968.
- [16] S. Sonnenburg, G. Rätsch, C. Schäfer, and B. Schölkopf, "Large scale multiple kernel learning," *Journal of Machine Learning Research*, vol. 7, pp. 1531–1565, 2006.
- [17] M. Gönen and E. Alpaydm, "Multiple kernel learning algorithms," *Journal of Machine Learning Research*, vol. 12, pp. 2211–2268, 2011.
- [18] P. Du, A. Samat, P. Gamba, and X. Xie, "Polarimetric sar image classification by boosted multiple-kernel extreme learning machines with polarimetric and spatial features," *International Journal of Remote Sensing*, vol. 35, no. 23, pp. 7978–7990, 2014.
- [19] Q. Zhang, Y. Tian, Y. Yang, and C. Pan, "Automatic spatial-spectral feature selection for hyperspectral image via discriminative sparse multimodal learning," *IEEE Transactions on Geoscience and Remote Sensing*, vol. 53, no. 1, pp. 261–279, 2015.
- [20] C. F. Tsai and Y. C. Hsiao, "Combining multiple feature selection methods for stock prediction: union, intersection, and multi-intersection approaches," *Decision Support Systems*, vol. 50, no. 1, pp. 258–269, 2010.

- [21] H. Hotelling, "Analysis of a complex of statistical variables into principal components," *Journal of Educational Psychology*, vol. 24, no. 6, pp. 417–441, 1933.
- [22] R. A. Fisher, "The use of multiple measurements in taxonomic problems," *Annals of Eugenics*, vol. 7, no. 2, pp. 179–188, 1936.
- [23] J. B. Tenenbaum, V. de Silva, and J. C. Langford, "A global geometric framework for nonlinear dimensionality reduction," *Science*, vol. 290, no. 5500, pp. 2319–2323, 2000.
- [24] M. Belkin and P. Niyogi, "Laplacian eigenmaps for dimensionality reduction and data representation," *Neural Computation*, vol. 15, no. 6, pp. 1373–1396, 2006.
- [25] C. Chen, W. Li, H. Su, and K. Liu, "Spectral-spatial classification of hyperspectral image based on kernel extreme learning machine," *Remote Sensing*, vol. 6, no. 6, pp. 5795–5814, 2014.
- [26] S. C. H. Hoi, R. Jin, P. Zhao, and T. Yang, "Online multiple kernel classification," *Machine Learning*, vol. 90, no. 2, pp. 289–316, 2013.
- [27] A. Mohan, G. Sapiro, and E. Bosch, "Spatially coherent nonlinear dimensionality reduction and segmentation of hyperspectral images," *IEEE Geoscience and Remote Sensing Letters*, vol. 4, no. 2, pp. 206–210, 2007.
- [28] S. T. Roweis and L. K. Saul, "Nonlinear dimensionality reduction by locally linear embedding," *Science*, vol. 290, no. 5500, pp. 2323–2326, 2000.
- [29] Z. Zhang and H. Zha, "Principal manifolds and nonlinear dimension reduction via local tangent space alignment," *SIAM Journal on Scientific Computing*, vol. 26, pp. 313–338, 2005.
- [30] D. Tao, X. Li, X. Wu, and S. J. Maybank, "General tensor discriminant analysis and gabor features for gait recognition," *IEEE Transactions on Pattern Analysis and Machine Intelligence*, vol. 29, no. 10, pp. 1700–1715, 2007.
- [31] M. Hanta-Kasari, J. Parkkinen, and T. Jaaskelainen, "Generalized co-occurrence matrix for multispectral texture analysis," in *Proceedings of the 13th International Conference on Pattern Recognition, Vienna, Austria, August*, pp. 25–29, IEEE Computer Society Press, Los Alamitos, USA, 1996.
- [32] Y. O. Ouma, J. Tetuko, and R. Tateishi, "Analysis of co-occurrence and discrete wavelet transform textures for differentiation of forest and non-forest vegetation in very-high-resolution optical-sensor imagery," *International Journal of Remote Sensing*, vol. 29, no. 12, pp. 3417–3456, 2008.
- [33] Y. Zhou, *Nonlinear Feature Extraction of Hyperspectral Remote Sensing Data Based on a Fast Manifold Learning Strategy*, PhD, Wuhan University, China, 2013.
- [34] C. Cortes and V. Vapnik, "Support vector networks," *Machine Learning*, vol. 20, no. 3, pp. 273–297, 1995.
- [35] M. Stone, "Cross-validatory choice and assessment of statistical predictions," *Journal of the Royal Statistical Society Series B-Statistical Methodology*, vol. 36, pp. 111–147, 1974.

## Research Article

# Error Compensation Technique for a Resistance-Type Differential Pressure Flow Sensor

Guimei Wang , Tao Chu , Lijie Yang , and Fang Sun 

College of Mechanical and Equipment Engineering, Hebei University of Engineering, Handan 056038, China

Correspondence should be addressed to Lijie Yang; yanglijie255@163.com

Received 15 October 2017; Revised 5 January 2018; Accepted 23 January 2018; Published 29 April 2018

Academic Editor: Zongyao Sha

Copyright © 2018 Guimei Wang et al. This is an open access article distributed under the Creative Commons Attribution License, which permits unrestricted use, distribution, and reproduction in any medium, provided the original work is properly cited.

A flow sensor is designed based on resistance-type differential pressure flow (RDPF) method, and the flow data is measured during a coal gangue paste-filling process. The measurement error characteristics of a RDPF sensor are analyzed. Periodic and aperiodic errors are then modeled separately. The model for the periodic error is established by Fourier series approximation using least squares solution of an overdetermined equation to solve for the model parameters. The model for the aperiodic error is established using an online least squares support vector machine (LS-SVM) method. The cross-validation is used to solve model parameters. Simulations and experiments show that the dynamic measurement accuracy of the sensor is greatly improved by error compensation, thereby reducing filling material waste and improving the economic efficiency.

## 1. Introduction

Coal gangue paste filling is a backfill mining technique that has the dual aim of reducing environmental pollution caused by coal gangue and flyash and lessening the risk of subsidence [1]. As green filling mining technology, the paste-filling technique has the above advantages. However, with the long filling pipe, nonuniform velocity, filling paste of large particles (over 25 mm in diameter) impose significant uncertainties for the paste filling pipe flow detection. The efficiency of paste filling depends on the flow rate of the paste in the filling pipe; but up to now, it has been difficult to measure this rate with sufficient accuracy. The inaccuracy in the flow rate measurement has resulted in a great waste of filling material and excessive consumption of electricity and human resources, causing deleterious consequences for environmental issues and safety production.

At present, the sensors used for fluid flow measurement include differential pressure flowmeter, capacitive flowmeter, electromagnetic flowmeter, and ultrasonic flowmeter, and all of those are not suitable for measure multiphase fluid flow

precisely [2]. Differential pressure flowmeter needs installation of an orifice plate or a shrink diameter pipe. The large diameter material has a serious side effect of aggregating damage on the orifice plate, which is likely to cause congestion accidents [3]. Capacitance flowmeter fails to capture measurement of fluid flow because the dielectric value of the paste is usually reflected by the dynamic changes of the concentration of the paste [2]. Electromagnetic flowmeter can be easily blocked, because the large diameter material accounted for about 50% of the filling material, resulting in distortion of the measurement results of the sensor [2, 3]. Ultrasonic flowmeter sensor is unable to accurately detect flow information because only weak signals are received due to the high mass concentration of the filling paste and the serious viscous viscosity and scattering attenuation [4]. Because of these limitations in paste flow measurement, all the above flow sensors cannot be effectively used in detection for paste-filling flow.

A resistance-type differential pressure flow (RDPF) sensor has been developed to achieve precise measurements. Noncontact and real-time flow measurement in the paste-

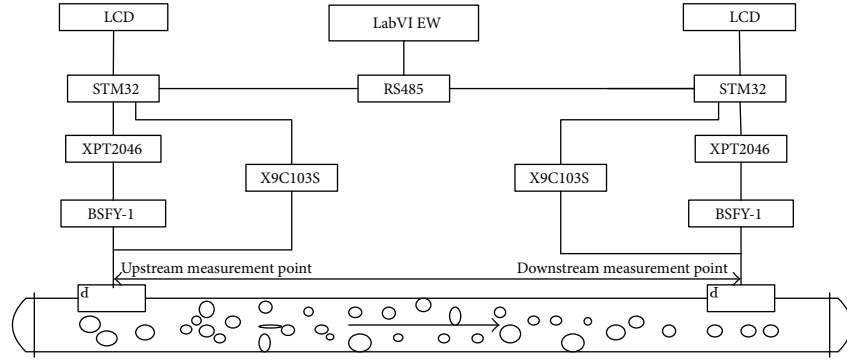


FIGURE 1: Schematic diagram of the RDPF sensor.

filling pipe is realized by the sensor. However, there is much space for improvement in the measurement error of the RDPF sensor. Thereby, error compensation model is built to compensate error. In recent years, both neural network theory and fuzzy theory have been applied to error modeling, but these two approaches are appropriate only for offline modeling and are not applicable to online error compensation [5–7]. Common methods that are suitable for online modeling include autoregressive modeling, minimum support vector machine modeling, and Bayesian dynamic model theory [8–13]. The paste flow in the pipeline changes periodically, which must be taken into account when building error compensation models to achieve sufficient accuracy [14–16]. Because the above models are not ideal for error compensation of RDPF sensor, a new compensation error method is proposed [17–19].

## 2. RDPF Sensor and Analysis of Its Measurement Error Characteristics

**2.1. RDPF Sensor.** Based on pressure difference detection principle, an indirect pipe flow measurement method is proposed by measuring the deformation of filling pipe. According to the pressure difference test theory of resistance strain gauge, the RDPF sensor is designed. The sensor includes a bridge measuring circuit, an amplifying circuit, an electric bridge automatic zeroing circuit, an analog/digital (A/D) conversion circuit, and a sample hold circuit. The analog signals from the strain gauge are converted into digital signals, and then the digital signals are uploaded through a communication module to a host computer which displays and stores the fill-pipe flow value with the software of LabVIEW. The principle of the RDPF sensor is shown in Figure 1.

**2.2. Measurement Error Analysis for the RDPF Sensor.** Mined-area filling capacity is regarded as the exact value of the paste flow, and it is compared with flow value measured by the RDPF sensor without the use of any error compensation. The result shows that the accuracy of the sensor is low, with a relative error of about 5% compared to the value of mined-area filling capacity.

The flow rate in the paste-filling pipe following pipe pressure undergoes periodic changes, which is shown in Figure 2. The errors in the sensor can be divided into three

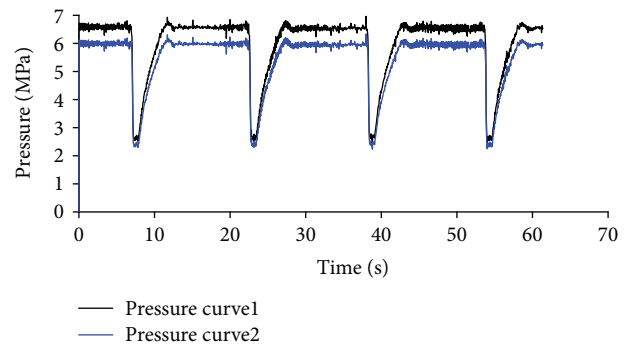


FIGURE 2: Measured value of pressure of paste-filling pipeline. Pressure curve1: pressure curve at upstream measuring point. Pressure curve2: pressure curve at downstream measurement point.

components: systematic error, random error, and gross error [20]. The gross error is mainly caused by accidental factors in the measurement process, such as strong interference, vibration, and human factors. The gross error can be eliminated by previous experience before building the compensation error model. The systematic error mainly consists of three components: pipe flow modeling error, strain gauge error due to the effects of the paste, and measurement error caused by pipe wear [21].

- (1) The systematic error is produced because the rising stage of each cycle is approximated as a linear process for the pipe flow model.
- (2) The systematic error is also caused by the difference of strain gauge-pasted angle and adhesive coating thickness of RDPF.
- (3) When the paste velocity is low, there is serious pipe wear in straight sections of the pipe, and then the system error is also caused by the abrasion of the filling pipeline.

The flow sensor is installed on a straight pipe section with high paste-filling pressure. The installation position of the sensor is close to the paste-filling station. The random error is caused by the environmental noise and electromagnetic interference in this region.

### 3. Error Modeling

By comparison of the paste-filling capacity measured by the flow sensor with the paste-filling capacity of the mined area, the measurement error of the sensor  $\Delta\delta(t)$  is obtained. According to the real-time flow curve in Figure 2, the filling flow changed in a periodic fashion follows the filling stroke of the filling pump. The measurement error can then be expressed as

$$\Delta\delta(t) = \Delta\delta_u(t) + \Delta\delta_e(t), \quad (1)$$

where  $t$  is the measurement time,  $\Delta\delta_u(t)$  is the periodic error component, and  $\Delta\delta_e(t)$  is the aperiodic error component.

**3.1. Periodic Error Compensation Model.** Through mathematical analysis of the systematic error, it is known that the periodic error in the flow sensor satisfies a Dirichlet condition (DC) in the period  $[0, T]$ , and therefore the periodic error in the dynamic measurements can be decomposed into an infinite series of linear combinations of trigonometric functions:

$$\begin{aligned} \Delta\delta_u(t) &= a_0 + a_1 \cos \omega_0 t + b_1 \sin \omega_0 t + a_2 \cos \omega_0 t \\ &+ b_2 \sin \omega_0 t + \dots = a_0 + \sum_{h=1}^{\infty} (a_h \cos \omega_0 t + b_h \sin \omega_0 t), \end{aligned} \quad (2)$$

where  $\omega_0$  is fundamental wave angle frequency, and  $a_0, a_1, a_2, \dots, a_n, b_1, b_2, \dots, b_n$  are Fourier coefficients of signals.

Using trigonometric identities, formula (2) can be rewritten as follows:

$$\Delta\delta_u(t) = A_0 + \sum_{h=1}^{\infty} A_h \cos(h\omega_0 t - \phi_h), \quad (3)$$

where  $A_0$  is the amplitude of the DC component,  $A_h = \sqrt{a_h^2 + b_h^2}$  are the amplitudes of the frequency components, and  $\phi_h = \arctan(a_h/b_h)$  are the phase angles of the frequency components. Therefore, the dynamic model of measurement error for the sensor is built after the amplitude and phase angle for each frequency are determined.

In the dynamic measurement of the paste flow,  $k+1$  data points are measured in each period. The measurement period is discretized according to the equidistant measurement method to obtain  $\Delta\delta_u(t)$ , and the time value of the measurement point can be expressed as  $t_i = it/(k+1), i=0, 1, 2, \dots, k$ .

Formula (3) can be expressed in matrix form as follows:

TABLE 1: Amplitude and phase angle of each harmonic.

Number of harmonics $n$	Harmonic amplitude $A_n$	Harmonic angle $\varphi_n$
0	-181.442	
1	5.767899	6.362538
2	215.75	1.458583017
3	-495.472	2.039259482
4	325.7386	1.367623042
5	155.6761	3.624029617

$$\begin{aligned} \Delta\delta_u(t) &= \begin{bmatrix} \Delta\delta_u(t_0) \\ \Delta\delta_u(t_1) \\ \Delta\delta_u(t_2) \\ \vdots \\ \Delta\delta_u(t_k) \end{bmatrix}, \\ \mathbf{L} &= \begin{bmatrix} A_0 \\ A_1 \\ A_2 \\ \vdots \\ A_k \end{bmatrix}, \\ \mathbf{A} &= \begin{bmatrix} 1 & \cos(\omega_0 t_1 - \phi_1) & \cos(2\omega_0 t_1 - \phi_2) & \dots & \cos(h\omega_0 t_1 - \phi_h) \\ 1 & \cos(\omega_0 t_2 - \phi_1) & \cos(2\omega_0 t_2 - \phi_2) & \dots & \cos(h\omega_0 t_2 - \phi_h) \\ 1 & \cos(\omega_0 t_3 - \phi_1) & \cos(2\omega_0 t_3 - \phi_2) & \dots & \cos(h\omega_0 t_3 - \phi_h) \\ \vdots & \vdots & \vdots & \dots & \vdots \\ 1 & \cos(\omega_0 t_k - \phi_1) & \cos(2\omega_0 t_k - \phi_2) & \dots & \cos(h\omega_0 t_k - \phi_h) \end{bmatrix}, \\ \Delta\delta(t) &= \mathbf{A} \times \mathbf{L} + \Delta\delta_e(t). \end{aligned} \quad (4)$$

Theoretically, in the formula (2), an infinite number of frequency components are superimposed, but when the relative error between the values measured by the flow sensor and mined-area filling capacity is less than 1%, the measurement accuracy is completely satisfactory, and the summation over frequency components can be truncated.

**3.2. Aperiodic Error Dynamic Compensation Model.** Based on the dynamic data exchange (DDE) technique and the least squares support vector machine (LS-SVM) method, a dynamic compensation model of aperiodic error is established [22]. The LS-SVM method employs a support vector machine to convert inequality constraints into equality constraints. A nonlinear mapping between the filling time and the aperiodic error in the filling flow is established by the method, and nonlinear laws hidden in the sample data is revealed. For nonlinear sample data  $(x_1, y_1), (x_2, y_2), \dots, (x_l, y_l)$ , using LS-SVM regression, the regression problem for the aperiodic error can be described as follows:

TABLE 2: Sensor measured values.

Time/h	Mined-area filling capacity/m <sup>3</sup>	Sensor measured value (uncompensated)/m <sup>3</sup>	Sensor measurement (compensated for aperiodic error)/m <sup>3</sup>	Sensor measurement (compensated for periodic and nonperiodic errors)/m <sup>3</sup>
0.5	0.625	0.655	0.6298	0.6251
1	1.24	1.3	1.2475	1.2402
1.5	1.845	1.935	1.8545	1.8452
2	2.46	2.57	2.461	2.46
2.5	3.06	3.195	3.0568	3.0599
3	3.66	3.84	3.6721	3.6603
3.5	4.26	4.465	4.2668	4.2602
4	4.87	5.105	4.8677	4.8699
4.5	5.485	5.745	5.4845	5.485
5	6.09	6.375	6.0825	6.0898
5.5	6.69	7	6.675	6.6897
6	7.3	7.645	7.2869	7.2997

$$\begin{aligned} \min \quad & J(\omega, \xi) = \frac{1}{2} \omega^T \omega + \gamma \frac{1}{2} \sum_{i=1}^l \xi_i^2, \\ \text{s.t.} \quad & y_i = \omega^T \varphi(x_i) + b + \xi_i, \\ & i = 1, \dots, l, \end{aligned} \quad (5)$$

where  $x_1, x_2, \dots, x_l$  are the input variables,  $y_1, y_2, \dots, y_l$  are the output expected values,  $\xi_1, \xi_2, \dots, \xi_l \in R$  are the error variables,  $\varphi(x): R^n \rightarrow R^{nh}$  is the kernel space mapping function,  $\omega \in R^{nh}$  is a right vector,  $\gamma$  is an adjustable parameter, and  $b$  is the amount of deviation. Then, the Lagrangian function is introduced.

$$L = \frac{1}{2} \omega^T \omega + \gamma \frac{1}{2} \sum_{i=1}^l \xi_i^2 - \sum_{i=1}^l a_i [\omega^T \varphi(x_i) + b + \xi_i - y_i], \quad (6)$$

where  $a_i (i = 1, 2, \dots, l)$  is Lagrange multiplies. According to the necessary conditions for the existence of extreme values,  $\partial L / \partial \omega = 0$ ,  $\partial L / \partial b = 0$ ,  $\partial L / \partial \xi_i = 0$ , and  $\partial L / \partial a_i = 0$ , the following formula is gotten:

$$\begin{aligned} \omega &= \sum_{i=1}^l a_i \varphi(x_i), \\ \sum_{i=1}^l a_i &= 0, \\ a_i &= \gamma \xi_i, \\ y_i &= \omega^T \varphi(x_i) + b + \xi_i, \\ & i = 1, 2, \dots, l. \end{aligned} \quad (7)$$

The following formula is obtained by eliminating  $\omega$  and  $\xi$  of formula (7),

$$\beta_l A_l = Y_l, \quad (8)$$

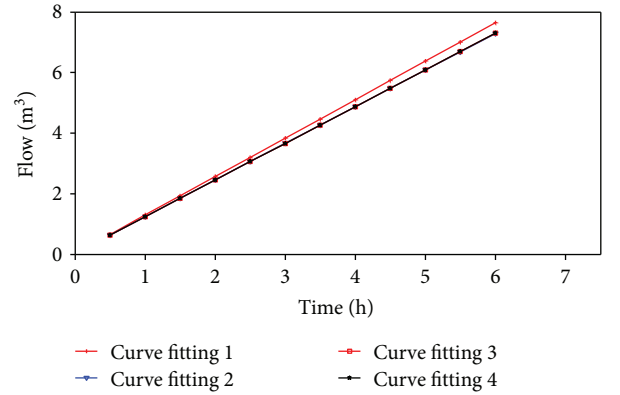


FIGURE 3: Flow values before and after error compensation. Curve fitting 1: sensor measured value (uncompensated). Curve fitting 2: sensor measurement (compensated for aperiodic error). Curve fitting 3: sensor measurement (compensated for periodic and nonperiodic errors). Curve fitting 4: mined-area filling capacity.

$$\begin{aligned} \beta_l &= \begin{bmatrix} 0 & 1 & \dots & 1 \\ 1 & K(x_1, x_1) + \frac{1}{\gamma} & \dots & K(x_1, x_l) \\ \vdots & \vdots & \ddots & \vdots \\ 1 & K(x_l, x_1) & \dots & K(x_l, x_l) + \frac{1}{\gamma} \end{bmatrix}, \\ A_l &= \begin{bmatrix} b \\ a_1 \\ \vdots \\ a_l \end{bmatrix}, \\ Y_l &= \begin{bmatrix} 0 \\ y_1 \\ \vdots \\ y_l \end{bmatrix}, \end{aligned} \quad (9)$$

where  $K(x, x_i)$  is kernel function.

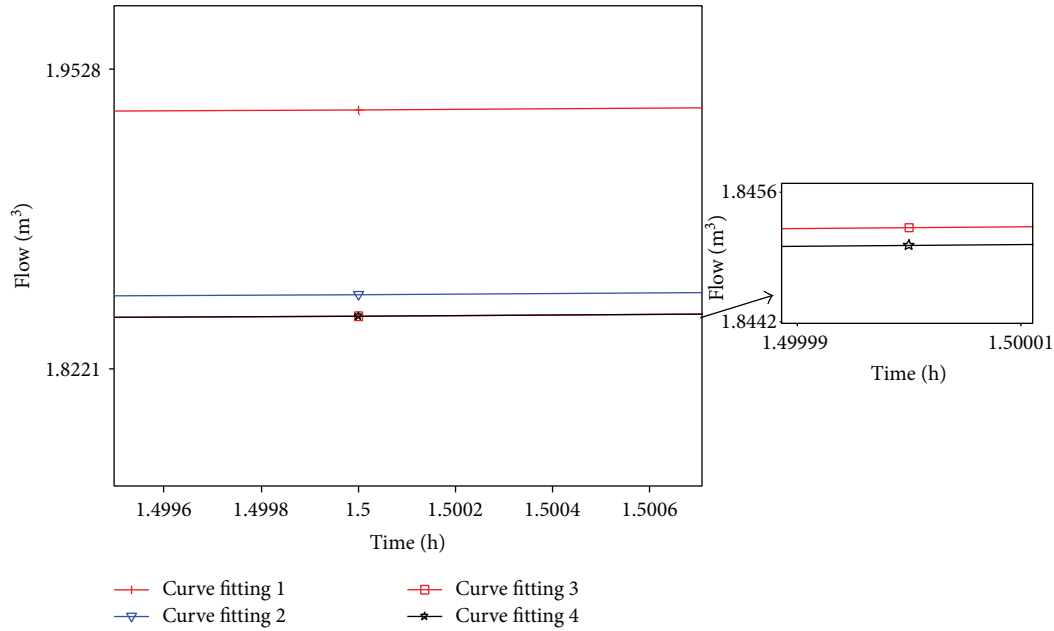


FIGURE 4: Local enlargement of Figure 3.

Linear kernel functions, polynomial kernel functions, and the radial basis function (RBF) kernel functions are commonly used kernel functions. The kernel function must satisfy Mercer's condition. Then, LS-SVM regression estimate using kernel function  $K(x, x_i)$  can be expressed by formula (10). The values of  $a_i$ - and  $b$  are obtained by the least square method [23–25].

$$f(x) = \sum_{i=1}^l a_i K(x, x_i) + b. \quad (10)$$

## 4. Results

**4.1. Determination of Model Parameters.** The error of the Fourier series approximation model satisfies the filling requirement when it is less than 1%. The error in the Fourier series approximation model meets the sensor measurement requirements when the fifth harmonic overlay is fitted by MATLAB. Using formula (7), the least squares principle is applied to solve for the amplitude and phase angle of each harmonic. The results are shown in Table 1.

The radial basis function (RBF)  $K(x_i, x_j) = \exp[-(x_i - x_j)^2 / (2\sigma^2)]$  is selected as the kernel function. The cross-validation method is chosen for determining the parameter  $\sigma$  in the RBF and the parameter  $\gamma$  in the LS-SVM model. To decrease the search time of the two parameters, the kernel function  $\sigma = \{20, 10, 5, 2, 1, 0.1, 0.01\}$  and the punishment constant  $\gamma = \{200, 100, 50, 20, 10, 5, 2, 1\}$  are chosen, thereby, the optimal parameter pairs ( $\gamma = 200, \sigma = 0.1$ ) are obtained by cross-validation. Then, acquisition time as the input, and the flow value measured by the sensor as the output, an aperiodic error compensation model is established. The square sum of the relative error is obtained, which is 0.0262.

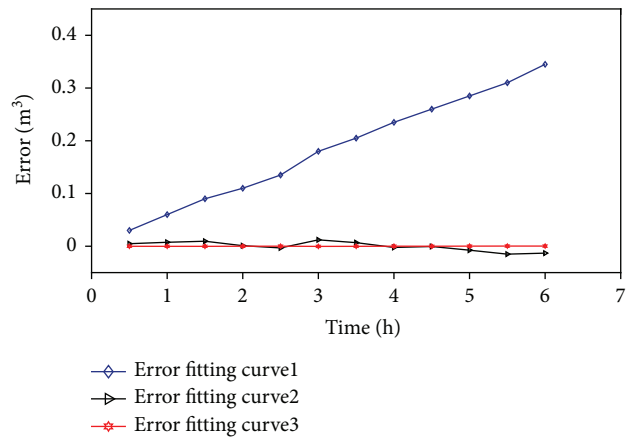


FIGURE 5: Error before and after error compensation. Error fitting curve1: measured error of sensor without compensated. Error fitting curve2: measured error of sensor with compensated for aperiodic. Error fitting curve3: measured error with compensated for periodic and nonperiodic errors.

**4.2. Experimental Analysis.** In coal gangue paste-filling process, the experimental platform of the sensor measurement accuracy is built. The sensor without compensation, the sensor of compensation for periodic error, and the sensor of compensation periodic error and aperiodic error are installed in the experimental pipeline. The measured flow values of three sensors are listed in Table 2.

The curve of flow values before and after error compensation is shown in Figure 3 after following the measured data in Table 2. Local enlargement of Figure 3 is shown in Figure 4. Measurement values with different compensation module are compared with mined-area filling capacity value (Figure 5). Seen from Figure 5, the measurement error increases with time without error compensation. When the Fourier series approximation method is used to compensate

for the periodic error, the measurement error of the sensor is obviously reduced. When the LS-SVM method is used to compensate periodic error, the measurement error of the sensor is reduced greatly, which is changed little with time.

## 5. Discussion

Under different conditions, the measured curves and error curves of the sensor are shown in Figures 3–5. Seen from Figures 3 to 5, the sensor has a large measurement error in the absence of compensation, but, when using the Fourier series approximation model to compensate for the periodic error, the error is greatly reduced, which shows that periodic error is the main component of the sensor measurement error. After compensation for both periodic and aperiodic error, the measurement error of the sensor fluctuates around zero, which indicates that the dynamic measurement accuracy of the sensor is greatly improved.

To guarantee dynamic compensation of aperiodic error, dynamic data exchange (DDE) can be used to realize real-time data exchange between MATLAB and the host computer. The flow value measured by the sensor and the mined-area filling capacity obtained through a data acquisition card are uploaded to the host computer. Models of the periodic and aperiodic errors are established in MATLAB using the above values, and the model parameters are calculated and then sent to the error compensation model to achieve dynamic compensation of measurement errors.

The value of RDPF sensor is related to the filling pipe pressure and the length and cross-sectional area of the filling pipe. When the discontent tube filling fault occurs, the cross-sectional area of the filling paste in the tube is smaller than the pipe cross-sectional area, making the measured result deviating from the actual filling flow. Therefore, the filling failure of the discontent tube should be avoided to improve the measurement accuracy of the RDPF sensor.

## 6. Conclusions

The measurement errors of the RDPF sensor have been analyzed. The periodic error model is established by a Fourier series approximation method. The parameters of the periodic error model are obtained by solving an overdetermined matrix by the least squares method. The aperiodic error model is constructed using an online LS-SVM method, and the model parameters are solved by cross-validation. Experiments show that the method proposed in the paper can greatly reduce the measurement error of the sensor and improve its dynamic measurement accuracy.

## Conflicts of Interest

The authors declare no conflict of interest.

## Authors' Contributions

Lijie Yang and Guimei Wang conceived and designed the experiments. Tao Chu performed the experiments. Lijie Yang

analyzed the data. Fang Sun contributed analysis tools. Tao Chu and Lijie Yang wrote and revised the paper.

## Acknowledgments

This project was supported by the Hebei Province Science and Technology Support Program (16394102D) and the science and technology research project of Hebei Higher Education Institutions (QN2014171).

## References

- [1] J. G. Liu, "Study and practice of low-carbon ecological mining," *Journal of China Coal Society*, vol. 36, no. 2, pp. 317–321, 2011.
- [2] G. M. Wang and S. Zhang, "Paste filling pipe on-line detection system," *Machine Tool & Hydraulics*, vol. 43, no. 8, pp. 161–163, 2015.
- [3] Y. J. Chen and B. W. Zhao, *Integrated Mechanized Paste Filling Coal Mining Technology*, Coal Industry Press, Beijing, China, 2012.
- [4] D. Y. Wang, *Analysis of Attenuation Characteristics of Ultrasonic Propagation in Mud*, Shenyang University of Technology, 2014.
- [5] S. Z. Sun and D. L. Peng, "Research on modeling and compensation technology for time-grating sensor's dynamic measurement errors," *Journal of Mechanical Engineering*, vol. 50, no. 22, pp. 10–15, 2014.
- [6] S. Z. Sun and D. L. Peng, "Compensation for dynamic measurement errors of time grating sensor," *Optics and Precision Engineering*, vol. 23, no. 4, pp. 1114–1121, 2015.
- [7] S. G. Gumarov and O. N. Korsun, "A method of determining the dynamic error of optical trajectory measurement stations," *Measurement Techniques*, vol. 54, no. 3, pp. 281–286, 2011.
- [8] J. Guajardo, R. Weber, and S. F. Crone, "A study on the ability of support vector regression and neural networks to forecast basic time series patterns," *International Federation for Information Processing Digital Library*, vol. 217, no. 1, pp. 149–157, 2010.
- [9] T. Zhang and W. H. Ye, "Temperature variable optimization for precision machine tool thermal error compensation on optimal threshold," *Chinese Journal of Mechanical Engineering*, vol. 26, no. 1, pp. 158–165, 2013.
- [10] S. Q. Liu and R. Zhu, "System error compensation methodology based on a neural network for a micromachined inertial measurement unit," *Sensors*, vol. 16, no. 2, p. 175, 2016.
- [11] F. J. Wang and Z. Y. Jia, "Time-varying position error compensation of machine tools based on dynamic fuzzy neural networks," *Journal of Mechanical Engineering*, vol. 47, no. 13, pp. 175–179, 2011.
- [12] Y. Zhang and J. G. Yang, "Modeling for machine tool thermal error based on grey model preprocessing neural network," *Journal of Mechanical Engineering*, vol. 47, no. 7, pp. 134–138, 2011.
- [13] D. H. Wu, "Compensation for nonlinear dynamic system of transducer based on least squares support vector machine," *Chinese Journal of Scientific Instrument*, vol. 28, no. 6, pp. 1018–1023, 2007.
- [14] H. Yang, K. Huang, I. King, and M. R. Lyu, "Localized support vector regression for time series prediction," *Neurocomputing*, vol. 72, no. 10–12, pp. 2659–2669, 2009.

- [15] Z. Jia, "Characteristics prediction method of electro-hydraulic servo valve based on rough set and adaptive neuro-fuzzy inference system," *Chinese Journal of Mechanical Engineering*, vol. 23, no. 2, p. 200, 2010.
- [16] H. Yang, L. Zhang, J. Zhou, Y. Fei, and D. Peng, "Modelling of dynamic measurement error for parasitic time grating sensor based on Bayesian principle," *Optics and Precision Engineering*, vol. 24, no. 10, pp. 2523–2531, 2016.
- [17] W. Lin, J. Z. Fu, Z. C. Chen, and Y. Z. Xu, "Modeling of NC machine tool thermal error based on adaptive best-fitting WLS-SVM," *Journal of Mechanical Engineering*, vol. 45, no. 3, pp. 178–182, 2009.
- [18] J. Li, G. Hu, Y. Zhou, and J. A. SM, "A temperature compensation method for piezo-resistive pressure sensor utilizing chaotic ions motion algorithm optimized hybrid kernel LSSVM," *Sensors*, vol. 16, no. 10, p. 1707, 2016.
- [19] J. Li, G. Hu, Y. Zhou, C. Zou, W. Peng, and J. A. Sm, "Study on temperature and synthetic compensation of piezo-resistive differential pressure sensors by coupled simulated annealing and simplex optimized kernel extreme learning machine," *Sensors*, vol. 17, no. 4, p. 894, 2017.
- [20] Y. T. Fei, *Error Theory and Data Processing*, China Machine Press, Beijing, China, 1987.
- [21] J. Guo and B. X. Zhang, "Numerical investigation of impact erosion in liquid-solid two-phase flow of backfilling pipe," *Science & Technology Review*, vol. 33, no. 11, pp. 49–53, 2015.
- [22] Z. J. Tang and F. Ren, "Chaotic time series least squares support vector machine prediction algorithm based on iterative error compensation," *Acta Physica Sinica*, vol. 63, no. 5, pp. 78–87, 2014.
- [23] W. Y. Lin and J. Z. Fu, "Thermal error modeling & compensation of numerical control machine tools based on on-line least squares support vector machine," *Computer Integrated Manufacturing Systems*, vol. 2, no. 2, pp. 295–299, 2008.
- [24] M. M. Adankon and M. Cheriet, "Model selection for the LS-SVM. Application to handwriting recognition," *Pattern Recognition*, vol. 42, no. 12, pp. 3264–3270, 2009.
- [25] H. S. Tang, S. T. Xue, R. Chen, and T. Sato, "Online weighted LS-SVM for hysteretic structural system identification," *Engineering Structures*, vol. 28, no. 12, pp. 1728–1735, 2006.